THREE-DIMENSIONAL RECONSTRUCTION OF TURBULENT GASES USING STEREO SCHLIEREN AND SHADOWGRAPH TECHNIQUES

by

Kyle Jeffrey Benalil

Submitted in Partial Fulfillment
of the Requirements for the Degree of
Master of Science in Mechanical Engineering
with Specialization in Fluid and Thermal Sciences

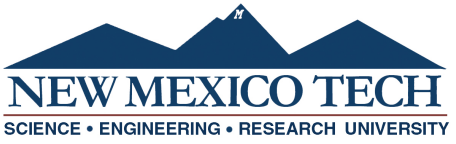

New Mexico Institute of Mining and Technology
Socorro, New Mexico
September, 2018

ABSTRACT

Quantifying turbulent mixing in a post-detonation environment has remained a challenge for modern fluid tracking techniques. In recent years, schlieren and shadowgraph imaging have been used to quantify velocity field characteristics of a detonation in two dimensions, but no thorough study of the turbulence or three-dimensional motion has been completed. The present work explores the capabilities of tracking turbulent flow in three dimensions by combining the information from schlieren and shadowgraph imaging with multi-camera systems. Schlieren and projective shadowgraph setups were used with two high-speed cameras at small stereo angles to develop three-dimensional reconstructions of refractive index fields. The cameras were calibrated using a target checkerboard with known dimensions and the MATLAB Stereo Camera Calibrator App, plus additional MATLAB functions to ultimately build three-dimensional reconstructions of the flow. A two-dimensional helium jet study using particle image velocimetry and schlieren image velocimetry was performed to validate the three-dimensional reconsturcted velocities. The three-dimensional study showed that stereo schlieren imaging with parallel-light lens systems did not yield a depth effect. However, the projective shadowgraphy experiment was able to reconstruct the helium jet into three-dimensional space because of the inherent diverging light rays. Following the validation experiments, a series of explosive tests were conducted with each system. The stereo schlieren test identified even with small camera angles, the parallel light in each schlieren system may not refract the same due to local changes in temperature and density along the two different optical paths. The projective shadowgraph explosively-driven field-scale test successfully reprojected the shock wave, fireball and gas cloud expansion into three-dimensional space. Velocity measurements were taken by manually identifying locations that could be matched over a series of frames. The work here shows promise for this technique to be used for tracking the shock, fireball and gas cloud propagation, but additional development of image processing routines must be made to allow automation of the process.

Keywords: Stereo imaging; schlieren; shadowgraph; turbulence; tracking; three-dimensional reconstruction; schlieren image velocimetry

ACKNOWLEDGMENTS

I would like to thank Dr. Michael J. Hargather for his continued insight, guidance and enthusiasm. While working for Dr. Hargather, I developed a passion for thinking outside the box and creating unique solutions to solve problems. This led me to conducting a variety of experiments in fluids and explosives that I didn't know were possible. He has been an inspiration and instilled vital skills necessary for me as a researcher and experimentalist. This work would not have been possible without him, thank you.

The New Mexico Tech faculty and staff, as well as the employees of the Energetic Material Research Testing Center were extremely accommodating during this research. Everyone was easy to work with and quick to assist me, whether it was ordering new parts, borrowing equipment, using facilities, developing test plans or providing guidance on how to best setup for an experiment. They have made this work possible thanks to their drive for success and encouragement for continued learning.

Members of the Shock and Gas Dynamic Laboratory have been an incredible help throughout this work. Thank you for teaching me the fundamentals of schlieren and shadowgraph imaging and providing insightful suggestions along the way. Thank you for making this research enjoyable even on the dullest of days. Your work ethic, positive attitude and intellectual wisdom has been very influential, thank you.

My family has provided endless support for me during my undergraduate and graduate education. Not only did they give me direction and encouragement in my education, but also in my work, hobbies and all other activities. Thank you for always pushing me to be better and for your continuous love and support in all my endeavors. I could not have done it without you!

My friends have always been around to support me, and I can't thank you all enough. You've all been an inspiration and had an incredible impact on my life. Thank you for being a part of my life and helping shape the way I am today.

Portions of this research were funded through Air Force STTR Phase I contract FA8651-17-P-0126 with Protection Engineering Consultants as the prime contractor with New Mexico Tech as a subcontractor.

CONTENTS

LIST OF TABLES

LIST OF FIGURES

Figure **Page**

This thesis is accepted on behalf of the faculty of the Institute by the following committee:

Michael J. Hargather

Academic and Research Advisor

Seokbin Lim

William Stone

I release this document to the New Mexico Institute of Mining and Technology.

Kyle Jeffrey Benalil July, 2018

CHAPTER 1

INTRODUCTION

1.1 Research motivation

Turbulent mixing in a post-detonation environment has not been well characterized because it is difficult to implement fluid tracking techniques in experiments. Schlieren imaging and shadowgraphy are visualization techniques that have been used to quantify certain characteristics of an explosion, including tracking; however, limited work has been done to expand these two-dimensional visualization techniques into three dimensions. This work will focus on validating stereoscopic schlieren and shadowgraph imaging as techniques for tracking turbulent gases in an explosive environment in three dimensions. The success of this technique would allow physical data to be integrated with current numerical simulations to improve the results in a variety of applications.

1.2 Literature review

Fluid flow field measurement approaches can be classified as either intrusive or non-intrusive. Intrusive techniques encompass methods that insert a measuring instrument into the flow, such as a pitot-pressure or hot-wire probe. Because the instrument is put directly in the flow field, it causes disturbances within the flow, which can be problematic for obtaining information within the entire flow field. Non-intrusive techniques perform measurements without directly inserting the measurement device into the flow, thus are generally considered to not disturrb the natural flow fields. A range of non-intrusive techniques have been used to quantify turbulent motion in fluid-dynamic experiments, including laser Doppler velocimetry, particle image velocimetry, schlieren and shadowgraphy. An extensive list of other techniques can be found in [36]. Intrusive and non-intrusive measurements each have their own advantages and drawbacks, the work performed here focuses on non-intrusive measurements.

1.2.1 Laser-Doppler velocimetry

Laser Doppler velocimetry (LDV), or laser Doppler anemometry (LDA), is one of the first non-intrusive methods developed to obtain velocity information

in a fluid flow [60]. Figure 1.1 shows a simple schematic of an LDV system. Two laser beams of collimated, monochromatic, and coherent light are crossed in the test section. The crossing of the coherent lasers creates a set of straight fringes shown in the zoomed in region of Figure 1.1. As particles that have been introduced into the flow pass through the fringes, they reflect light, which is captured by a photodetector. The reflected light from the particle fluctuates in intensity, which is related to the Doppler shift between the incident and scattered light. The velocity of the particle is calculated by multiplying the frequency of intensity fluctuations by the distance between the fringes.

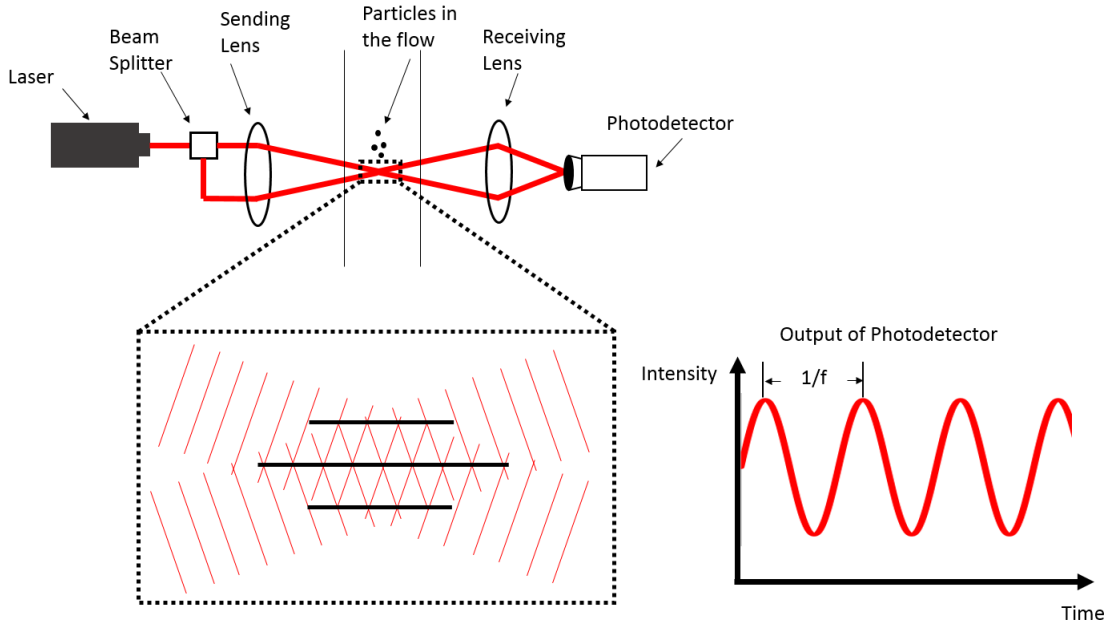

Figure 1.1: A schematic of LDV showing fluctuation intensities observed by the photodetector as particles pass through the fringes of the coherent light beams.

LDV offers several advantages over intrusive techniques: It allows local velocity information to be gathered from the flow field with high spatial and temporal resolution, it can be used in environments not suitable for classical measurements and additional modifications can be made to the setup to simultaneously determine multiple velocity components [5]. LDV is a well established technique that has been used to conduct studies in subsonic and supersonic flows [2, 4, 16, 27, 31]. A similar technique has been used to conduct explosive tests called photonic Doppler velocimetry [12, 33, 37]. The disadvantage of LDV is that only a singular point in the flow field is measured. Other non-intrusive techniques such as particle image velocimetry, schlieren imaging and shadowgraphy offer the capability to study planar views of the flow field.

1.2.2 Particle image velocimetry

Particle image velocimetry (PIV) is a powerful flow visualization technique in which light scattering particles are injected into the fluid flow field, illuminated by a pulsing laser sheet and photographed with a synchronized camera. This produces a planar image in which the particles can be identified and tracked, which is ultimately used to obtain the flow field velocity. Figure 1.2 is a schematic of a typical PIV setup.

Although PIV is a simple concept, properly seeding the flow is very challenging. Particles must be introduced to the flow in such a way as not to disturb it. In gaseous flows, this is particularly difficult because the particle diameter must be very small in order to compensate for the large density difference between the particle and fluid; however, not so small that the light scattering properties of the particle are affected [43]. If too large of particles are injected into the flow, a velocity lag of the particles will be observed, and sudden changes in the flow, such as turbulent fluctuations, will not be captured [39, 43]. Additional information on how to properly setup PIV can be found in [43].

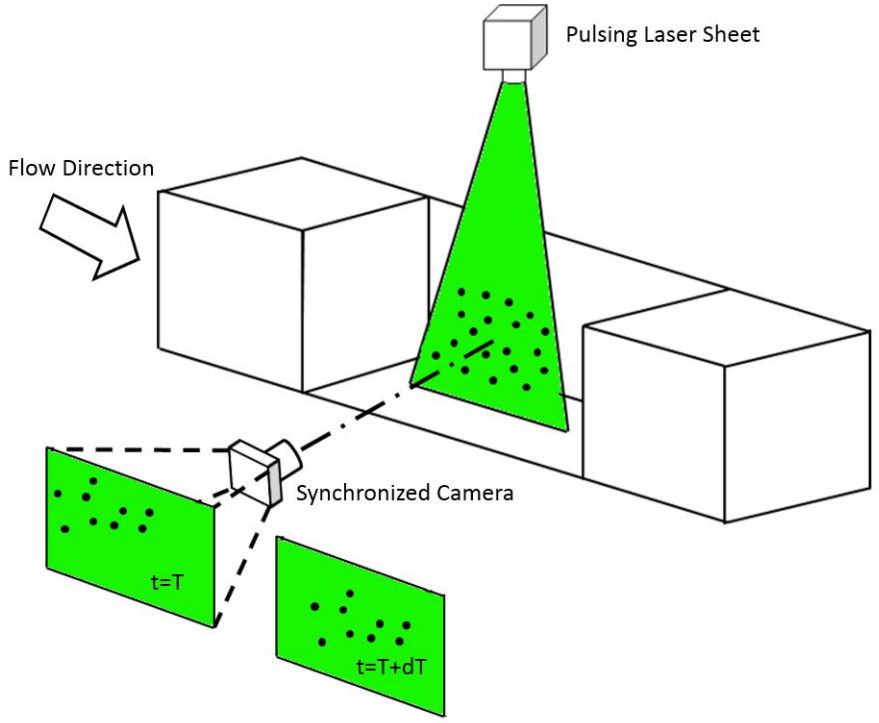

Figure 1.2: Typical PIV schematic illustrating particle movement after some dT.

Despite the challenges, significant advances have been made in high-speed PIV applications thanks to the development of high-speed cameras and more robust lasers. For example, PIV has been used to quantify flows in high-speed wind

tunnels. Scarano discusses the current capabilities and limitations of PIV in super and hypersonic flow [45]. Additionally, time-resolved PIV at Mach 0.8 was achieved by Beresh et al. in Sandia National Laboratories' Transonic Wind Tunnel [6]. Prior to Beresh et al.'s work, time-resolved PIV has not been achieved in a high-speed test facility.

Beyond steady flow conditions, PIV can also be used to study unsteady flow fields; however, few studies have been performed to understand explosive features. Murphy et al. [39] conducted two types of PIV tests on the blast from exploding bridge wires. First, a standard PIV analysis was implemented that seeded the flow with 1-2 micron diameter olive oil droplets. Second, they seeded a solid, polydimethylsiloxane (PDMS), with 4 micron diameter metallic-coated polystyrene. By knowing how PDMS responds to shock interactions, the observed disturbances in the solid can be related back to velocity. The velocities obtained were lower than expected for both methods; however, Murphy and Adrian revisited the seeded solid and were able to obtain results with much better accuracy [38, 41]. Jenkins et al. [28] performed testing with aluminum and tungsten particles surrounding an explosive charge in order to obtain velocities of the metallic particles driven by the detonation using high speed cameras and PIV software. Shock waves have also been analyzed using PIV in a shock tunnel by creating a curtain of particles for the shock to pass through [57]. Thus far, PIV has only been used to track ejected fragments and shock expansion in explosions, leaving the turbulent mixing region uncharacterized. This is because properly seeding an explosive environment to capture the turbulent regime is incredibly challenging.

1.2.3 Schlieren and shadowgraph imaging

Schlieren and shadowgraphy allow us to see transparent media, including turbulent gaseous flows, by creating color contrasts and amplitude changes through refractive index changes in the flow [47]. In a simple schlieren setup, like the one pictured in Figure 1.3, a convex lens, L1, is used to collimate the light of a point source, such as an LED. A second convex lens, L2, is used to bring that collimated light back to a point, which is focused on a cutoff tool, CT. A camera is positioned immediately behind the cutoff tool to capture the event. Refracted light from the schlieren object will cause light to either be directed into the cutoff tool, blocking the light, or past the cutoff tool, allowing the light into the camera lens as illustrated by the solid line and dashed line, respectively. These will create darker and lighter regions in the image. Frequently, a razor blade will be used as the cutoff tool creating gradients perpendicular to the orientation of the razor blade. For example, if the razor blade is positioned vertically, this will create horizontal gradients; however, if the schlieren object is only producing vertical gradients it will remain unseen [47].

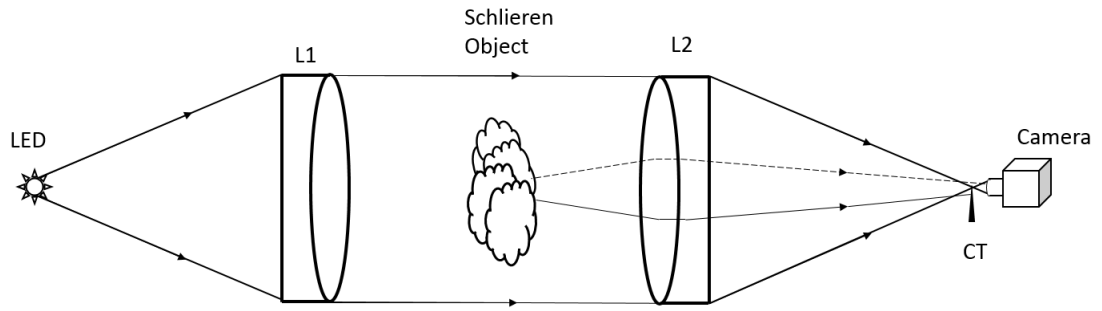

Figure 1.3: Schematic of a schlieren imaging setup with refracted light from the schlieren object.

When the cutoff tool is removed from the schlieren setup, it is called focused shadowgraphy. Additionally, the focus of the camera should no longer be on the schlieren object, but offset some distance, g, as seen in Figure 1.4. As g increases and the focus shifts closer to the camera, the sensitivity of the system is increased; consequently, the image becomes less focused. Figure 1.5 shows a series of helium jet shadowgrams while varying the camera's focus. In Figure 1.5a, the camera is focused direcly onto the helium jet's plane. While this focus provides very sharp turbulent structures, they are incredibly faint and near impossible to see even after the image has been processed. These turbulent structures become more apparent as the camera's focus is shifted away from the nozzle, but if the camera continues to defocus past 75 percent of the distance to the nozzle, the turbulence begins to blur and can no longer be used for quantitative analysis.

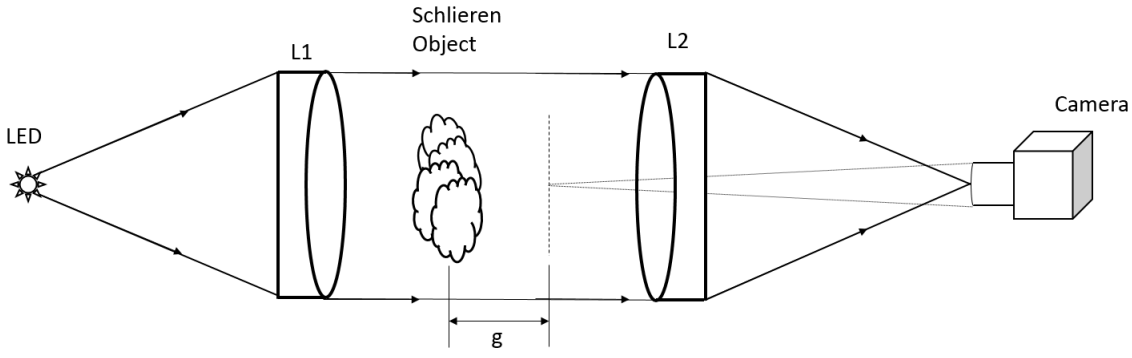

Figure 1.4: The camera's focus in a focused shadowgraph system should be shifted a distance g for proper imaging.

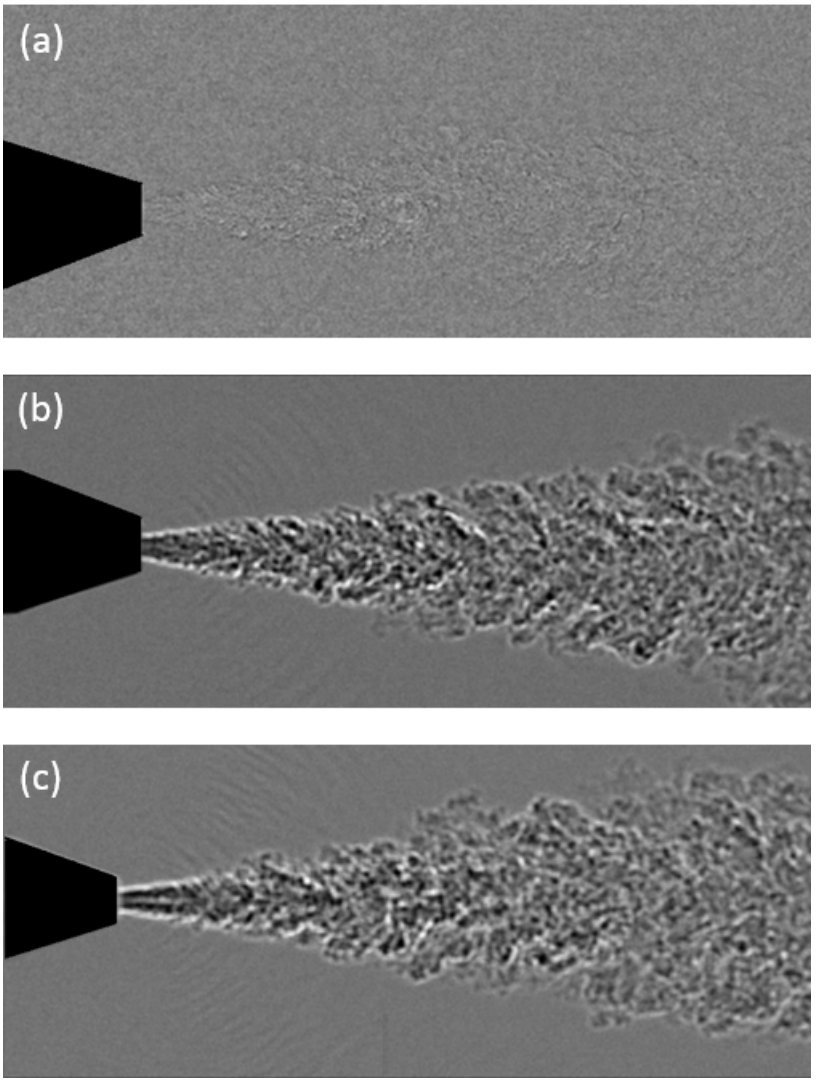

Figure 1.5: Shadowgram of a helium jet with (a) the camera's focus on the jet, (b) 85 percent of the distance to the jet and (c) 75 percent of the distance to the jet.

A side by side comparison of a schlieren and shadowgraph image can be seen in Figure 1.6. Because schlieren is the first spacial derivative of refractive index, and shadowgraphy is the second spacial derivative, the turbulent structures in Figure 1.6b have much sharper edges than the ones seen in Figures 1.6a. This allows shadowgraphy to capture sudden refractive index changes, such as turbulence and shock waves, better than schlieren; however it is unable to capture smooth features such as expansion waves [47].

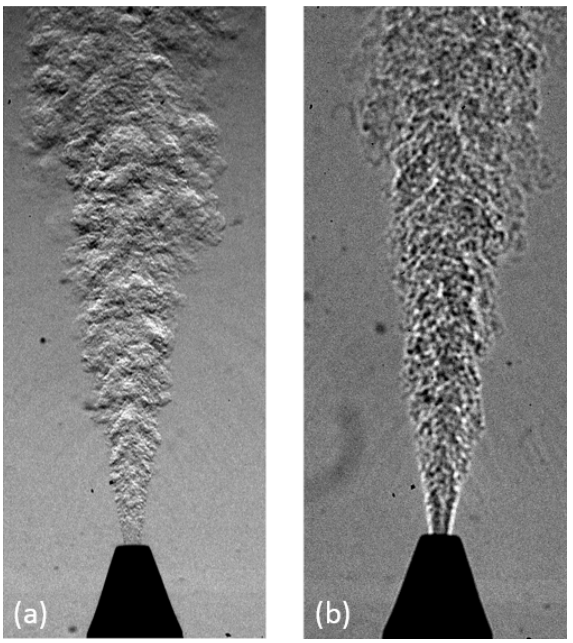

Figure 1.6: Comparison of (a) schlieren and (b) shadowgraph image of a helium jet.

Schlieren imaging has proven to be very successful in studying explosives [40, 49, 54], but its biggest drawback is its limited field of view because it can only be as large as the schlieren lenses. Projective shadowgraphy is a powerful alternative that can be used at much larger scales as shown in [9, 22, 48]. The basic schematic of a projective shadowgraph system can be seen in Figure 1.7. A bright light source is focused onto a rod mirror mounted on the camera lens. The rod mirror is a glass rod that has a 45 degree mirrored surface, allowing the illumination light to be made coaxial to the camera's imaging axis. The rod mirror casts the light over the schlieren object, creating a shadow on the retroreflective screen that is captured by the camera. The rod mirror is an essential part of the setup because it allows the camera to be coincident with the light. Prior to this configuration, the light source was offset from the camera, resulting in both the physical object and its shadow to appear in the image [22]. Like in focused shadowgraphy, the camera is focused past the object onto the retroreflective screen, which is a distance g away from the object.

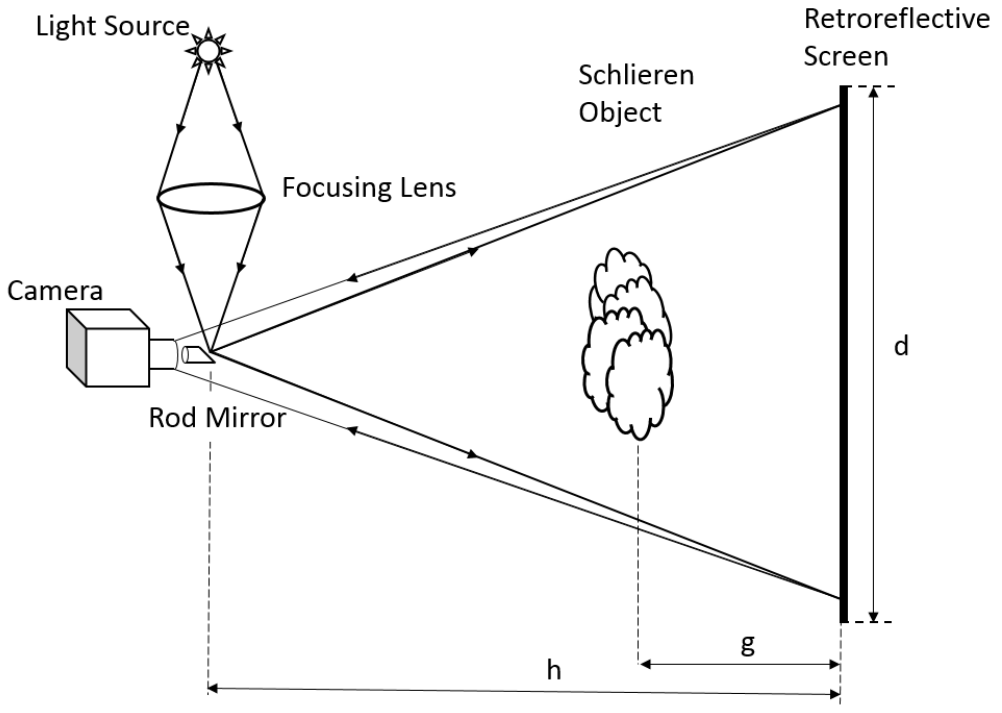

Figure 1.7: Schematic of projective shadowgraph system with the camera's focus onto the retroreflective screen.

1.2.4 Schlieren image velocimetry

Schlieren and shadowgraph imaging have been used to obtain quantitative data such as density, pressure and temperature measurements [23, 47, 54]. Velocity measurements have also been made using a technique called schlieren image velocimetry (SIV) [10, 21, 29]. The turbulent eddies in high speed flows naturally cause refractive index changes. The flow then becomes "seeded" with these turbulent eddies, which can be tracked using PIV software or image correlation techniques to obtain velocities. Because the challenge of properly seeding the flow is avoided, SIV has a significant advantage over PIV in certain applications. However, this technique is limited in that the flow must be turbulent.

Jonassen et al. [29], performed a sensitivity analysis on schlieren and shadowgraph setups in order to optimize the "particle" size for analysis in PIV software. The sensitivity of a schlieren system is proportional to the amount of light cutoff; as cutoff is increased, the schlieren system becomes more sensitive. Cutoff ranges between 30 and 60 percent were identified as ideal for PIV analysis. Cutoff percentage below this range do not provide sufficient information, and percentages greater than the ideal range have washed out regions that are not traceable in commercial PIV software [29].

Biwas and Qiao [10] performed work to validate SIV against PIV using a helium jet. Velocities of the helium jet using SIV were obtained using a vertical razor blade, horizontal razor blade and focused shadowgraphy (no cutoff tool). It was found that the cutoff perpendicular to the flow direction and focused shadowgraphy yielded the best results. However, there is another type of cutoff that was not studied by Biwas and Qiao, which is a circular cutoff tool. This allows light to be cutoff equally in all directions. A unidirectional cutoff is normally sufficient [47], but the circular cutoff will be explored in this study for completeness. Figure 1.8 shows how different cutoff tools affect the visualization of a helium jet.

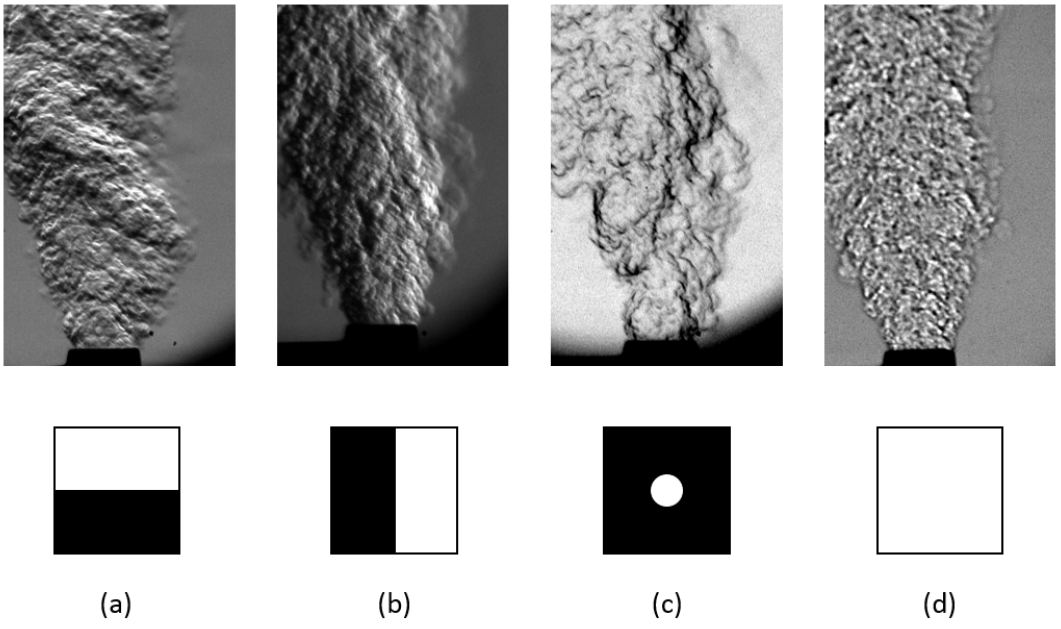

Figure 1.8: Images of a helium jet taken with different schlieren cutoff geometries: (a) horizontal knife edge, (b) vertical knife edge, (c) circular cutoff and (d) no cutoff or focused shadowgraphy.

1.2.5 Three-dimensional reconstruction

There are several methods available to create 3-D reconstructions of turbulent flows including stereoscopic imaging [59], tomography [1, 15, 19] and holography [15, 42]. The work in this study focuses on stereoscopic imaging. Stereo imaging is a well developed technique used in a variety of applications ranging from entertainment to robotics. Additionally, there are multiple and readily available software packages, including MATLAB and Open CV, that provide detailed documentation on how to create a 3-D image from a pair of stereo images.

Stereoscopic imaging uses two images of the same object at a slightly different angle in order to triangulate common points identified in the two views. Although work has been done to obtain 3-D information from a single camera [34, 44] these techniques sacrifice accuracy and frame rate, which is not ideal for this study. Thus a multi-camera system was the preferred method for calculating three-dimensional photometric data. Figure 1.9 illustrates how a multi-camera system can be used to triangulate points between the two images. Some of the challenges faced in a multi-camera system include synchronization and keeping similar parameters such as focus, zoom and exposure as these can affect the quality of reconstruction [34].

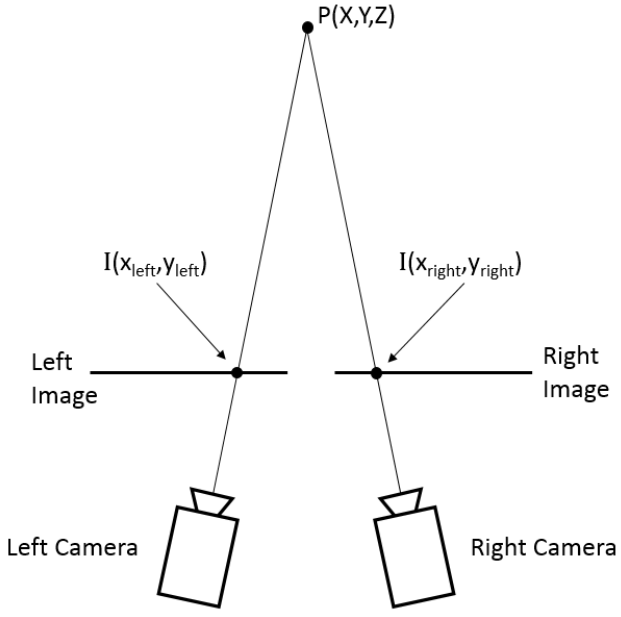

Figure 1.9: Multi-camera systems can be used to triangulate common points between the pair of images.

The heart of several three-dimensional reconstruction methods lies within the calibration. Several algorithms have been developed over the years to calibrate multi-camera systems, but the majority of calibration algorithms used today are based on the work done by Zhang et al. [61], Heikkila and Silven [24] and Tsai [55]. Each technique uses a planar object at different locations and orientations with sharp identifiable features, such as the corners of a checkerboard, to create a relationship between the cameras' X-Y coordinates to the real world's X-Y-Z coordinates. Zollner and Sablatnig [62] performed a study comparing the work of these three authors to determine the differences between them. Although each method produced overall accurate results; Tsai's method [55] performs best for applications where there is strong radial distortion, Zhang's approach [61] converges to the most accurate camera parameters in a multi-camera system, but Heikkila's [24] converges more quickly.

By performing a camera calibration the intrinsic and extrinsic parameters of the cameras are acquired. The intrinsic parameters contain information about the effective focal length, scaling factor and the principle point, which is the point at which the camera's optical axis intersects the image plane, while extrinsic parameters are used to translate between the cameras coordinates to real world coordinates.

The major steps remaining in creating a three-dimensional reconstruction are rectification, correspondence and reprojection [11]. Rectification adjusts the image pairs based on the translational and rotational differences identified in the calibration process. The images are manipulated so that the cameras appear as if they were parallel. The effect of this manipulation is that matching points between the images will lie in same pixel row. Shown in Figure 1.10a and b is a pair of stereo photos, and the anaglyph rectification of the image pair is shown in Figure 1.10c.

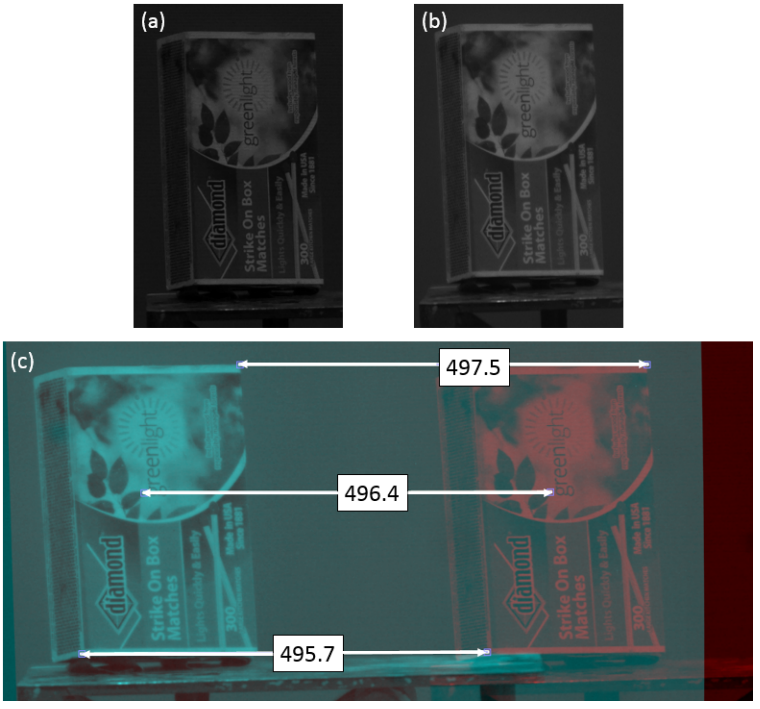

Figure 1.10: (a) Left and (b) right stereo images of a box of matches are used to create the (c) rectified anaglyph image using a MATLAB routine. Three distances, measured in pixels, between common points in the rectified image are shown.

Correspondence identifies the common points between the image pair and creates a disparity map, which provides a measure of depth in the image. The farther the distance between the common points, the closer that point is to the camera. Figure 1.11 shows the disparity map created by the images in Figure 1.10 with disparity range of 484 to 500 between the image pair. The depth information

created from the disparity map is then used to reproject the image pair as a single 3-D image shown in Figure 1.12.

In order to identify corresponding regions, there are two common algorithm choices, standard block matching and semi-global. The standard block matching method (sum of absolute differences) [20], compares pixel intensities of a given square size in the left and right image. If the sum of absolute difference between the image pair is equal to zero, this corresponds to a perfect match, and the distance between the square in the left and right image is calculated, providing a disparity. The default matching algorithm used by MATLAB is the semi-global method [25]. The semi-global method implements the sum of absolute differences, but incorporates a forcing function so that nearby regions have similar disparities.

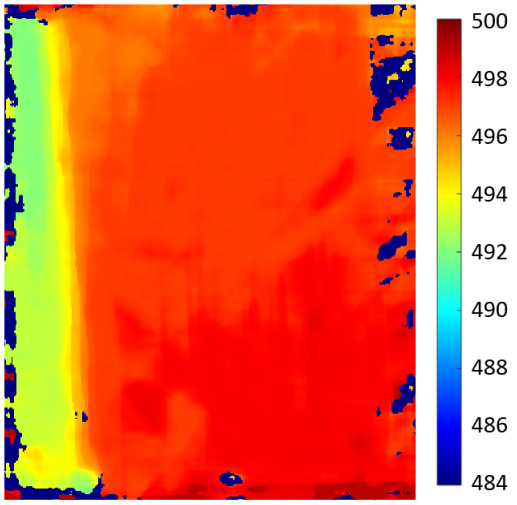

Figure 1.11: Disparity map created from the rectified image

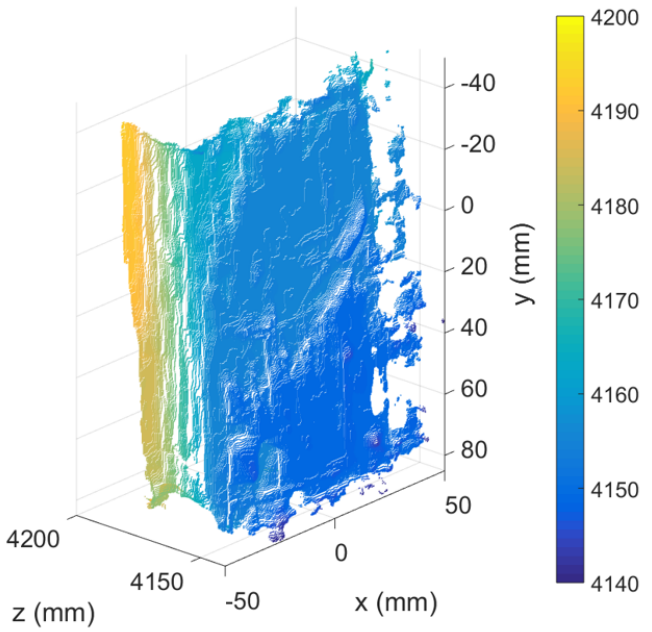

Figure 1.12: Three dimensional point cloud constructed from the disparity map

1.2.6 Stereo imaging with schlieren and shadowgraphy

Most studies that have performed stereo schlieren imaging had 10 to 15 degrees of separation between each setup to allow for left and right eye view [18, 47, 56]. However, this angle is not ideal for 3-D reconstruction. At least 70 percent overlap is recommended in the rectification of images, resulting in a disparity range of less than 256 pixels.

Wang performed some of the most recent work in stereoscopic schlieren and projective shadowgraph imaging [58]. In the work accomplished, the bursting of a bubble was tracked in three dimensions using a high-speed schlieren setup. Wang states that previous work done in stereo schlieren imaging was not truly stereoscopic because the test section with parallel light does not obey the characteristics of projective geometry. To work around this, Wang used a stereo z-schlieren system that created a test section in non-parallel light similar to the schematic in Figure 1.13.

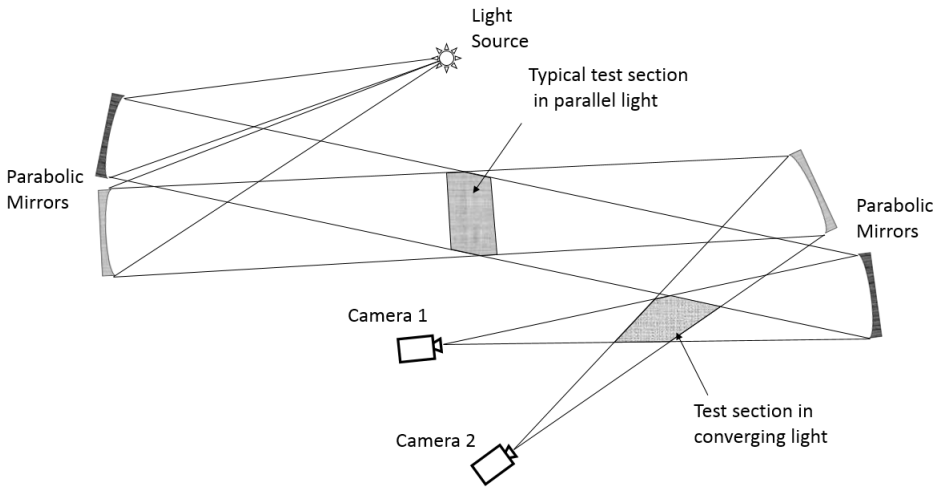

Figure 1.13: Stereo z-schlieren schematic creating an overlapping test section with non-parallel light.

In order to understand the projective geometry characteristics previously described, a transparent checkerboard was placed in the parallel light test section and in the converging light test section of a schlieren system as seen in Figure 1.14a. The checkerboard was then rotated equally in both directions. Figure 1.14b shows that the orientation of the checkerboard in the parallel light test section appears the same regardless of rotation; however, a clear difference in orientation can be identified in the converging light test section, Figure 1.14c.

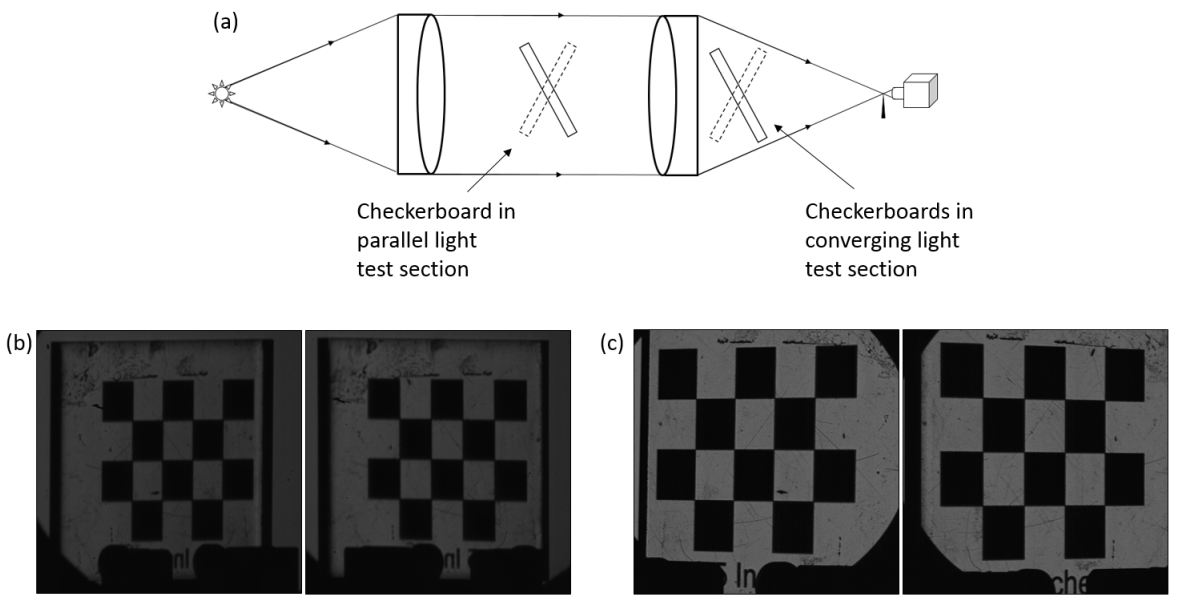

Figure 1.14: (a) Schlieren system with a transparent checkerboard placed in the parallel and converging light sections. (b) The orientation of the checkerboards in the parallel light cannot be determined, but (c) the rotation of the checkerboards in the converging light is easily observed.

Although visualizing fluid flow in a stereo schlieren setup with parallel light adds challenges because projective geometry isn't satisfied, this does provide a simplification in tracking. In a visualization technique with diverging light, such as projective shadowgraph setup or Wang's z-schlieren system, there is not a one-to-one correspondence between the physical object and the schlieren object [47], which creates a method of false tracking. This effect becomes increasingly more significant with larger test sections. Consider Figure 1.15 where a shock wave is initiated at the center of the schlieren setup, Figure 1.15a, and at the center of the shadowgraph setup, Figure 1.15b, and propagating outward. In projective shadowgraphy, the location where the light meets the shock wave is changing, but the parallel light in the schlieren system contacts the shock front in the same location as it expands. To account for the changing position in projective shadowgraphy, a geometry correction needs to be applied as discussed by Hargather and Settles [22].

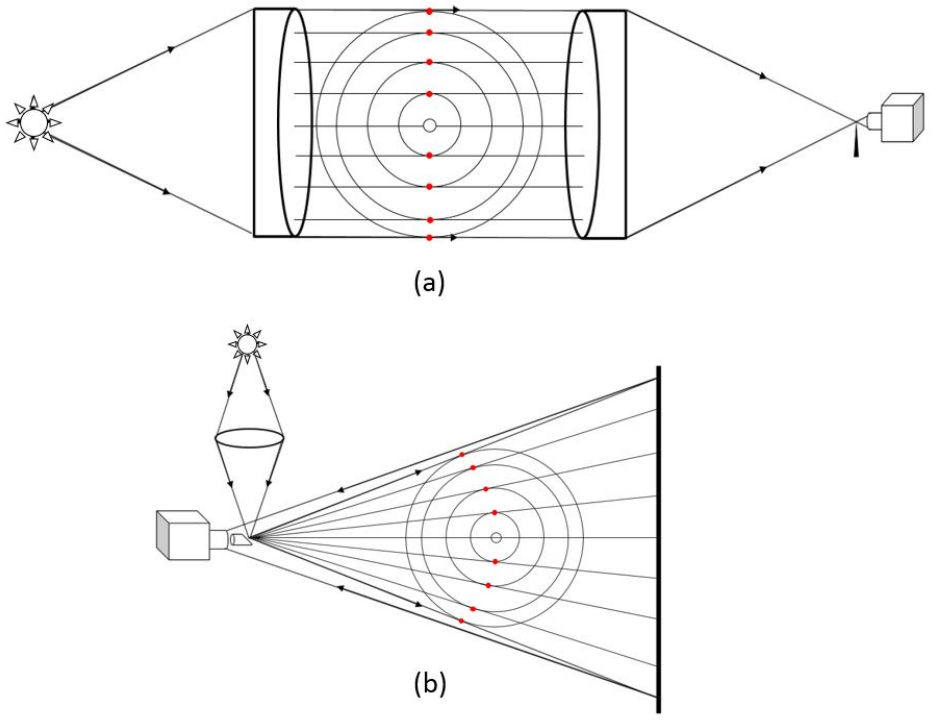

Figure 1.15: Location of the shock front as seen from (a) a schlieren setup and (b) projective shadowgraph system.

1.3 Goals of this research

The goal of this work is to use and validate stereo schlieren and stereo projective shadowgraph systems as techniques to visualize and track the turbulent mixing of a post detonation environment in three dimensions. The explosive tests will be validated by testing a helium jet in a stereo schlieren and stereo projective shadowgraph system. The data from the schlieren and shadowgraph studies using a helium jet will be compared to an ideal velocity obtained using PIV. This work will quantify errors and evaluate the appropriateness of stereo schlieren and stereo projective shadowgraphy.

CHAPTER 2

EXPERIMENTAL SETUPS

Five individual experimental analyses were performed here, involving helium jets and explosives imaged with a range of techniques. The helium jet was tested in a stereo schlieren setup and stereo projective shadowgraph setup. PIV analysis on the helium jet provides a baseline measurement of the velocity field for comparison with the schlieren and shadowgraph measurements. Explosive tests were then performed using stereo schlieren imaging and stereo projective shadowgraphy to measure shock wave and product gas three-dimensional positions and motions. This chapter details the optical diagnostic techniques and setups used to perform and analyze the experiments.

2.1 Optical diagnostic techniques applied

2.1.1 Stereo schlieren imaging

Two simple schlieren systems were set up in a stereo configuration with an angle of 2 degrees between the systems. Shown in Figure 2.1 and 2.2 is a schematic of the overall setup as well as images of emitting and receiving optics. On the emitting side of the schlieren systems, individual 5-Watt white LEDs (part no. 897-LZ100CW00 from Mouser Electronics) were used as the point light source. The light was collimated using 700mm focal length schlieren lenses (L1). For the receiving optics, 900mm focal length schlieren lenses (L2) were used, followed by the cutoff tools (CT), -200mm negative meniscus lenses (L3) and high-speed cameras. The negative meniscus lenses allow for an increase in focal length and are discussed in detail in Section 2.1.2.

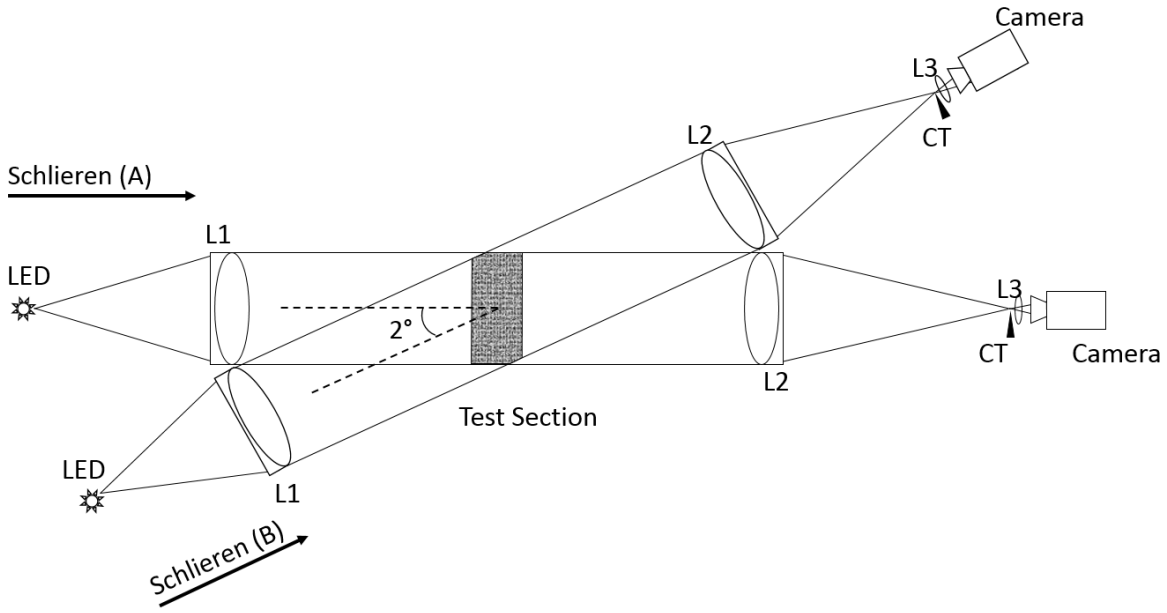

Figure 2.1: Stereo schlieren schematic with a 2 degree angle variation between systems Schlieren (A) and Schlieren (B). The total length of each schlieren system from LED to camera was 11 meters with the test section centered at 5.5 meters.

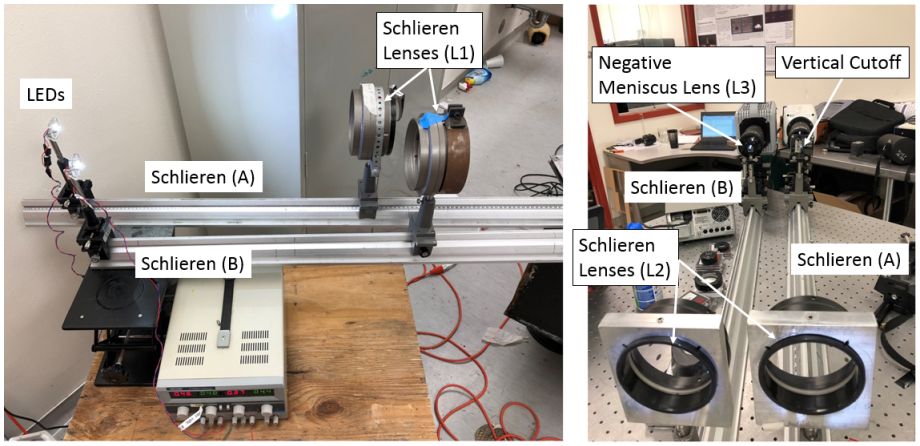

Figure 2.2: (a) Emitting and (b) receiving optics used in the stereo schlieren system.

2.1.2 Effect of negative meniscus lenses in a schlieren system

In order to achieve a small angle variation between cameras in the stereo schlieren setup, long schlieren systems were built to accommodate the width of

the optical equipment. Due to the extreme length of the system, the cameras could not focus on the schlieren object 5.5m away. To overcome this, negative meniscus lenses were used to increase the distance the cameras could focus.

Parallel light converges to the focal point after it passes through a positive lens. Conversely, in a negative lens, parallel light diverges after the light passes through it. The diverging beams can be traced back to a point, which lies before the light passes through the lens giving a "negative" focal length. The two lens types are illustrated in Figure 2.3.

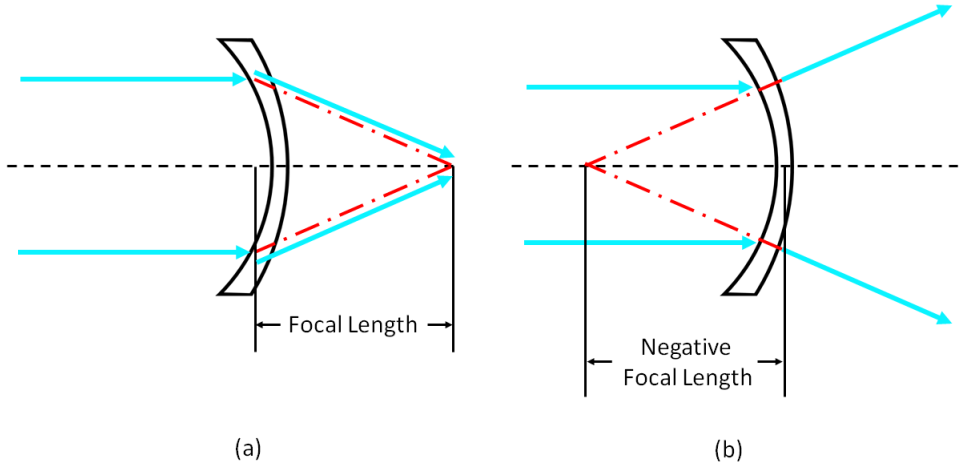

Figure 2.3: (a) A positive meniscus lens, converges parallel light to a point at the lens's focal length whereas (b), a negative meniscus lens, diverges parallel light creating a negative focal length.

The use of negative meniscus lenses in a schlieren system has not yet been characterized in the literature. A brief study was performed here to determine the effect of different camera lenses, negative meniscus lenses (L3) and the receiving schlieren lens (L2) had on the distance the camera was able to focus. The threads of a 1/4"-20 bolt were used as the object to focus on, and the distance measured began where the camera lens attaches to the camera, shown in Figure 2.4. This point was chosen because it could remain a fixed point while testing different schlieren and camera lenses.

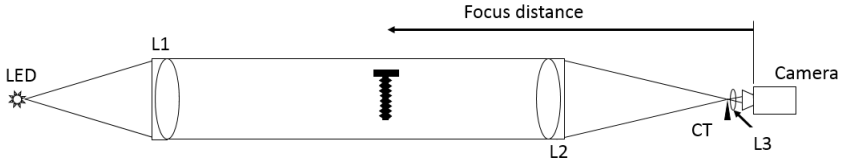

Figure 2.4: Schematic of the negative meniscus lens focusing test. The threads of a 1/4"-20 bolt were used to identify when the camera was focused, and the distance was measured from where the camera lens meets the camera.

It was determined that different camera lenses had negligible effect on the camera's focus distance. Figure 2.5 shows the relationship between negative meniscus lenses and schlieren lenses. The points on the plot represent a minimum and maximum focus distance that were measured.

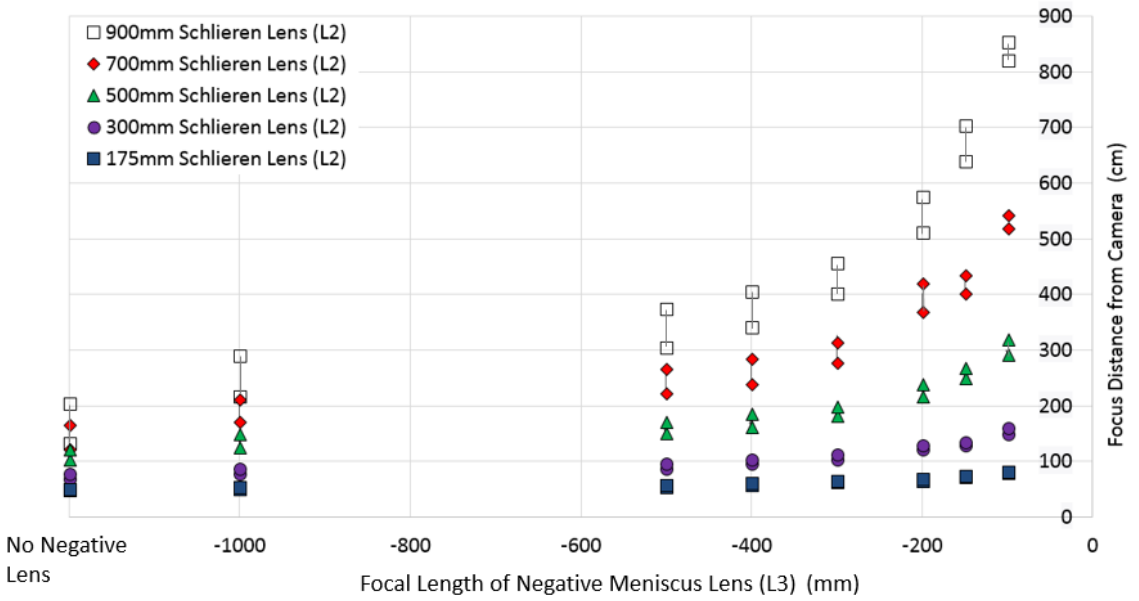

Figure 2.5: Effect of negative meniscus lenses (L3) and receiving schlieren lenses (L2) on a camera's focus distance in a schlieren system.

A clear relationship between focus distance, schlieren lens (L2) and negative meniscus lens (L3) can be observed in Figure 2.5. For all of the schlieren lenses, the focus distance increases when a negative meniscus lens is added. This effect is amplified for schlieren lenses with longer focal lengths. The focus distance of the camera without a negative meniscus lens is also plotted and represents a focal length of negative infinity. As the focal length of the negative meniscus lens increases from negative infinity toward zero, the distance that the camera is able to focus increases at a non-linear rate. It can also be observed that the schlieren lens' focal length is the dominant factor in determining the depth of the camera's focus range.

2.1.3 Projective shadowgraphy

Two stereo projective shadowgraph systems were used in this work based on the light requirements for the test. These configurations are shown in Figures 2.6 and 2.7. Figure 2.6 uses 5-Watt white LEDs (part no. 897-LZ100CW00 from Mouser Electronics) as the light sources. Two short schlieren systems were used to focus the light onto the rod mirror. A 300mm focal length lens was used to

collimate the light and a 175mm focal length lens was used to focus the light onto the rod mirror. This setup allowed for a camera separation angle of 2 degrees.

Figure 2.7 replaces the LED light sources with a 1kW arc lamp. This is because explosive tests require more light to prevent the image from becoming washed out from the direct illumination created by the blast. In order to transport the light from a single arc lamp to both cameras, a focusing lens was used to bring the light of the arc lamp to a point on a triangular mirror. The light then passes through a short schlieren system, using the same 300mm and 175mm focal length lenses, to focus the light onto the rod mirrors. The resulting angle between each camera in this setup was 14 degrees.

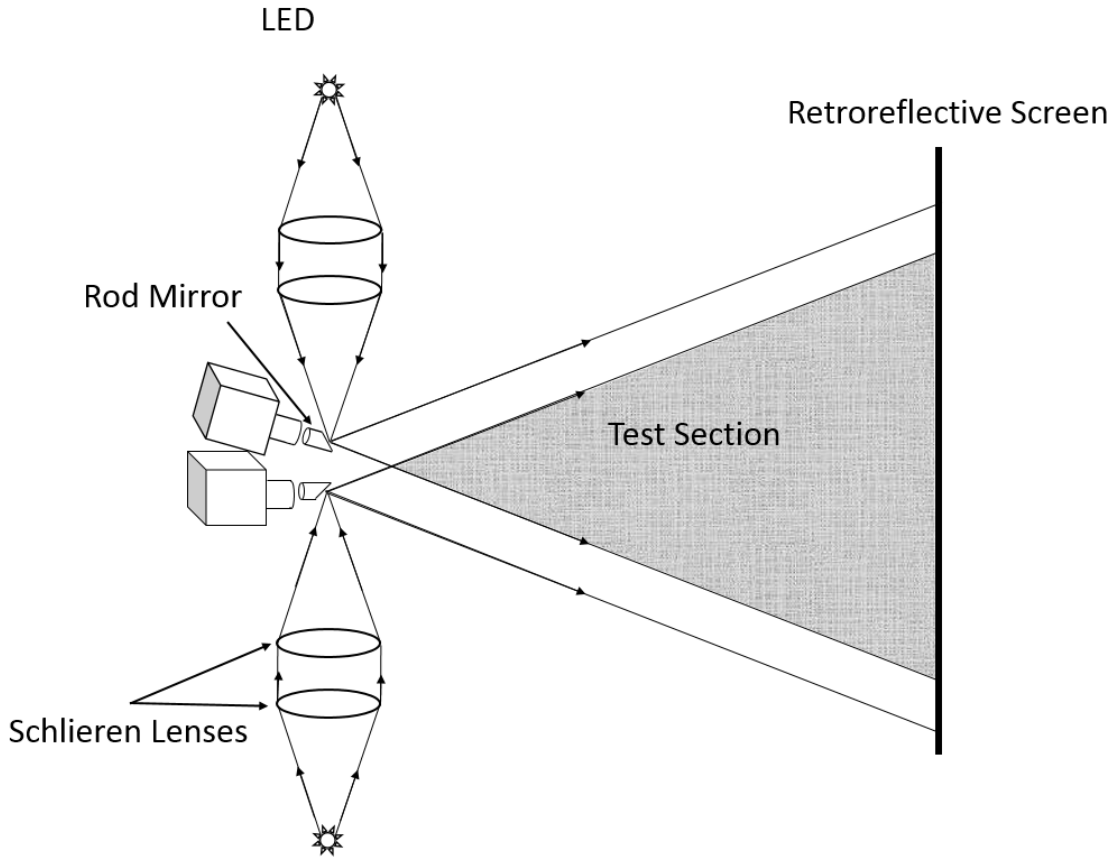

Figure 2.6: Stereo projective shadowgraph system with low light requirements and a camera separation angle of 2 degrees.

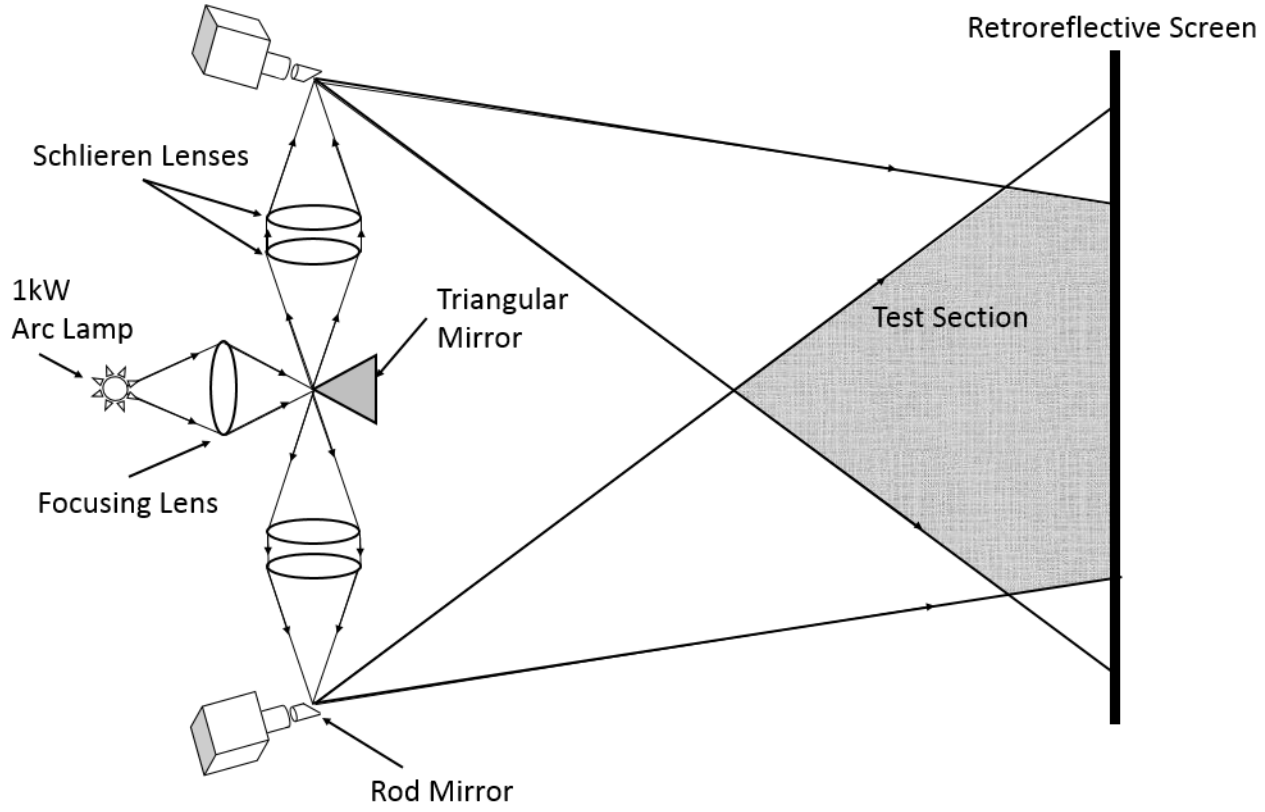

Figure 2.7: Stereo projective shadowgraph system with a high light requirement and a camera separation angle of 14 degrees.

2.1.4 Particle Image Velocimetry (PIV)

A continuous laser sheet developed at New Mexico Tech [8] was used to illuminate the seed particles. This was used instead of a traditional pulsing laser to allow for the use of a regular high speed camera to capture the event with temporal resolution set by the camera frame rate. Figure 2.8 shows an overview of the PIV setup. The exhaust and seeding system are contained in an acrylic box to mitigate any external influences on the flow. The laser sheeting optics are mounted above the test section and aligned with the exhaust.

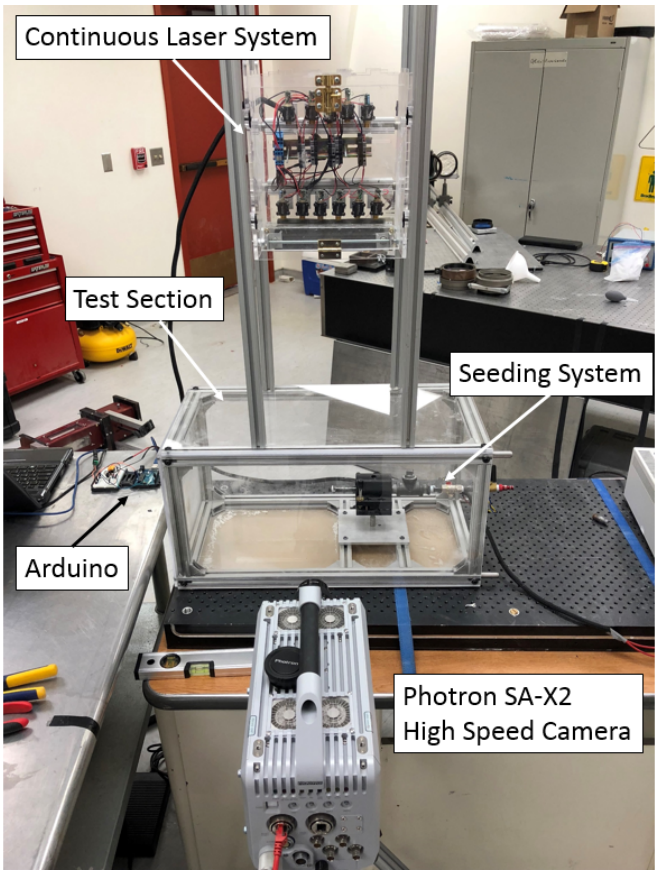

Figure 2.8: Overview of PIV setup

A detailed image of the helium jet and seeding system is shown in Figure 2.9. The seeding system is comprised of 1/4 inch and 1/2 inch NPT nipples, adapters and fittings, a ball valve and electronic valve. The ball valve is used to throttle the flow for proper seeding. The electronic valve, which is controlled by a switch installed on an Arduino, is used to consistently open and close the system to run individual tests without having to adjust the ball valve. The desired seeding particles are loaded into the seeding chamber and are dispersed into the flow by the ball bearing chamber. The ball bearing chamber contains 100-200 4.5mm ball bearings and acts as a fluidized bed to distribute the solid particles into the flow with less particle clumping.

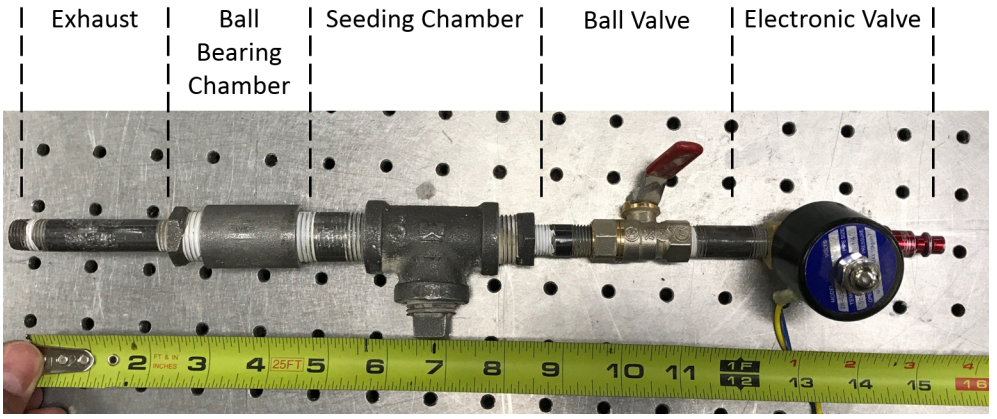

Figure 2.9: Details of the seeding system used for PIV testing.

2.2 Experiments performed

2.2.1 Helium jet

Jets are simple fluid-dynamic flow fields that have been heavily studied [10, 29]. A helium jet is used here to increase the visibility of the jet in the schlieren and shadowgraph systems. A two-dimensional particle image velocimetry (PIV) analysis was performed on the helium jet to obtain velocities that will be used to compare and validate the two-dimensional and three-dimensional schlieren image velocimetry (SIV) data collected in the stereo schlieren and projective shadowgraphy systems.

To perform the PIV experiment with the helium jet, a helium gas cylinder was attached to the PIV seeding system and regulated to 205 kPa. 5 grams of silver-coated hollow-glass spheres (part no. 10089-SLVR from TSI Incorporated) were added to the seeding chamber for each PIV test. A Photron SA-X2 high-speed camera was used to record each test at 50,000 frames per second with an exposure of 10 μs at an image resolution of 768x328 pixels and a spatial resolution of 0.16 mm/pixel. This provided a minimum of 30,000 frames (0.6 seconds) of usable test data. The data were analyzed using PIVlab, which is an open source software for MATLAB to perform PIV [51, 52, 53].

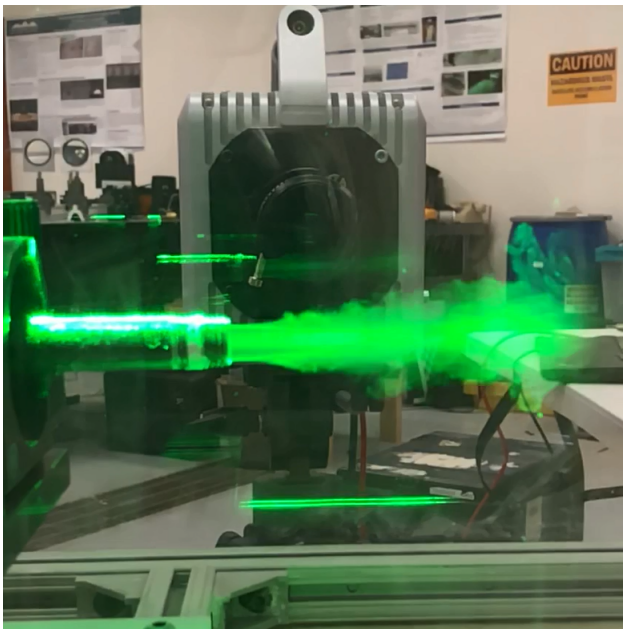

Figure 2.10: Visualization of helium jet using the continuous PIV laser system.

The helium jet was moved into the test section of the stereo schlieren system, identified in Figure 2.1, to perform a two-dimensional and three-dimensional SIV analysis. A Phantom v711 and Photron SA-X2 high-speed cameras recorded the jet at 40,000 frames per second with an exposure of 1μs at an image resolution of 512x256 pixels and a spatial resolution of 0.16 mm/pixel. The cameras were calibrated using a 4x5 checkerboard with 6.35mm squares and synchronized using a Stanford DG535 Pulse Generator. A vertical knife edge, horizontal knife edge, circular cutoff and no cutoff were tested to provide a complete study of tracking turbulent structures in a schlieren system with varied cutoffs.

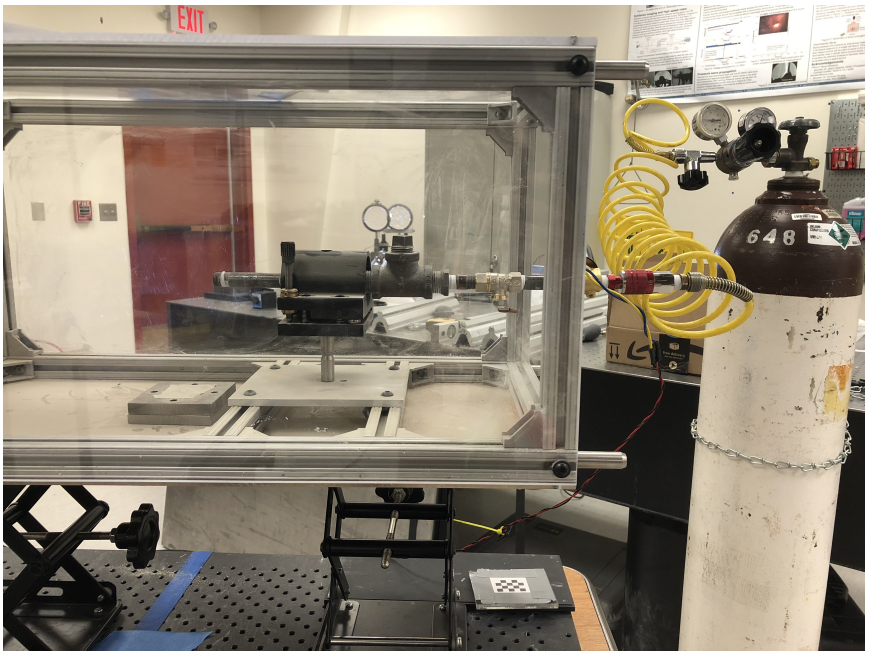

Figure 2.11: Helium jet placed in the stereo schlieren setup.

The Phantom v711 and Photron SA-X2 high-speed cameras were also used to record the helium jet in the stereo projective shadowgraph setup shown in Figure 2.6. They recorded the jet at 40,000 frames per second with an exposure of 24μs at an image resolution of 512x256 pixels with a 2 degree angle between each other. Due to the limitations of the camera lenses a pixel resolution of only 0.635 mm/pixel was achieved. The cameras were calibrated using a 5x8 checkerboard with 19.05 mm squares and synchronized using a Stanford DG535 Pulse Generator. Figure 2.12 shows an overview of the stereo projective shadowgraph setup.

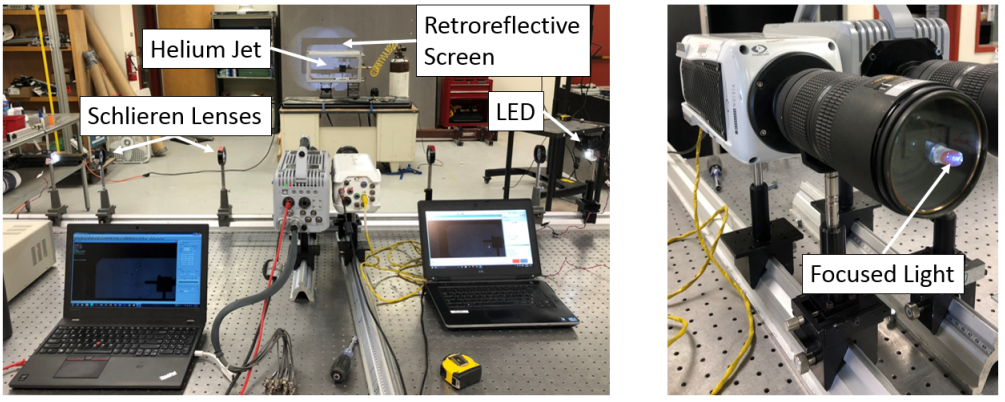

Figure 2.12: (a) Overview of the stereo projective shadowgraph test setup. (b) A schlieren system is used focus the light onto each rod mirror.

2.2.2 Explosive testing with stereo schlieren imaging

The Tunnel for High-speed Optical Research (THOR) was used to detonate and visualize a series of explosive tests in the stereo schlieren system. THOR, shown in Figure 2.13, can be broken down into three major sections: the driver section where the explosives are initiated, the optical section, which is used for viewing and capturing the event, and the exit section. Details of THOR can be found in [3, 50].

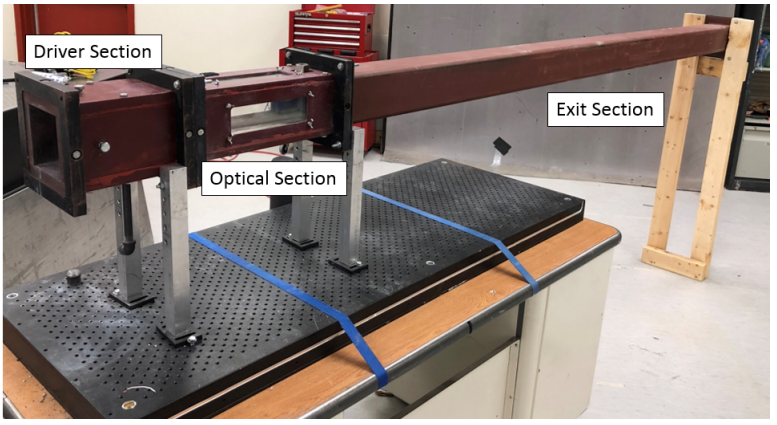

Figure 2.13: The major sections of the Tunnel for High-Speed Optical Research (THOR) outlined.

Each test detonated 400mg of PETN powder and was initiated with an RP-2 detonator. Only a vertical cutoff tool and focused shadowgraphy were used to visualize the tests. It was discovered in the analysis of the helium jet that these cutoff types yielded the most accurate velocity calculations in a schlieren system. This is in concurrence with the results of Biwas and Qiao [10].

To begin test setup, the powder containment fixture (Figure 2.14a) is loaded with the desired explosive configuration and is sealed with masking tape on both sides to prevent spilling of the explosive mixture. The powder containment fixture is set into the positioning block (Figure 2.14a), followed by the detonator plate (Figure 2.14a) which are then bolted together to create the firing block assembly (Figure 2.14b). The firing block assembly is then inserted into the driver section of THOR and secured (Figure 2.14c). A Swagelok fitting is threaded into the detonator plate to hold and align the RP-2 detonator with the explosives.

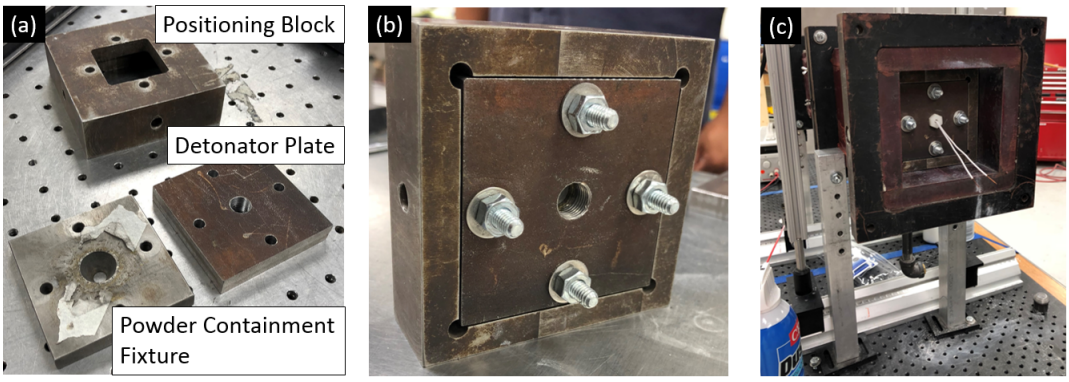

Figure 2.14: (a) THOR firing block pre-assembly, (b) post-assembly and (c) secured into the driver section of THOR.

Three types of tests were conducted as illustrated in Figure 2.15 and the details of each test is tabulated in Table 2.1:

1. Bare PETN (Pentaerythritol Tetranitrate)
2. PETN with ball bearings deposited on the surface of the charge
3. PETN with ball bearings homogeneously mixed into the charge.

A Phantom v711 and Photron SA-X2 high-speed camera recorded the tests at 40,000 frames per second with an exposure of 1μs at an image resolution of 512x256 pixels and a spatial resolution of 0.16 mm/pixel. The cameras were calibrated using a 4x5 checkerboard with 6.35mm squares and synchronized using a Stanford DG535 Pulse Generator.

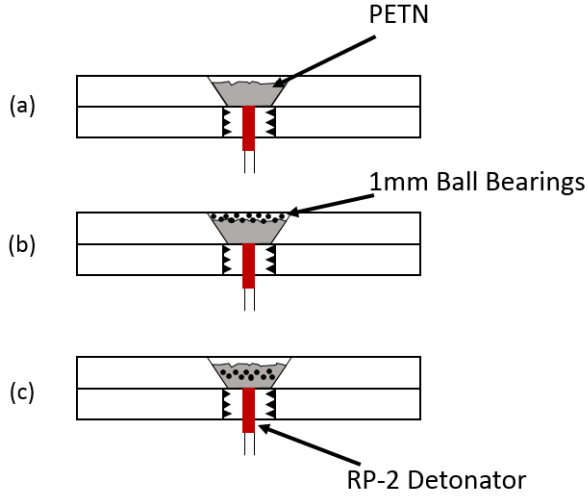

Figure 2.15: Different test configurations used in THOR: (a) bare PETN, (b) ball bearings placed on top of the PETN and (c) ball bearings mixed in with the PETN.

Table 2.1: THOR test sequence and details

Test Number	Test Type	Cutoff
1*	Bare PETN	Vertical
2	Mixed Bearings	Vertical
3	Mixed Bearings	Vertical
4	Bare PETN	Vertical
5	Mixed Bearings	None
6	Bare PETN	None
7	Surface Bearings	None

* Only this test was analyzed in this work.

2.2.3 Field explosive testing using stereo projective shadowgraph

A series of cylindrical HMX explosive pellets were tested at the outdoor Eagle Test Site at the Energetic Materials Research and Testing Center (EMRTC) at New Mexico Tech. Each test used four high-speed cameras. One pair of the cameras was setup as a horizontal stereo projective shadowgraph pair, as described by Figure 2.7, to capture the shockwave, fireball and resultant turbulent gases. The other pair of cameras, identified as Cameras 1 and 2 in Figures 2.16 and 2.17 were used for work unrelated to this study and are discussed in [8]. The cameras used in the shadowgraph system are Photron SA-Z high-speed cameras, and are shown as Cameras 3 and 4 in Figures 2.16 and 2.17. Barriers with plexiglass windows were placed in front of the cameras to provide shielding from potential fragments. The spatial resolution for each camera was approximately 1 mm/pixel. Further details about the camera operating features are shown in Table 2.2.

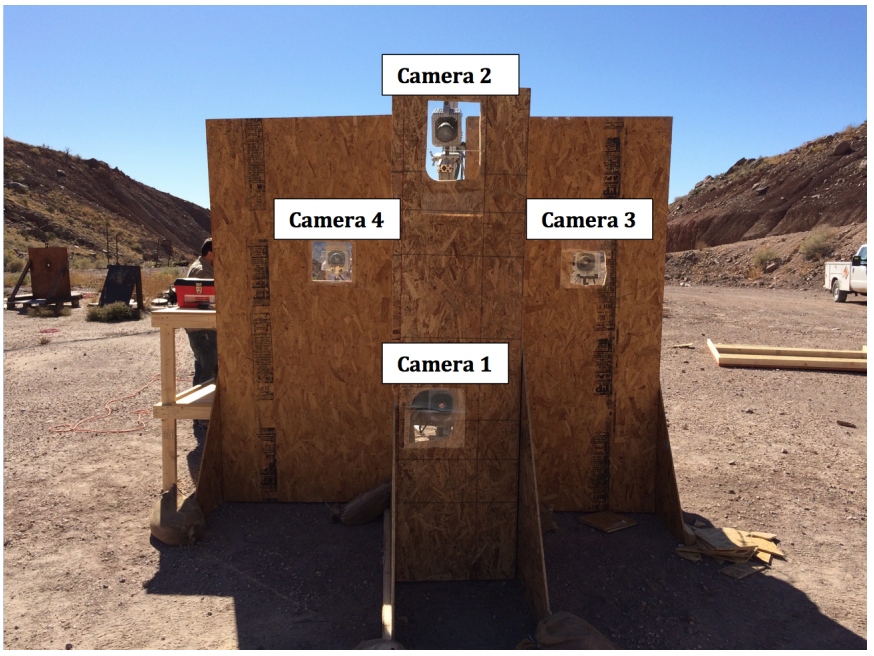

Figure 2.16: The stereo projective shadowgraph system is shown by cameras 3 and 4 at an angle of 14 degrees between each setup. Cameras 1 and 2 were not used in this work.

An image of the overall setup for the stereo projective shadowgraph field-scale test is shown in Figure 2.17. The high-speed cameras are in the mounting on the left, the shadowgraph screen is on the right and the explosives were placed on the wooden table between the cameras and the screen.

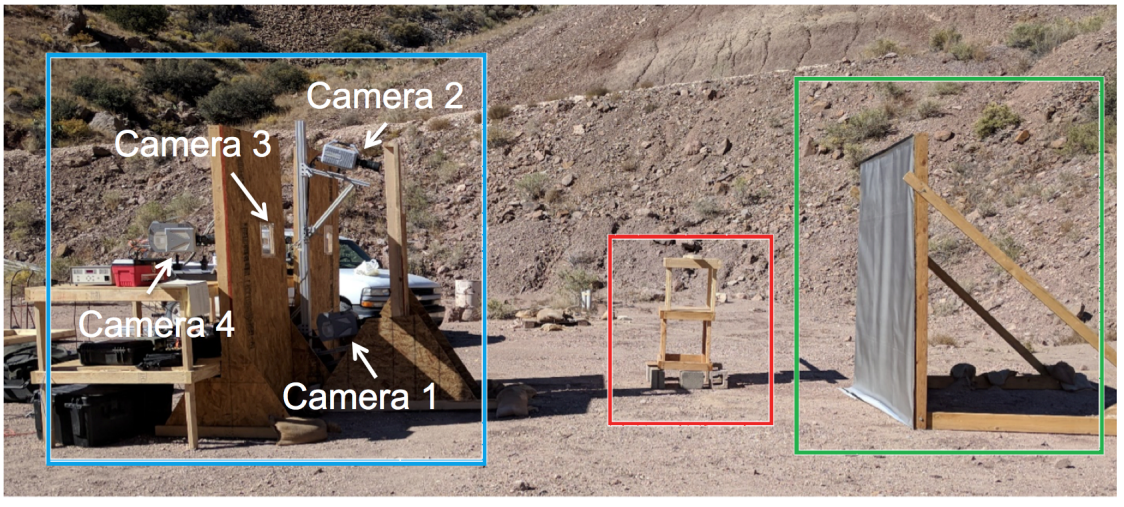

Figure 2.17: Projective shadowgraph field test setup

Table 2.2: Camera feature details for each test

Test	Frame rate (fps)	Shutter speed (μs)	Resolution
1	20000	1.25	1024x1024
2	20000	1.25	1024x1024
3	40000	2.5	1024x512
4	40000	2.5	1024x512
5	40000	2.5	1024x512
6*	40000	2.5	1024x512
7	40000	2.5	1024x512
8	40000	5	1024x512
9	40000	2.5	1024x512

* Only this test was analyzed in this work.

Nine individual explosive tests were conducted with pressed explosive pellets comprised of 98% HMX, 1.5% binder and 0.5% graphite. Each pellet had a diameter of 1 inch and an approximate height of 1 inch. Three types of pellets were fabricated for this test series:

1. bare HMX pellets
2. pellets with bearings deposited on the surface of the pellet, and
3. pellets with bearings homogeneously mixed in with the explosive.

The steel bearings used were 1mm in diameter. The three pellet designs can be seen in Figure 2.18. From left to right is a bare HMX charge, an HMX charge with bearings pressed onto the surface and an HMX charge with bearings mixed with explosive prior to pressing.

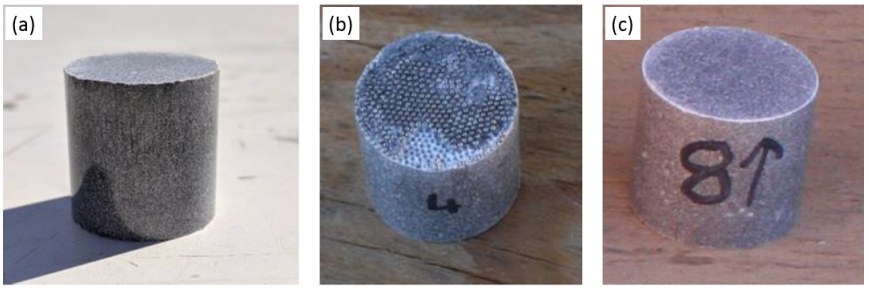

Figure 2.18: Different pellet designs for explosive stereo projective shadowgraph test: (a) bare HMX, (b) bearings deposited on the surface and (c) bearings mixed into the charge.

The charges were held in floral foam that was secured to the blast table. The HMX pellets were in direct contact with the RP-2 detonators that were used to initiate the event. For tests 1 through 7, the detonator was placed axially behind the pellet. However, for tests 8 and 9, the detonator was placed orthogonally to

the explosive's axial axis. These different configurations are shown in Figure 2.19. Details of each pellet and testing sequence are provided in Table 2.3.

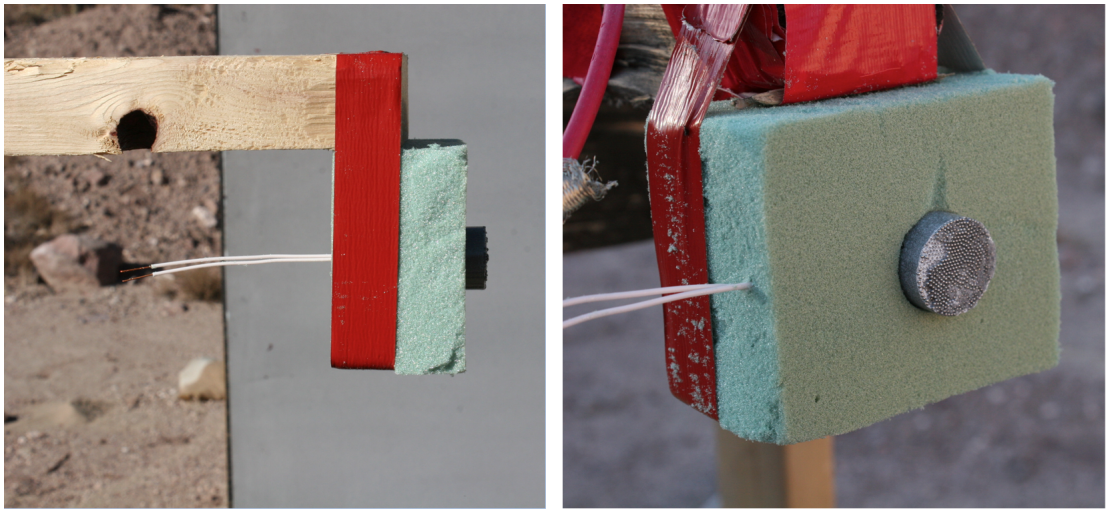

Figure 2.19: Detonator placement: (left) rear of the explosive and (right) orthogonally to the explosive.

Table 2.3: Explosive projective shadowgraph details and test sequence

Test number	HMX mass (g)	L/D	Pellet configuration	Maximum loading pressure (tons)	Detonator location
1	19.97	0.892	Bare HMX	12	Rear
2	21.94	0.903	Surface Bearings	10	Rear
3	21.89	0.900	Surface Bearings	10	Rear
4	21.70	0.923	Surface Bearings	10	Rear
5	20.06	0.885	Bare HMX	10	Rear
6*	22.25	0.890	Mixed Bearings	10	Rear
7	21.90	0.892	Mixed Bearings	10	Rear
8	21.65	0.908	Surface Bearings	10	Orthogonal
9	23.48	1.013	Bare HMX	15	Orthogonal

* Only this test was analyzed in this work.

CHAPTER 3

VISUALIZATION ENHANCEMENT AND RECONSTRUCTION

3.1 Image processing

Image processing was used to improve the visualization of the fluid flow in SIV. Flow features were enhanced through image subtraction and histogram stretching in order to reduce background noise and increase contrast. This section discusses the process used to transform the test images, using a schlieren image of a helium jet with a vertical cutoff as an example, and shows the final transformation for all cutoff variations. This same general process was used for all testing. Shown in Figure 3.1 are raw schlieren images of the helium jet during and just before testing.

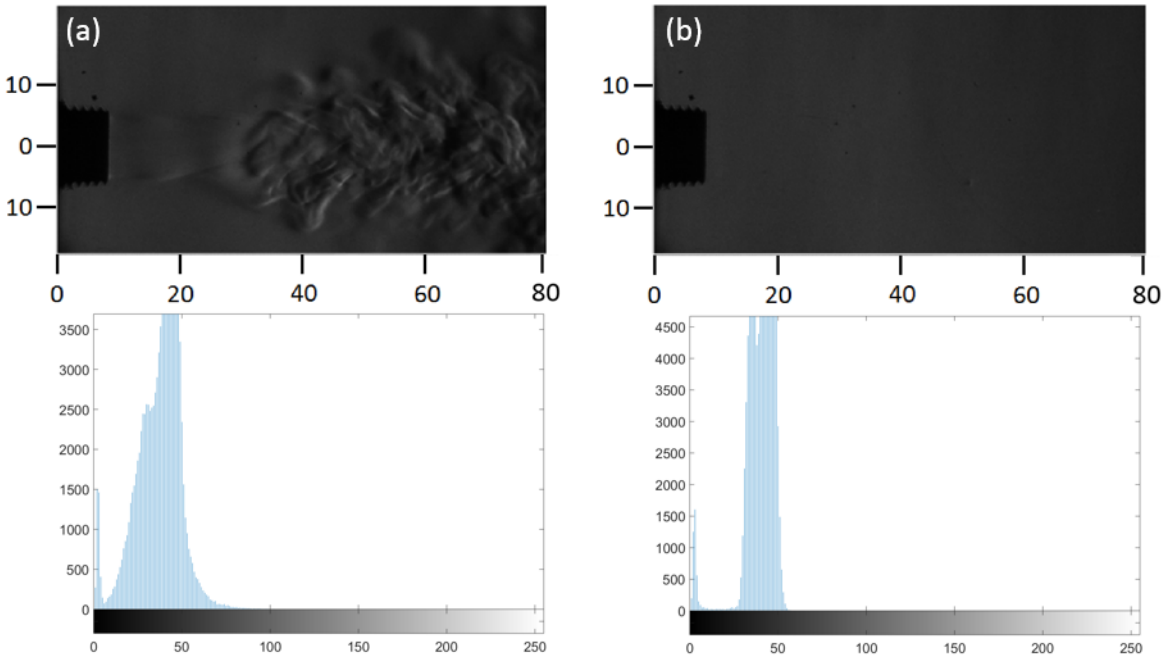

Figure 3.1: (a) Raw schlieren image of a helium jet and (b) tare image with their corresponding histograms. The dimensions listed are in millimeters.

The test and tare images are first converted from 8-bit unsigned integers to double-precision matrices before any image manipulation is performed. The algorithm used to process the images in MATLAB is given by: Equations 3.1 through 3.3. The tare image intensity, I_{tare} at each pixel location is subtracted from the test image intensity I_{test} to produce the new image intensity $I_{subtracted}$. The result of this subtraction is shown in Figure 3.2a. Next, Equation 3.2 is used to determine the pixel range of the subtracted image, R, by subtracting the minimum pixel value, P_{min}, from the maximum pixel value, P_{max}. Equation 3.3 is then used to produce the image in Figure 3.2b, where b is the image's bit depth, which is 12 for the cameras used.

$$I_{subtracted} = I_{test} - I_{tare} \tag{3.1}$$

$$R = (P_{max} - P_{min}) \tag{3.2}$$

$$I_{processed} = \frac{I_{subtracted} + \frac{R}{2}}{2^b} \tag{3.3}$$

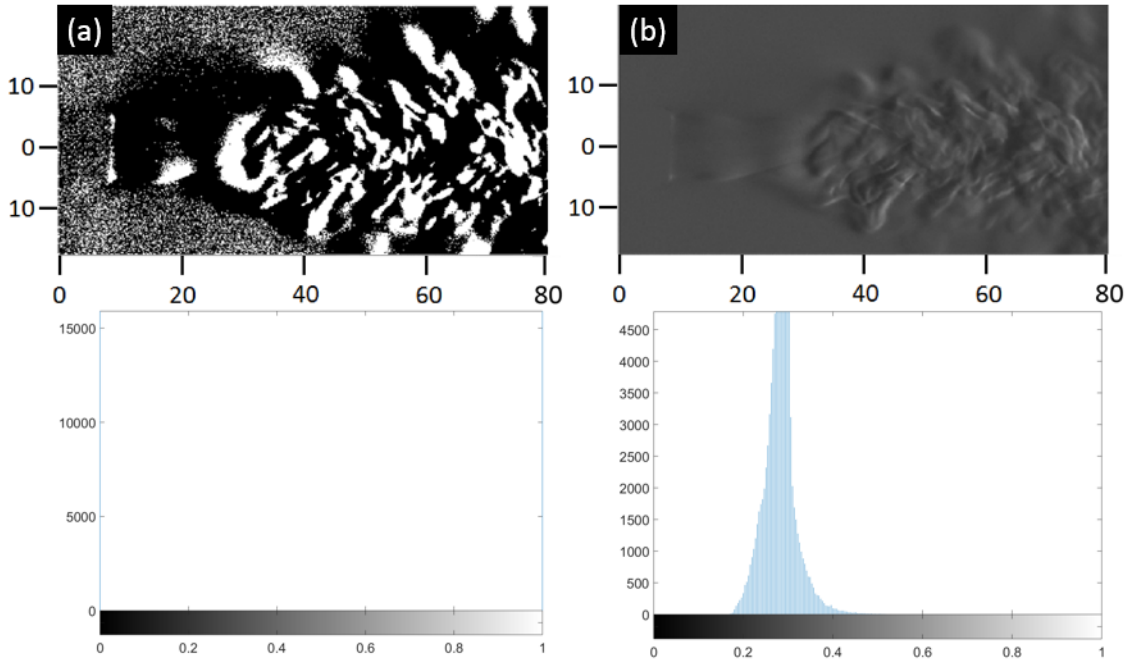

Figure 3.2: (a) Result of subtracting the tare image from the test image using Equation 3.1 and (b) the effect of applying Equations 3.1 through 3.3 and their corresponding histograms. The dimensions listed are in millimeters.

Because only a narrow band of pixel intensities is used, the histogram is stretched to use a larger range of pixel values to increase the image's contrast.

Figure 3.3 shows the raw test images and histograms for the vertical cutoff (a), horizontal cutoff (b), circular cutoff (c), focused shadowgraphy (d) and projection shadowgraphy (e), and Figure 3.4 shows the processed images and histograms for each scenario.

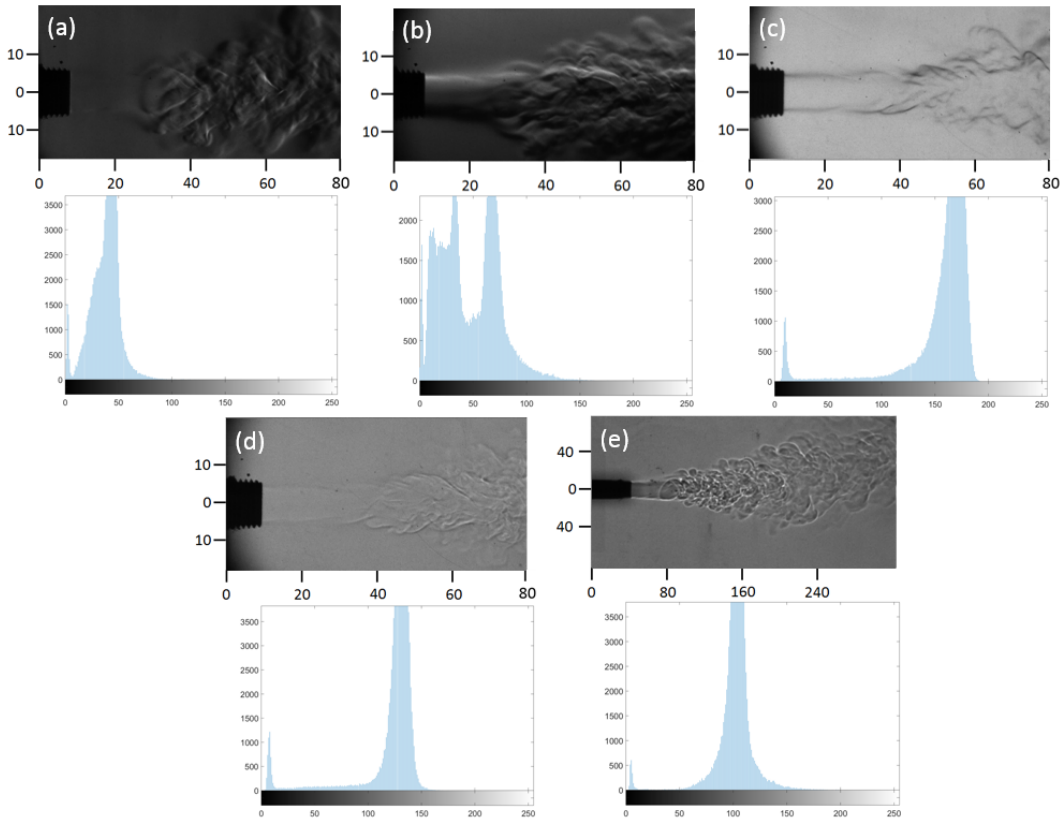

Figure 3.3: Raw helium jet images and histograms for the (a) vertical cutoff, (b) horizontal cutoff, (c) circular cutoff, (d) focused shadowgraphy and (e) projection shadowgraphy of the helium jet. The dimensions listed are in millimeters.

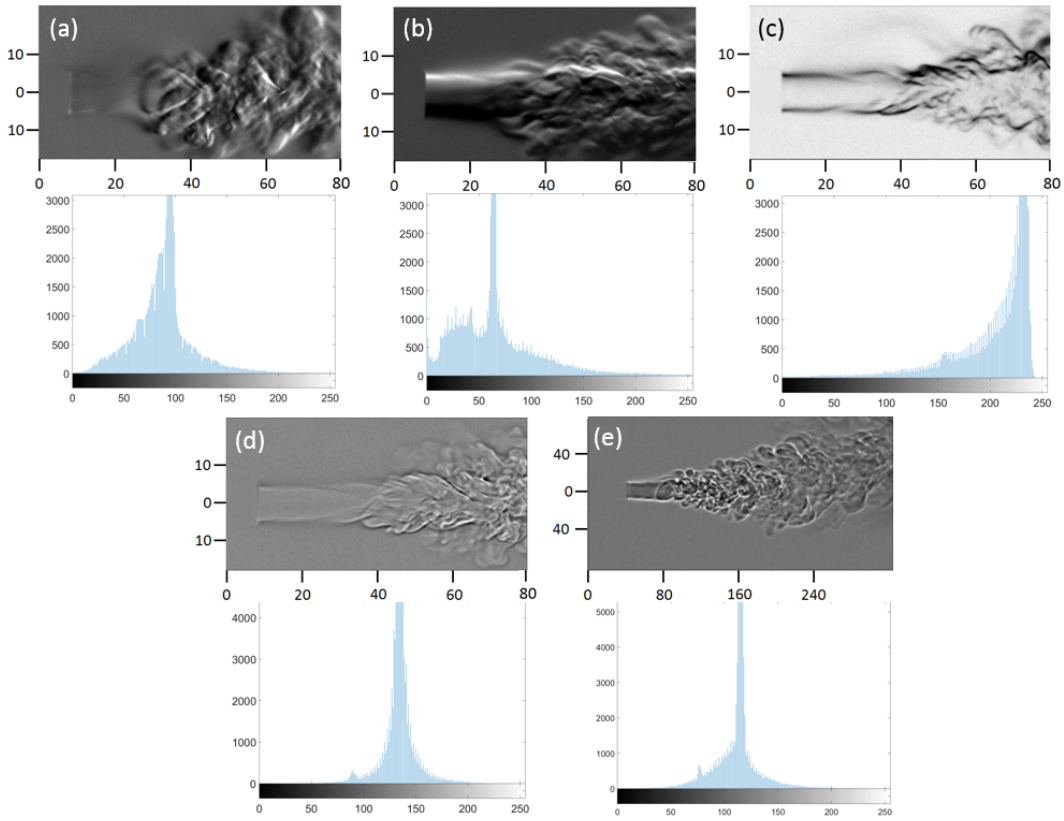

Figure 3.4: Final processed images and histograms for the (a) vertical cutoff, (b) horizontal cutoff, (c) circular cutoff, (d) focused shadowgraphy and (e) projection shadowgraphy of the helium jet. The dimensions listed are in millimeters.

3.2 Stereo image reconstruction at large angles

MATLAB provides thorough tutorials on how to calibrate a stereo camera system using their Stereo Camera Calibrator App, rectify the stereo images and reproject those images into three-space using built in functions [35]. However, the MATLAB routine is optimized for stereo camera setups that will produce a disparity less than 256 pixels. Due to the cameras and optical equipment used in this study, the disparities obtained during testing ranged from as low as 500 to 600 up to 2000 to 2300. This disparity is heavily dependent on obtaining a small angle between the stereo cameras, and having their optical axes parallel. This section outlines how to calibrate and verify the stereo parameter output; the two methods used to obtain 3-D positions of the test data; and characterizes the relationship between angle variation in a stereo camera system with the quality of 3-D reconstruction.

3.2.1 Stereo camera calibration

The calibration images of the checkerboard target are uploaded to MATLAB's Stereo Camera Calibrator App. Figure 3.5 shows the product of a calibration checkerboard with sections enlarged to show the difference between the initially detected checkerboard corner and the reprojected corner using the calibrated parameters.

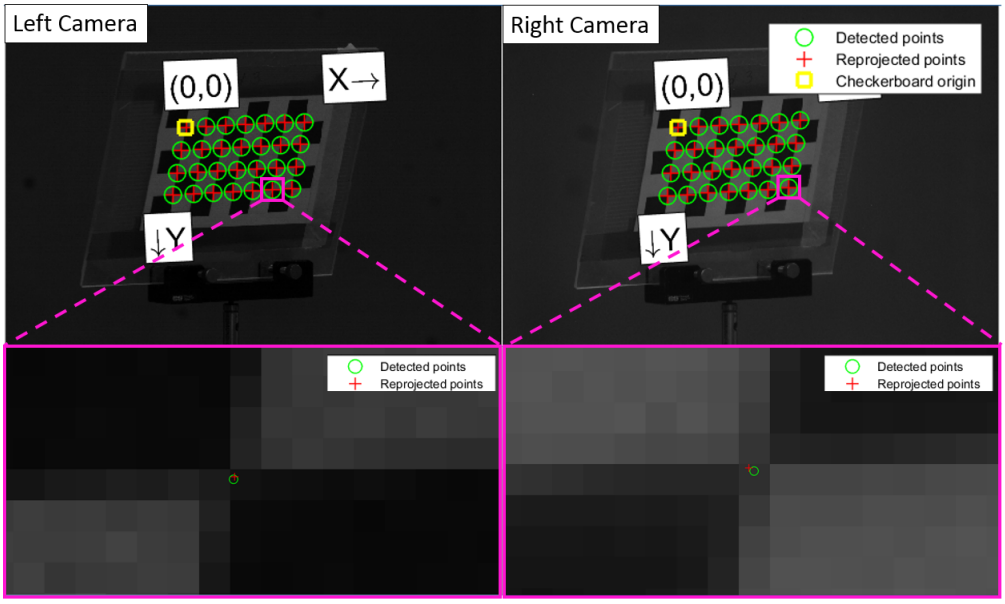

Figure 3.5: Output of stereo camera calibration showing the small difference between the initial detected corner and reprojected point using the stereo camera calibration.

The calibration app provides multiple outputs that can be used to validate the accuracy of the calibration. Shown in Figure 3.6 are the measured difference between the detected checkerboard corner and reprojected corner for each image. Images with excessive differences (less than 0.5 pixel error is ideal) can be quickly identified, removed from the calibration, and the calibration is re-run to improve the accuracy. The extrinsic view maps the stereo camera pair and calibration boards in real world coordinates as shown in Figure 3.7. The displayed real world coordinates can be compared to the dimensions of the physical setup. The third validation approach rectifies the stereo image pair and produces horizontal lines which, if the calibration is accurate, should intersect common points on the image pair as shown in Figure 3.8.

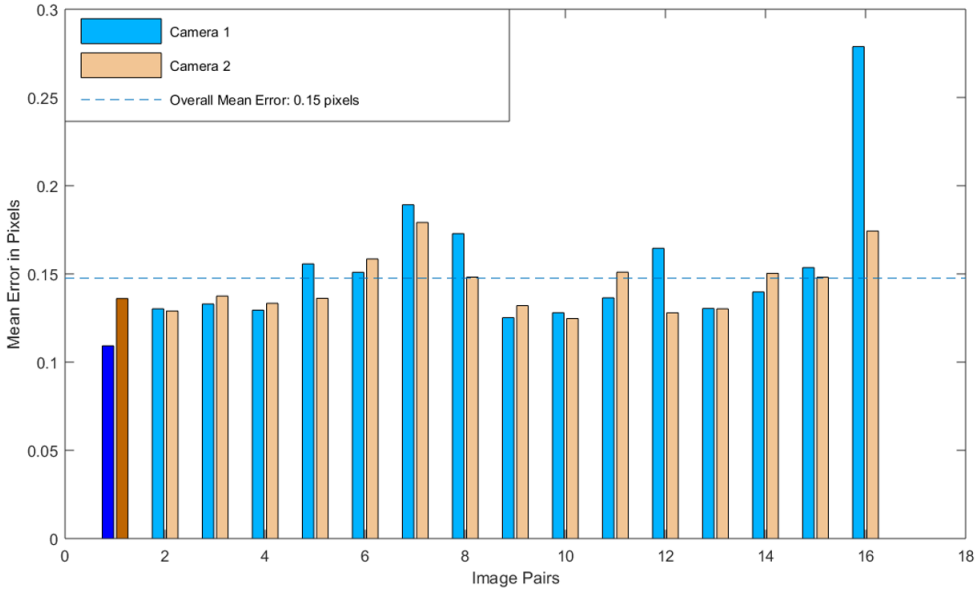

Figure 3.6: The reprojection errors are shown for the camera calibration with a separation angle of 2 degrees.

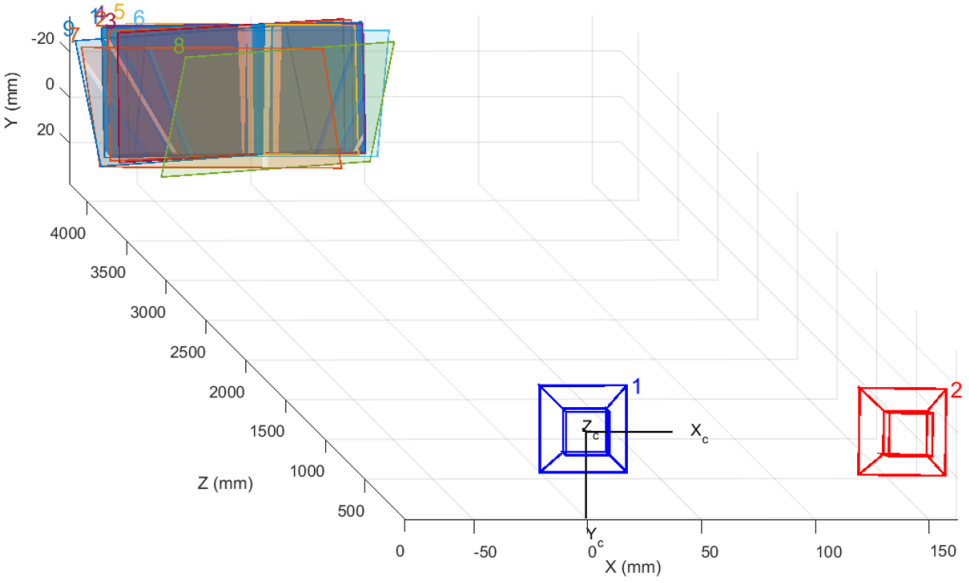

Figure 3.7: Extrinsic view showing the stereo camera pair as well as the locations and orientations of the calibration boards.

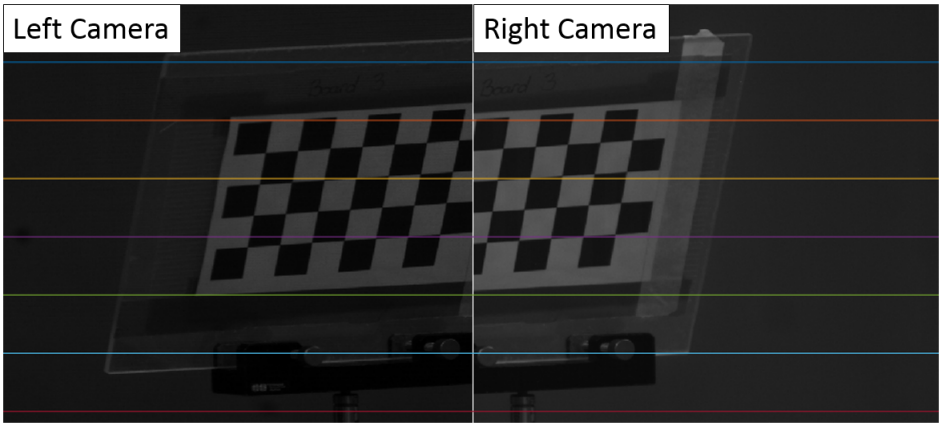

Figure 3.8: Horizontal lines are projected onto the rectified image to verify that common points between the image pair intersect the line at the same point.

3.2.2 Triangulation process

Common points between a stereo image pair are manually selected to triangulate the identified points in real world coordinates using the stereo camera calibration parameters as shown in Figure 1.9. A stereo image pair of a calibration checkerboard shown in Figure 3.9. These images are used to demonstrate the triangulation reconstruction process. The reprojection error from the stereo calibration used in this example is 0.13 pixels.

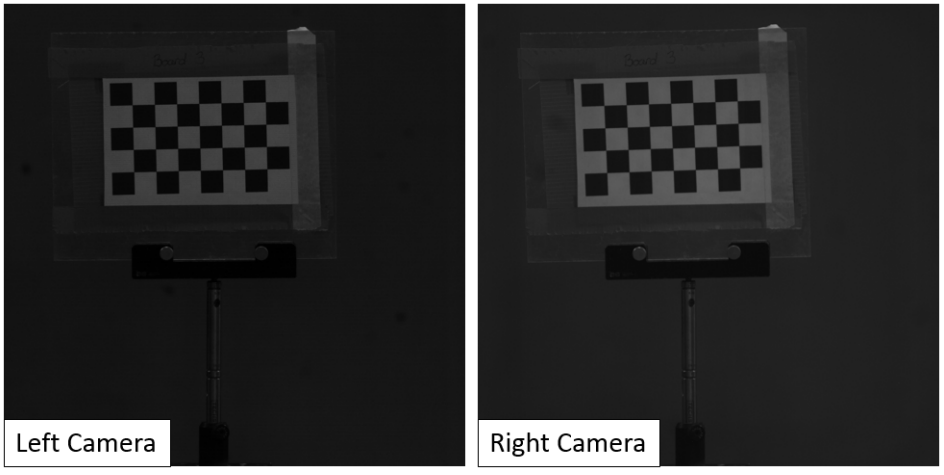

Figure 3.9: The pair of checkerboard images used to demonstrate the triangulation reconstruction process.

The *ginput* command is used to manually select and extract the images' x-y coordinates as identified by the red dots on the checkerboard in Figure 3.10a.

The triangulation function uses the x-y coordinates and stereo calibration parameters to transform the points into x-y-z coordinates.

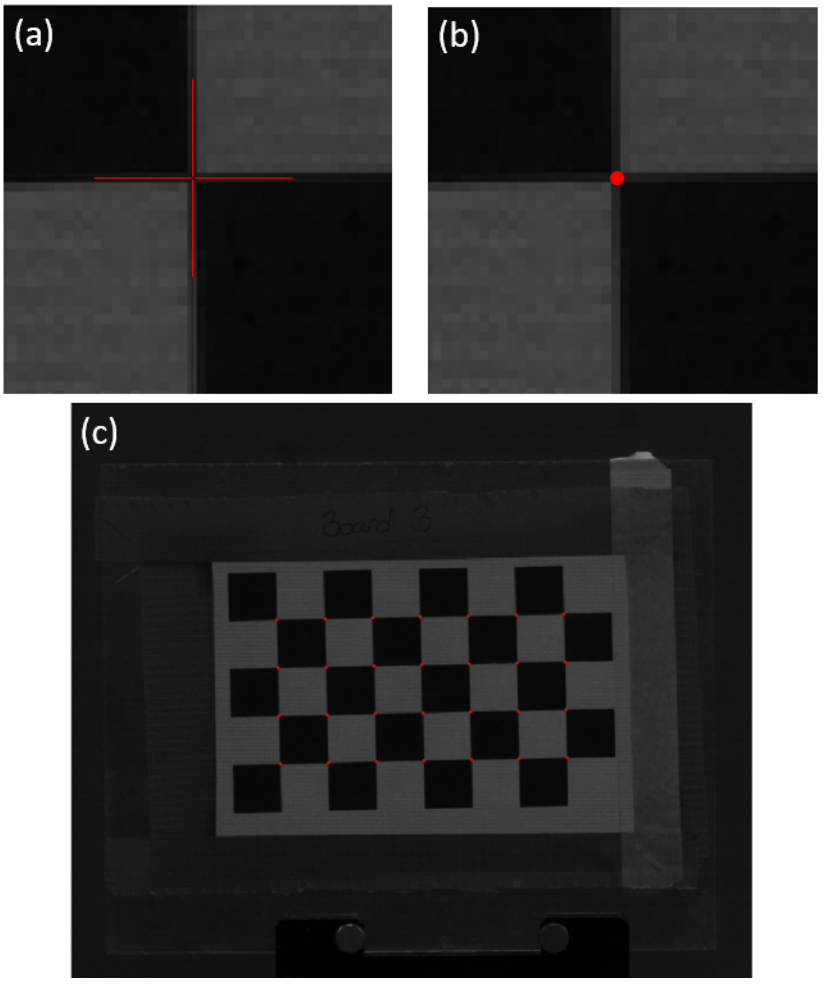

Figure 3.10: (a) The *ginput* command provides cross hairs (b) to accurately select the desired point. (c)The complete array of selected points. The cross hairs in (a) were colored and the point in (b) was enlarged for easier visualization.

Figure 3.11 shows two views of the reconstructed points from the triangulation method against the automated checkerboard detection. The left image shows very little variation between the two methods in the x-y plane. The maximum displacement between the two methods in the x and y direction are 0.25 mm and 0.12 mm, respectively. The right image shows the depth variation in each method along the width of the board. The automated method's reprojected points are within $\pm$ 3 mm, but the triangulation method shows differences up to $\pm$ 6 mm.

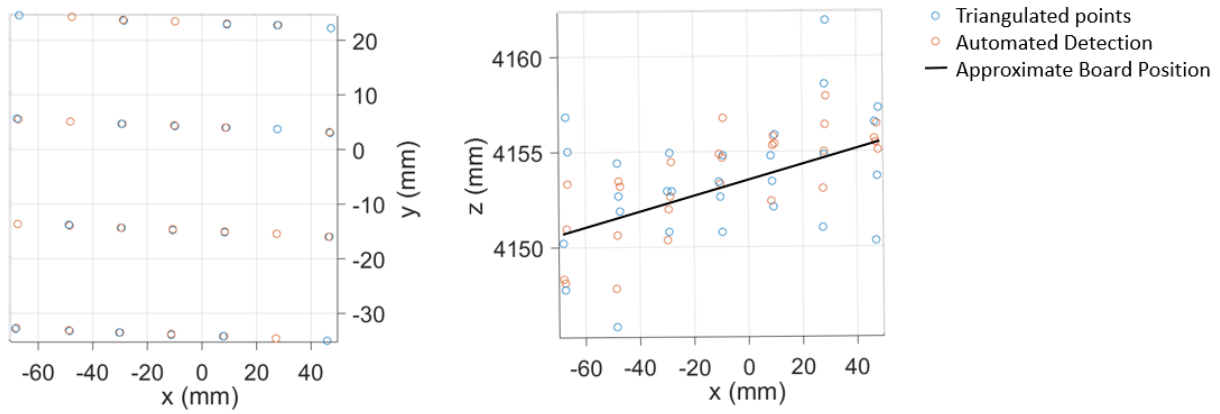

Figure 3.11: Two views of a comparison between the manual triangulation method and MATLAB's automated detection of checkerboard corners. The left image shows minimal difference in the x-y plane. The right image shows depth variation between the two methods.

The automated method's error is solely based on the reprojection error from the camera calibration. This can be used to quantify the uncertainty of manually selecting common points in the pair of stereo images. Figure 3.11 shows that a reprojection error of 0.13 pixels corresponds to a depth variation of $\pm$ 3 mm. Because the angle between the pair of cameras is fixed by the stereo calibration parameters, there is a linear relationship between the pixel error and reported depth. The $\pm$ 6 mm variation shown for the triangulation method in Figure 3.11 is used to determine that the triangulated points were selected within 0.26 pixels of each other.

3.2.3 Reprojection process

A reconstruction of a calibration checkerboard is used to demonstrate the process used to reproject the experimental images. Once the calibration is complete, the image pair is rectified to determine the appropriate disparity range. In this example, the checkerboard's disparity is between 494 and 507 pixels as shown in Figure 3.12.

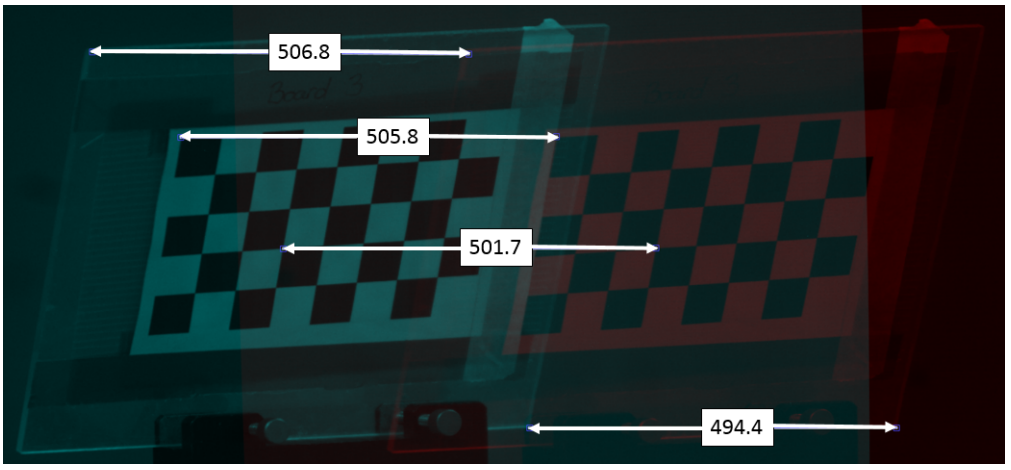

Figure 3.12: The disparity range of the checkerboard is between 494 and 507 pixels. This is much larger than the ideal range of 0 to 256 pixels, but was the smallest disparity that could be achieved in this study.

Once the images have been rectified and the disparity range selected, the image can be reprojected using the *disparity* and *reconstructScene* functions. Figure 3.13a shows the reconstructed 3-D point cloud with the color bar indicating distance from the camera. The axes of Figure 3.13a can be cropped to reduce noise and emphasize the location of interest shown in Figure 3.13b.

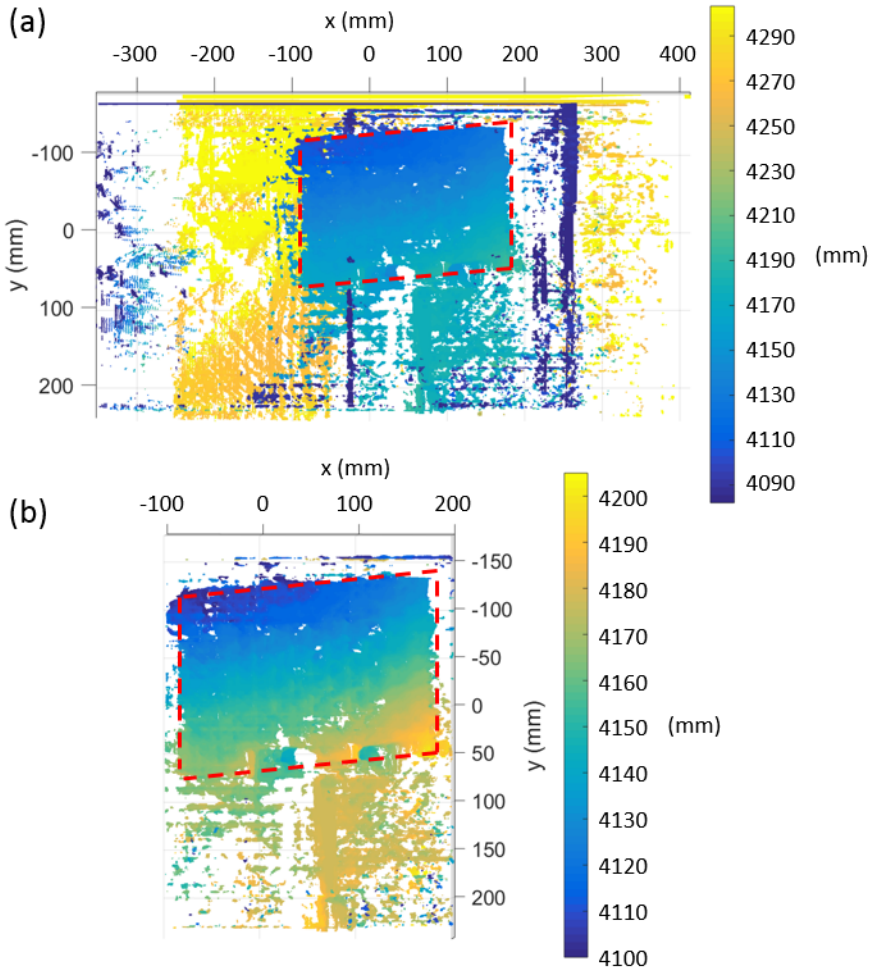

Figure 3.13: (a) Raw reconstructed point cloud of the checkerboard and (b) cropped reconstructed point cloud.

By increasing the block size of the matching algorithm, noise can be further reduced. The default block size in MATLAB is 15 pixels, which was used to construct Figures 3.13a and b. Figure 3.14 is the product of increasing the block size to 23 pixels. Although the noise is reduced, a consequence of increasing the block size is that details of the image are lost and larger regions are not properly reconstructed as shown by the excessive blank regions in Figure 3.14. The red outline in each reprojection identifies the actual location of the board.

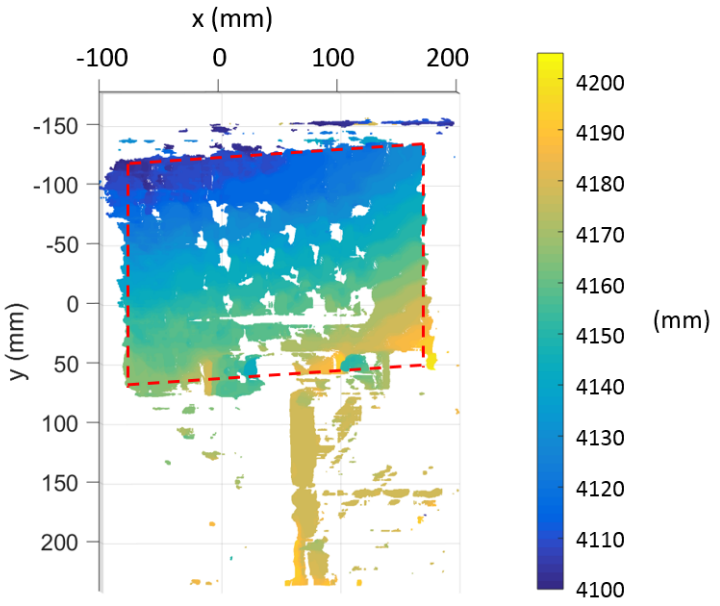

Figure 3.14: Reprojection of the checkerboard with a block size of 23 pixels results in reduced noise and larger empty regions.

3.2.4 Effect of stereo camera angle on 3-D reconstruction

To investigate how angle variation between each camera in a stereo system affects three-dimensional reconstruction, an analysis was performed to reproject an object of known dimensions. Here a box of matches was chosen as the object because it is a simple object with known dimensions that can be used to quickly quantify reprojection errors. The box of matches, shown in Figure 3.15, has several unique features, including words and pictures. These features allow MATLAB to easily match common points between the pair of stereo images. A Photron SA-X2 and Photron Mini UX were set up at varying angles, similar to the schematic in Figure 3.16. The cameras were calibrated using a 5x8 checkerboard with 19.05mm squares. The camera angles explored were between 2 and 14 degrees with 3 degree intervals.

Figure 3.15: A box of matches was chosen as the object to reproject because of its known dimensions and unique features that can be used to correlate matching regions in the left and right camera.

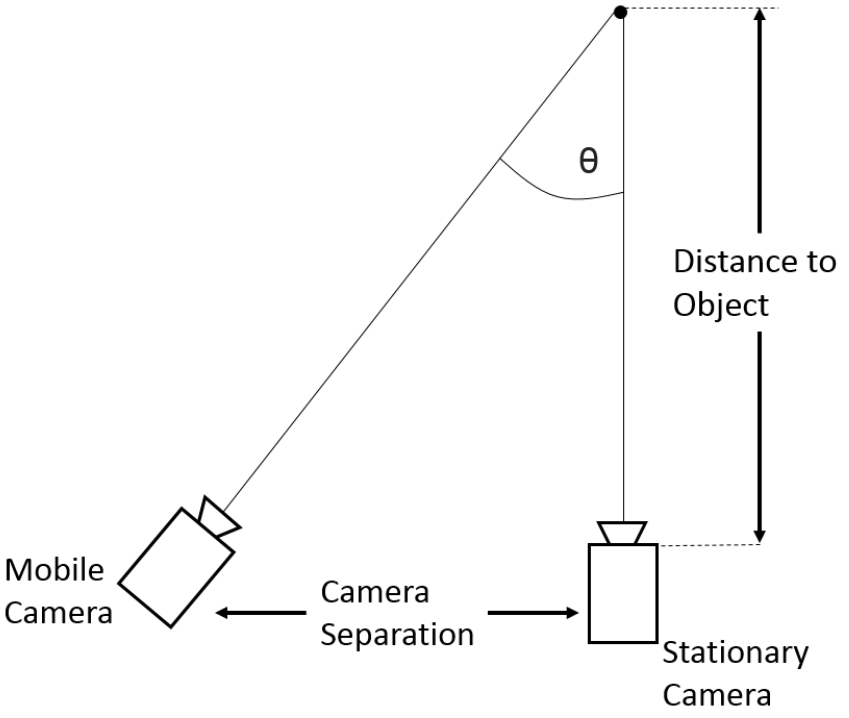

Figure 3.16: Schematic of the setup used to characterize reconstruction quality at stereo camera angles between 2 and 14 degrees.

Figure 3.17 shows the original images from the left camera, right camera

and reprojection using the MATLAB routine previously described for (a) a 2 degree camera angle, (b) 5 degree camera angle, (c) 8 degree camera angle, (d) 11 degree camera angle and (e) 14 degree camera angle. A fixed block size of 15 pixels was used for each reconstruction. Other block sizes were tested, and while smaller block sizes filled in some of the gaps, it had no affect on the dimensions of the reprojection. The height, width and depth of each reconstructed box was measured, as indicated by the markings on the reconstructed image. These values were tabulated and compared to the physical measurements in Table 3.1.

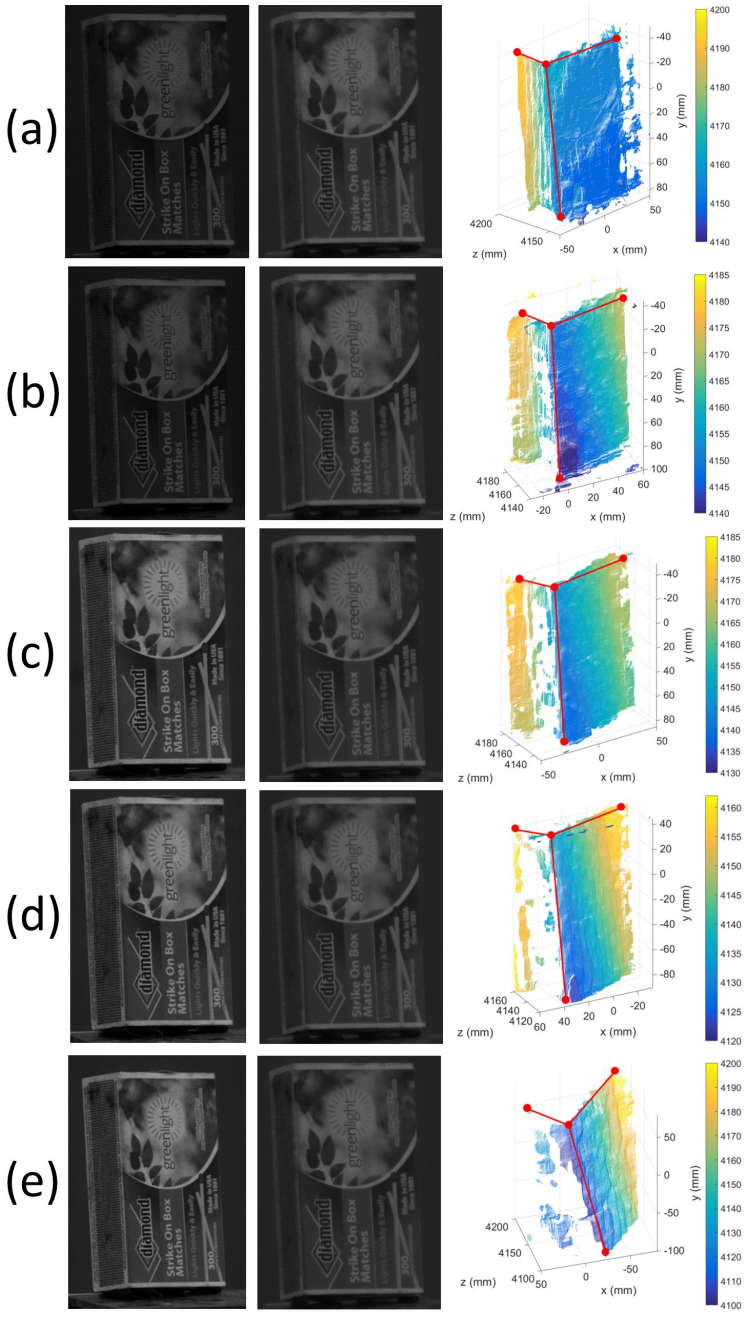

Figure 3.17: Images from the left and right camera used to create the reprojection at camera angles of (a) 2 degrees, (b) 5 degrees, (c) 8 degrees, (d) 11 degrees and (e) 14 degrees

Table 3.1: A comparison between the reconstructed box dimensions as the stereo camera angle is varied.

Scenario	Height (mm)	Width (mm)	Depth (mm)	Disparity (range)
Actual size	119.8	68.4	36.2	
2 degree angle	119.6	72.7	29.3	485-517
5 degree angle	122.2	72.7	29.9	935-967
8 degree angle	122.0	76.3	29.3	1510-1542
11 degree angle	130.0	75.2	29.7	2086-2118
14 degree angle	180.0	114.8	47.5	2680-2712

The height, width and depth measurements for camera angles between 2 and 11 degrees are all within 10mm of the true value. The height and width measurements for the 14 degree separation differed by 60mm and 46mm from the true value. However, the depth measurement, although 11mm larger than the true value, compared relatively well with the other scenarios that reported values 7mm too short.

CHAPTER 4

HELIUM JET ANALYSIS

A two and three-dimensional study of a helium jet was performed to obtain initial validation of tracking turbulent gases using schlieren and shadowgraph techniques. To determine the accuracy of the schlieren and shadowgraph tracking methods, they were compared to a two-dimensional particle image velocimetry (PIV) analysis.

4.1 Two-dimensional analysis

Figure 4.1 shows a single frame of PIV and the ensemble-average velocity obtained from 5000 frames. It is expected that the average velocity near the nozzle would be the highest, but because of the dense seeding near the nozzle exit, the PIV software was not able to accurately resolve individual particles and detect movement, creating a lower velocity zone.

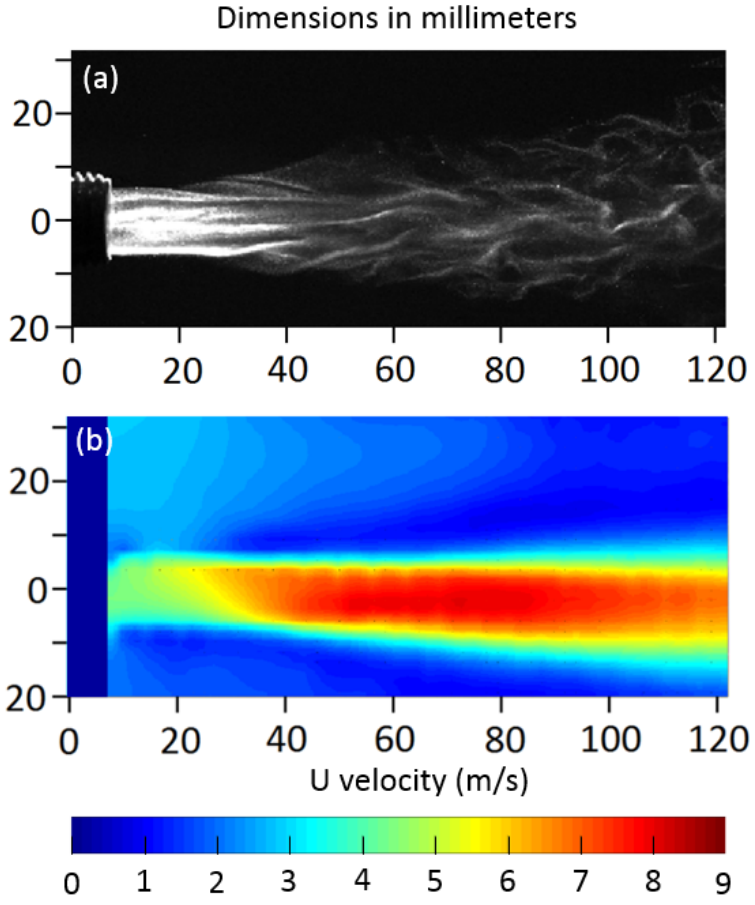

Figure 4.1: (a) A single frame of PIV shows the dense particle region near the nozzle exit that (b) results in a lower average velocity at the nozzle.

The particle Stokes number was calculated to determine how well particles follow the flow path. Stokes number is a dimensionless number used to quantify how accurately the particles in PIV follow flow gradients and resolve velocity fluctuations. Stokes number is determined from: Equations 4.1 and 4.2. Where u_0 is the flow velocity, l_0 is a characteristic length (usually the particle diameter), t_0 is the particle response time, ρ_p is the particle density, d_p is the particle diameter and μ_f is the fluid's dynamic viscosity. In order to accurately capture turbulent fluctuations and other sudden changes in a fluid flow, the Stokes number must be less than 1. If a Stokes number is greater than 1, then there will be a delay in the particle's response making the fluid's sudden changes untraceable. The parameters of this test resulted in a Stokes number of 650, but because the goal of this work was only to capture the mean velocity flow field so this was considered acceptable.

$$Stk = t_0 \frac{u_0}{l_0} \tag{4.1}$$

$$t_0 = \frac{\rho_p d_p^2}{18\mu_f} \tag{4.2}$$

When analyzing the SIV images, the movement of turbulent structures was on the order of a single pixel between frames. This resulted in lower than expected velocities because the software was unable to detect the small motions. To increase the softwares detection of motion, every fourth frame was analyzed reducing the average from 5000 frames to 1250 frames. Figure 4.2 shows the average velocity obtained for each SIV scenario.

Flow near the nozzle reports a velocity close to zero because SIV cannot be used to analyze the laminar region because there are no structures present to correlate. The velocities observed in SIV are also significantly lower than those in the PIV analysis. This is due to the optical path integration of schlieren imaging. In order to make a direct comparison between SIV and PIV, an Abel transform is implemented at 75mm.

An Abel transform can be used in spherical and axisymmetric flow fields to create path averaged data from axisymmetric planar data. The planar velocity data, V_{pl}, is transformed to path averaged data, V_{pa}, using: Equation 4.3 [29]. Where i is the radial position of the velocity with i_0 being the center of the flow and i_{edge} the edge of the flow, j is the axial position of the velocity, and N is the number of discrete velocity measurements between the center and edge of the flow. Alternatively work has been done to reverse the Abel transform to translate path averaged data into planar data [10, 32, 54]. Figure 4.3 shows the results of performing an Abel transform on the PIV data compared to the SIV data.

$$V_{pa}(i,j) = \frac{\sum_{i=i_0}^{i_{edge}} V_{pl}(i,j)}{N_{i_0 \to i_{edge}}} \tag{4.3}$$

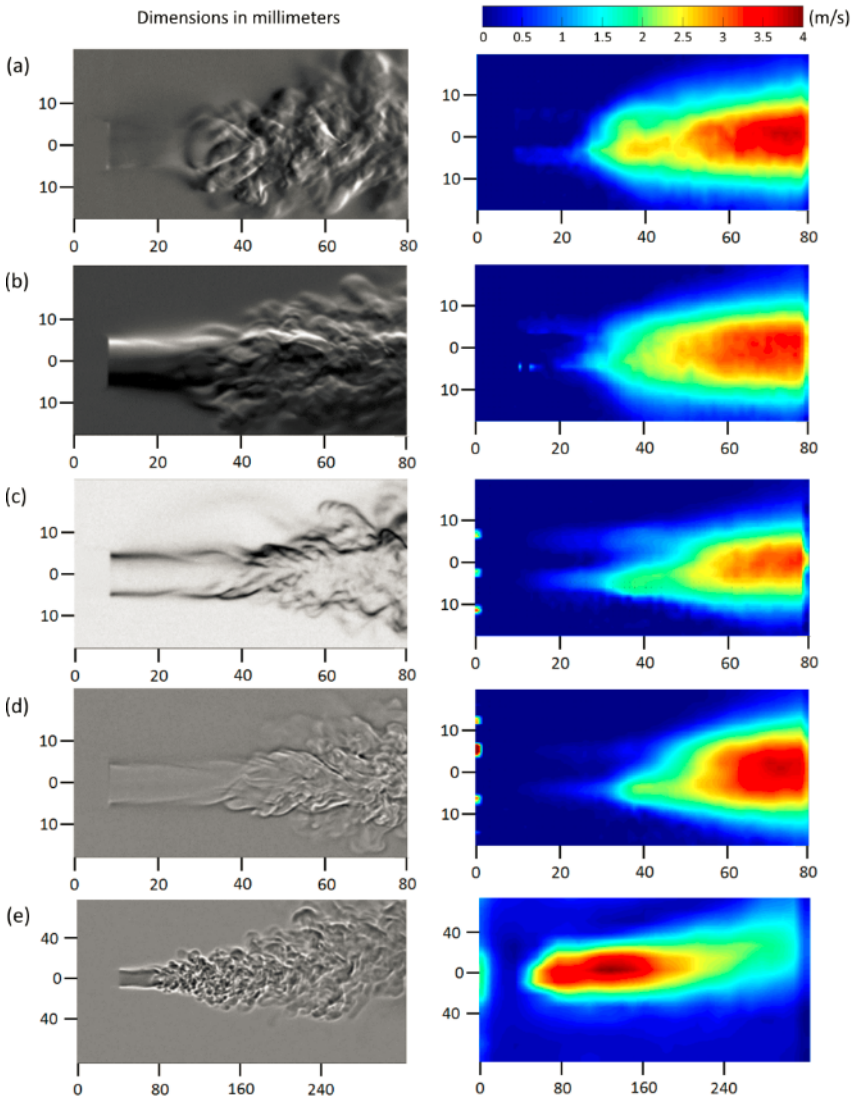

Figure 4.2: Average velocity of the helium jet for the (a) vertical cutoff, (b) horizontal cutoff, (c) circular cutoff, (d) focused shadowgraph and (e) projective shadowgraph.

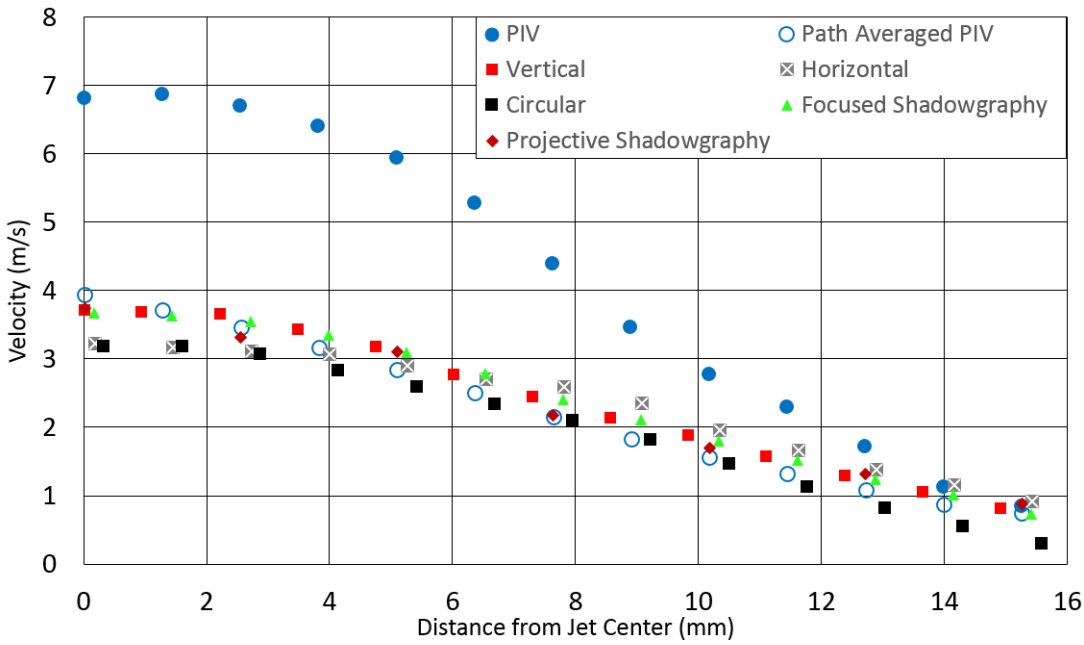

Figure 4.3: Helium jet velocity comparison between SIV, PIV and transformed PIV data at 75mm.

The data shows that the vertical cutoff, focused shadowgraphy and projective shadowgraphy compare well with the transformed PIV data, while the horizontal cutoff and circular cutoff deviate farther from the transformed PIV data. The average and standard deviation of the difference between each SIV analysis and the path averaged PIV from Figure 4.3 was calculated and is displayed in Table 4.1 to quantify the velocity error for each scenario.

Table 4.1: The average and standard deviation of the difference between each SIV case and the path averaged PIV is shown.

	Vertical	Horizontal	Circular	Focused Shadowgraphy	Projective Shadowgraphy
Average Velocity Difference (m/s)	0.173	0.085	- 0.307	0.109	0.061
Standard Deviation (m/s)	0.167	0.375	0.201	0.178	0.180

Previous work has determined that the accuracy of SIV is directly corre-

lated to the ”particle” size [10, 29]. Jonassen et al. identified that the optimum range of particle diameter for SIV is between 6 and 12 pixels [29], which corresponds to areas between 28 and 113 pixels. The histograms in Figure 4.4 show the number of occurrences for turbulent structure sizes with areas between 30 and 120 pixels for each cutoff variation. The structure sizes were determined by a MATLAB routine that used a dual threshold to isolate the light and dark turbulent structures. The projective shadowgraph images had a larger field of view and were cropped to the same physical dimensions as the rest of the tests. The histogram data was obtained from 500 equally spaced frames in 5000 test frames. The data from Figure 4.4 is in agreement with the results of Figure 4.3 and Table 4.1 in that the systems with more turbulent structures matched the transformed PIV velocity better. Figure 4.5 shows a comparison of the MATLAB routine used to calculate structure sizes between the focused shadowgraph and horizontal cutoff schlieren imaging, which showed the most and least number of structures in the desired size range, respectively.

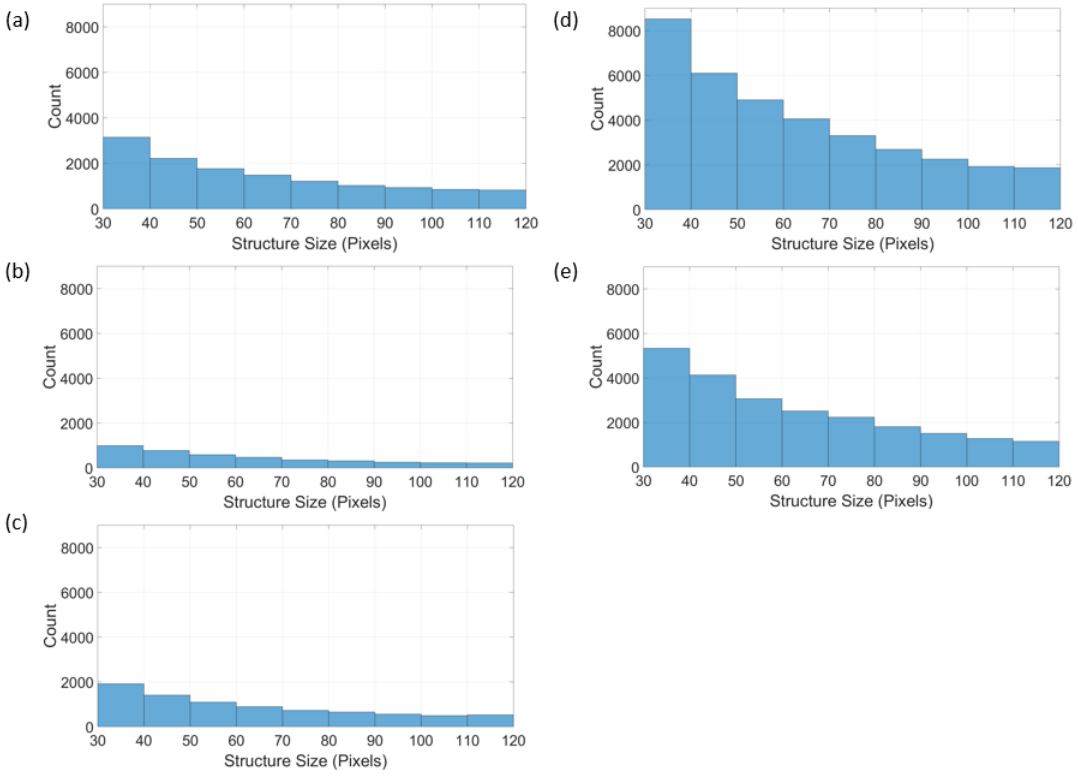

Figure 4.4: Histograms counting the number of occurrences that a turbulent structure size is seen in (a) vertical cutoff, (b) horizontal cutoff, (c) circular cutoff, (d) focused shadowgraph and (e) projective shadowgraph.

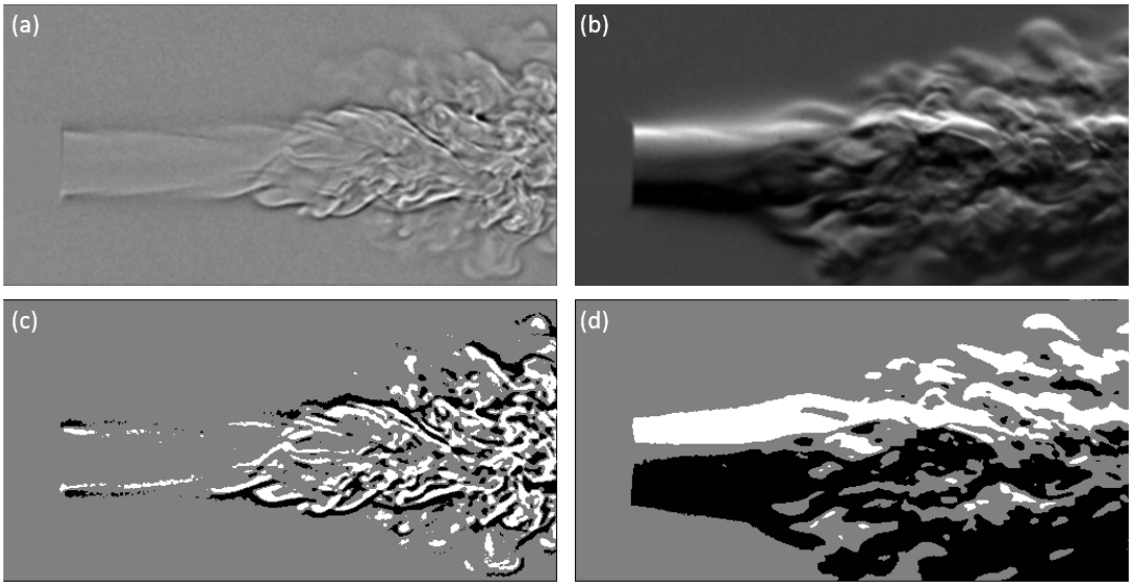

Figure 4.5: A MATLAB routine is used to isolate the light and dark regions of the (a) focused shadowgram and (b) horizontal schlieren cutoff. The processed images (c) and (d) show the output for processing (a) and (b), respectively. These represent the scenarios with the most (focused shadowgram) and least (horizontal schlieren cutoff) number of turbulent structures in the desired size range.

The axial location of 75mm was chosen because of the laminar core's affect on SIV. Figure 4.6 shows the velocity along the jet's radius at 60mm. Regardless of cutoff variation, the centerline velocity is not the maximum velocity. The light rays passing through the center of the jet are refracted less from passing through the laminar core than the light rays that pass through the edge of the laminar region resulting in higher velocity zones [29]. This effect is decreased as the distance from the nozzle increases.

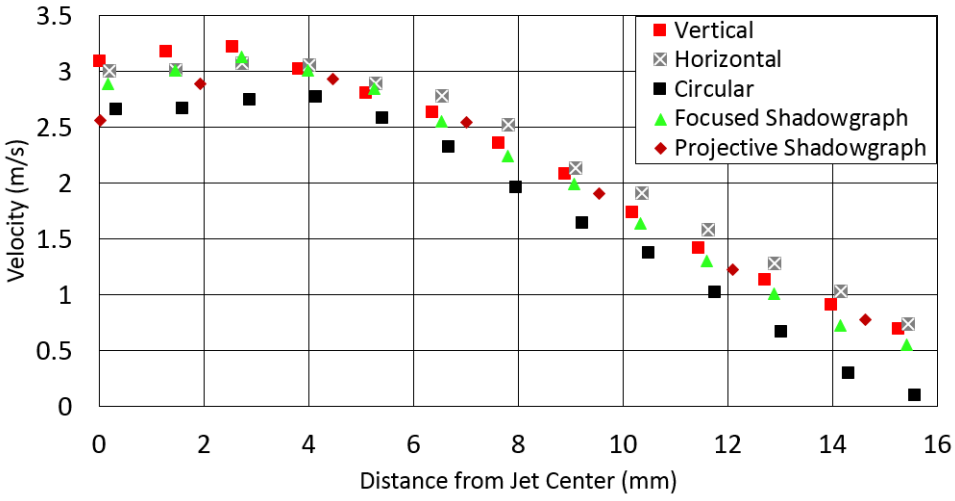

Figure 4.6: Helium jet velocity for different cutoff variations at 60mm. Due to the laminar core, the maximum velocity does not appear along the center of the jet.

4.2 Three-dimensional Analysis

4.2.1 Stereo schlieren

In order to calibrate the cameras in a stereo schlieren setup, the LED light sources were turned off, the cutoff tools were removed and the cameras' exposure were increased to 1000 μs. An example pair of calibration images are shown in Figure 4.7. Even with the high exposure levels, the calibration images are darker than an ideal image. This is because the housing for the negative meniscus lens, required to focus at the desired location, is blocking a significant amount of the light from entering the camera.

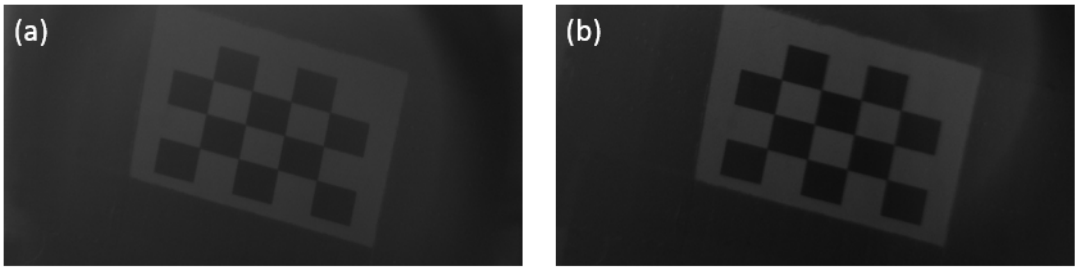

Figure 4.7: An example pair of calibration images from the stereo schlieren setup from the (a) left and (b) right cameras.

Figure 4.8 shows the extrinsic reconstruction and reprojection errors from the stereo schlieren calibration. From the extrinsic view, there is a camera angle

of approximately 3 degrees, and the cameras are vertically offset by 75 mm. Although this is not true to the physical setup of a 2 degree variation and vertically parallel cameras, the calibration was successful with a mean pixel error of 0.27 pixels. Camera 2 is located in the negative z-direction because there was a slight zoom difference between the cameras. MATLAB manipulates the coordinate reference so that the calibration boards are directly in front of camera 1 (blue), rather than the true location.

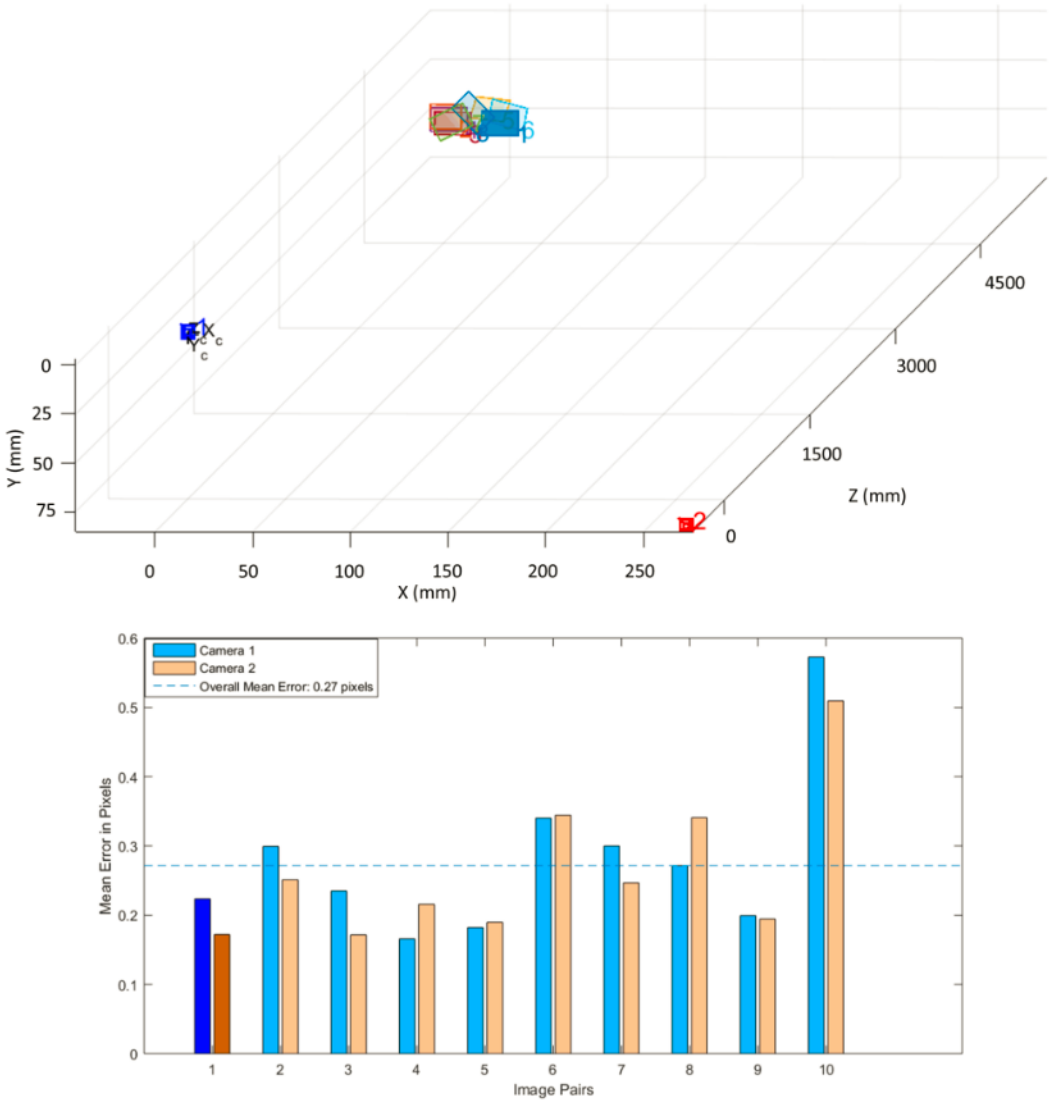

Figure 4.8: The (top) extrinsic reconstruction and (bottom) reprojection errors are shown. The extrinsic reconstruction closely represents the physical setup and average reprojection error obtained was 0.27 pixels.

An initial attempt was made to use the automated reprojection MATLAB

routine, but when determining the disparity range between the rectified images, all distances between common points were the same. This indicates that there is no depth variation in the images. Figure 4.9 shows the measured disparity between several common points for the vertical cutoff test. This was not a unique situation as all of the stereo schlieren scenarios exhibited a lack of depth.

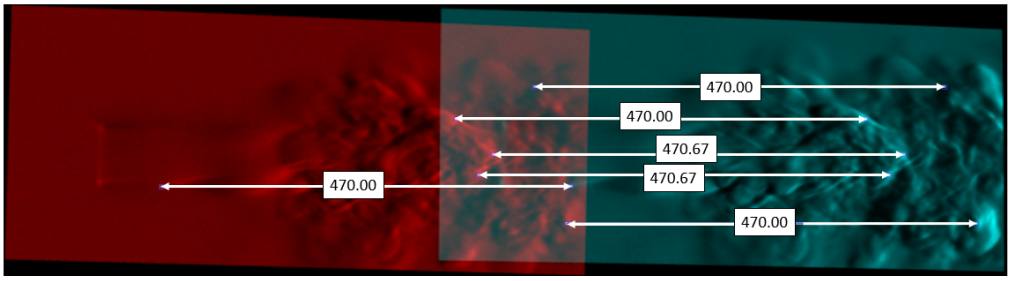

Figure 4.9: Several disparities were measured between common points on the stereo schlieren image pair, all of which resulted in approximately the same value indicating there is no depth to the image.

In order to attempt a three-dimensional reconstruction, a turbulent structure was identified in two pairs of stereo images 20 frames (0.5ms) apart. Using the triangulation reconstruction method the structure was reprojected using 15 points to approximate the structure. The images used and the reprojection are shown in Figures 4.10 and 4.11. Points vary in the z-direction by $\pm$ 7mm, which is due to the reprojection errors from the calibration and accuracy of manually selecting points.

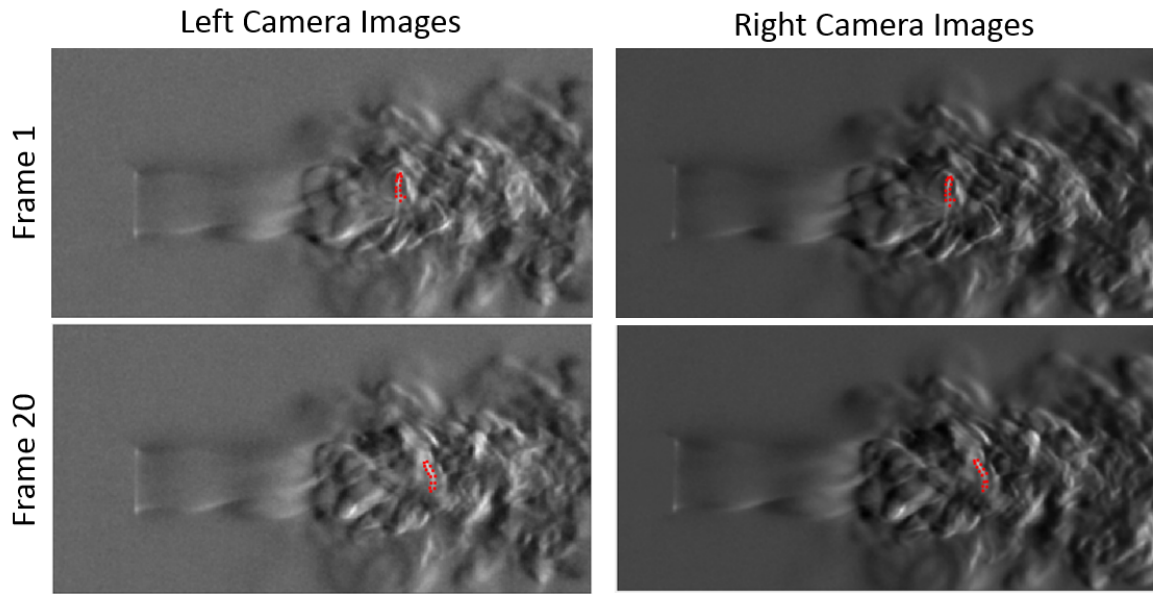

Figure 4.10: The stereo images from each camera 20 frames (0.5ms) apart are shown with the turbulent structure outlined in red from the *ginput* command in MATLAB.

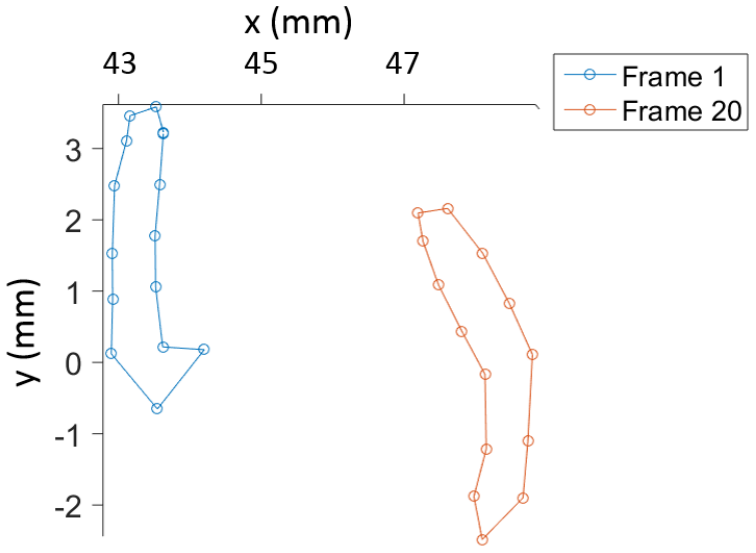

Figure 4.11: A reconstruction using the triangulation method of the turbulent structure from each frame shows a displacement of approximately 4.8mm, resulting in an average velocity of 9.5 m/s.

The resulting velocity magnitude of the structure is approximately 9.5 m/s. This was determined by calculating the displacement of the centroid for

each structure. To accurately determine the structure's centroid position, the *regoinprops* function was used. The averaged PIV data in the same axial and radial location yielded a velocity magnitude of 8.4 m/s. Because the structure is being tracked in three-space, correcting for path averaging is not necessary and a direct comparison can be made to PIV. The measured velocity is thus within expected uncertainties. Although tracking the turbulent structure in the stereo schlieren imaging was successful, it does not provide information beyond standard SIV as varying depths cannot be extracted from a pair of stereo images in a schlieren system. This manual processing is also not amenable to measuring average velocities throughout the jet across hundreds of images.

4.2.2 Stereo projective shadowgraph

Although the rod mirrors were left in front of the camera lens during calibration of the projective shadowgraph systems, they did not block as much light as the negative meniscus lenses in the stereo schlieren calibration. The light source for each camera was turned off, and the exposure levels were set to 1000 μs. A pair of calibration images is shown in Figure 4.12.

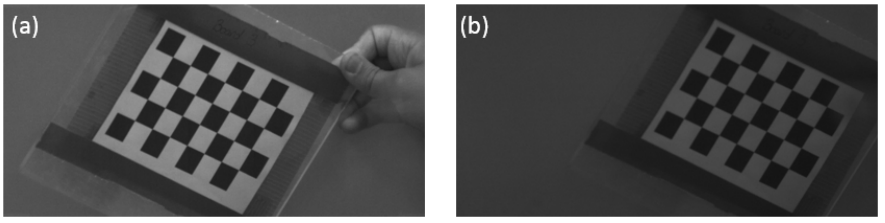

Figure 4.12: An example pair of calibration images from the (a) left and (b) right camera in the stereo projective shadowgraph system.

Shown in Figure 4.13 are the camera extrinsic reconstruction and reprojection error chart. The camera extrinsic view nearly matches the physical setup perfectly. The cameras were placed 150mm apart, and the cameras were focused on the retroreflective screen approximately 6.3 meters away (15 percent farther than the helium jet that was placed at 5.5 meters). The overall mean reprojection error is 0.13 pixels, which is less than the recommended 0.5 pixel, and there are no outliers.

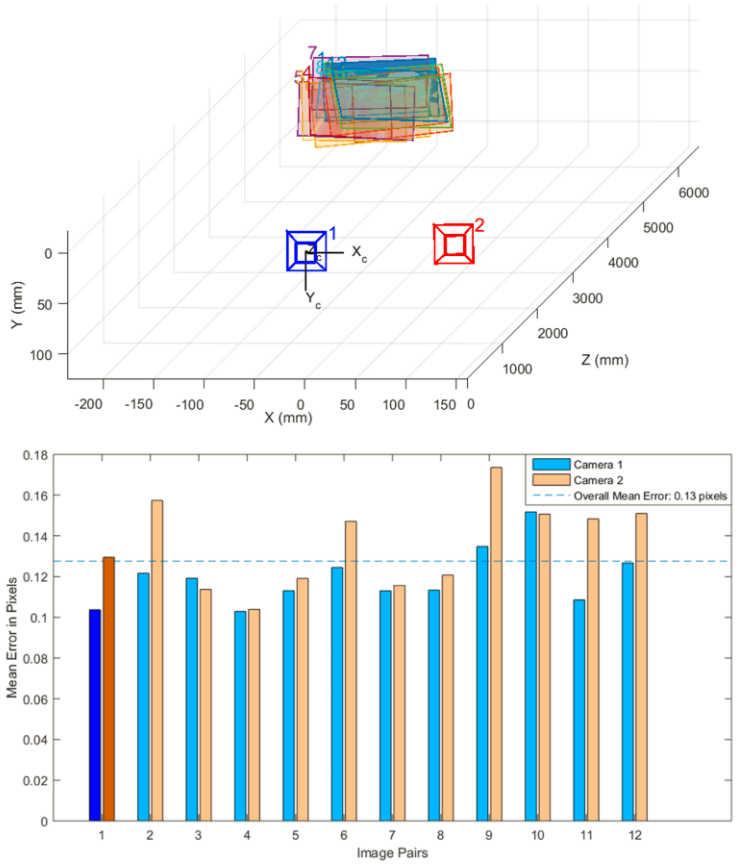

Figure 4.13: The (top) extrinsic view matches the physical setup very well, and an (bottom) average reprojection error of 0.13 pixels also indicates a successful calibration.

To verify that depth variation existed in projective shadowgraphy, multiple measurements were taken between common points in the rectified images using the automated MATLAB routine. Figure 4.14 shows that there is depth variation in the image because the disparity ranges from 540 to 570. Because there is varying depth within the image, the automated MATLAB routine can be used to reproject the image pair. Figure 4.15 shows the left and right camera views used to create the reprojection with the color bar indicating depth.

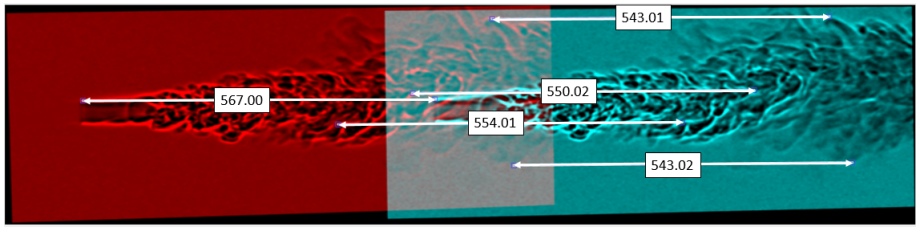

Figure 4.14: Different distances between common points along the helium jet in the rectified images signifies that there is depth variation in the image.

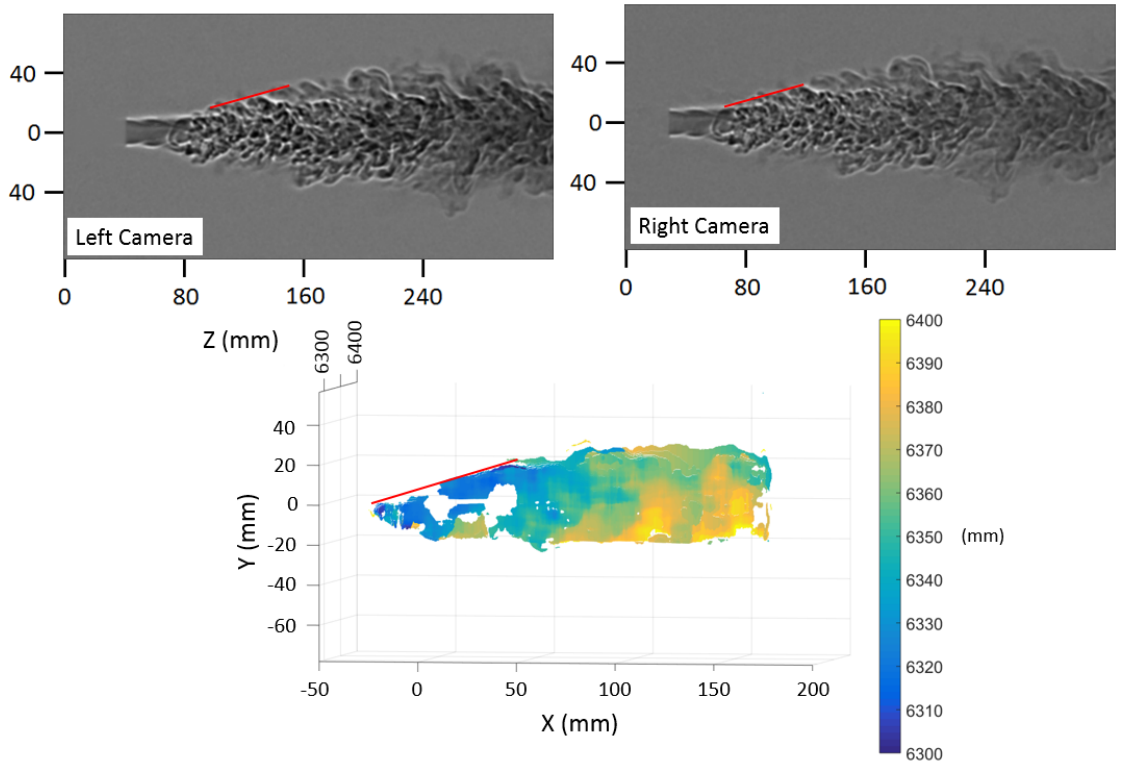

Figure 4.15: The processed left and right image used to create reprojection with a block size of 39 is shown. The red line was used to compare the divergence angle from the images to the reprojected divergence angle.

An initial check was performed by comparing the size of the reprojected jet to the size of the helium jet in the individual two-dimensional images. The reprojected helium jet is smaller than what is shown in the two-dimensional images. This is because only the region with turbulent structures having high contrast were reprojected by the automated routine. Turbulent features with weak contrasts, such as those on the outer radius of the jet or far from the nozzle, were not reprojected, likely due to poor matching between the images.

The divergence angle of the helium jet was compared between the reprojection and test images as indicated by the red line in Figure 4.15. Only the divergence angle along the top side of the jet was measured because the turbulent structures on the lower side of the jet had weaker contrasts and were not reprojected by the automated routine. The divergence angle of the reprojection was measured to be 17.1 degrees, which compares well against the 16.4 degree angle from the individual test images. A divergence angle of about 20 degrees is expected for flows less than Mach 0.3 [30].

The reprojection also increases in depth from the nozzle to the end of the jet (left to right). This trend implies that the outer surface of the jet is being reprojected rather than internal turbulent features. Figure 4.16 shows two reprojections of the helium jet 100 frames apart in order to identify movement within the

reprojections. Some motion can be observed, but without tracking the physical structures it is difficult to perform a quantitative analysis.

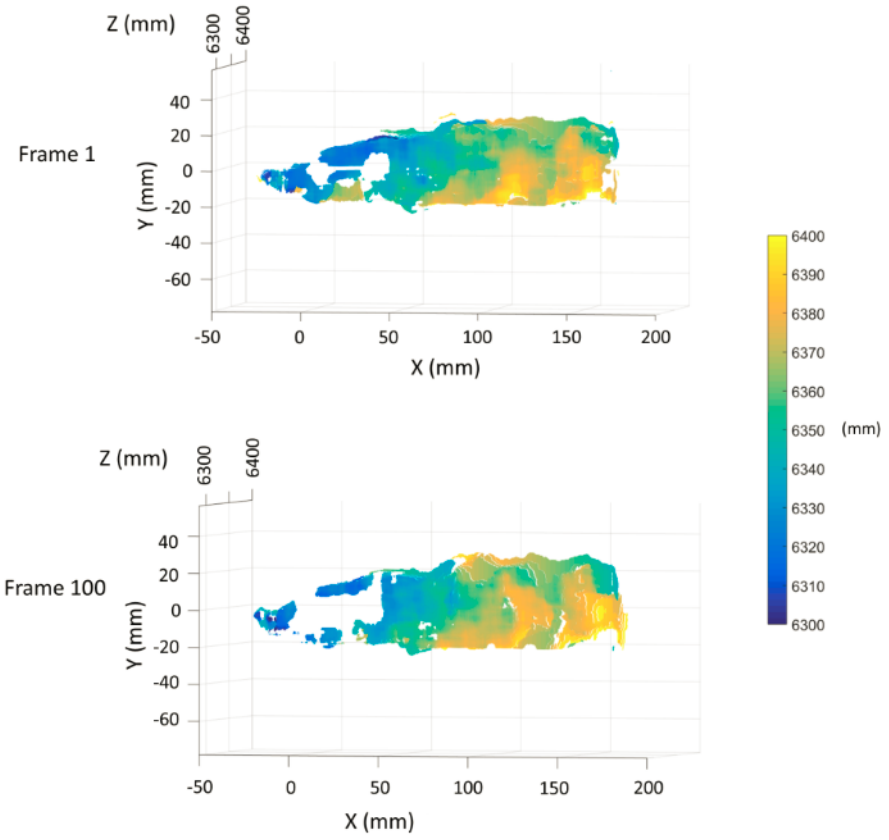

Figure 4.16: Two reprojections, separated by 100 frames (2.5ms), created with a block size of 39 are shown. Some motion can be observed between the reprojections, but it is difficult to quantify the movement without tracking a physical structure.

Although stereo projective shadowgraphy allows depth determination, additional work needs to be performed to investigate the details of what is being reprojected in order to obtain quantitative results. Though the details of the turbulence are not captured in the reprojection, the shape of the helium jet is identifiable. This method will likely have more success in tracking the expansion of gas fronts rather than internal mixing.

CHAPTER 5

EXPLOSIVE ANALYSIS

5.1 Explosive testing with stereo schlieren imaging

As observed in the stereo schlieren helium jet analysis, there was no depth determination in the explosive tests conducted in THOR, so there is no three-dimensional reconstruction to be made. Figure 5.1, however, shows three frames from the explosive test that exhibit interesting features regarding the identification of turbulent structures using stereo schlieren imaging. Frame 10 (0.25 ms after detonation) shows similar shock wave features in the left and right camera views; however, it is near impossible to match common turbulent features in the left and right camera. Frame 40 (1 ms after detonation) shows that several turbulent structures can be identified in both cameras. Examples of matching structures are outlined in blue, and an example of a structure that is not seen in both cameras is outlined in red. This trend of resolving more turbulent structures would be expected to increase with time as the gas front evolves, but as shown in frame 70 (1.75 ms after detonation), much of the viewing window has been clouded from the product gases and much of the sharp features that identify turbulent structures are lost.

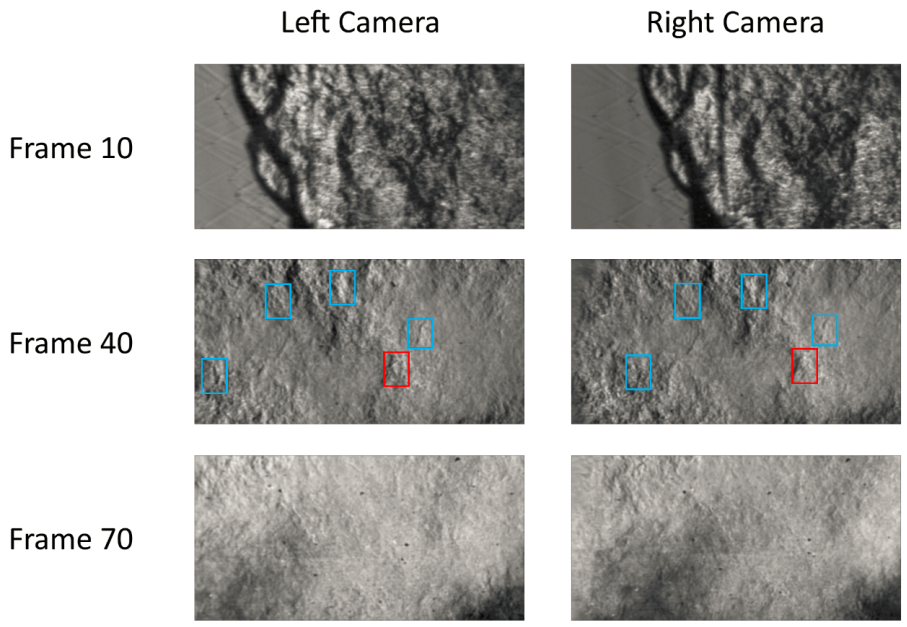

Figure 5.1: Left and right camera views of a stereo schlieren explosive test at three separate frames. Frame 10 shows that it is incredibly difficult to identify turbulent structures in the initial frames, by frame 40, most of the turbulence can be identified in both cameras. At frame 70, the viewing windows have been clouded making it difficult to continue identifying features.

Turbulence cannot be identified in the left and right camera during frame 10 due to motion blur. The shock wave and product gases were traveling too quickly for the cameras' exposure setting. Enough time has elapsed by frame 40 to reduce the motion blur effects and create sharp turbulent structures, but not all turbulent structures appear in both cameras. This is because the light in each schlieren system is refracting differently. Light interacts with inhomogeneous media, i.e. air and the explosive products, and refracts at a certain angle based on the refractive index of the schlieren object. The refractive index of a gas is a function of chemical species, temperature and density [47]. These refractive index changes in the explosive test are different in each camera view because of local changes in temperature and density. This was not an issue during the helium jet tests because the jet was a relatively simple flow field. Although the helium jet does not have perfectly uniform temperature and density throughout the flow, the changes observed at the small camera angle are negligible, but they become more significant at larger camera angles.

5.2 Field explosive testing using stereo projective shadowgraph

The calibration process for the explosive projective shadowgraph was the same as the helium jet. The light source was turned off, and the cameras' expo-

sure was increased to 1000 μs allowing natural light to illuminate the checkerboard. A pair of calibration images with the reprojection estimation are shown in Figure 5.2.

Figure 5.2: A pair of calibration images with MATLAB's automated checkerboard corner detection (green circle) and its estimated reprojection of the corner (red plus).

Shown in Figure 5.3 are the camera extrinsic reconstruction and reprojection error chart. The camera extrinsic view matches the physical setup well. The cameras were placed 1.5m apart, and the cameras were focused on the retroreflective screen 5.5m away. The mean reprojection error of the 15 calibration images is 0.29 pixels, indicating a successful calibration.

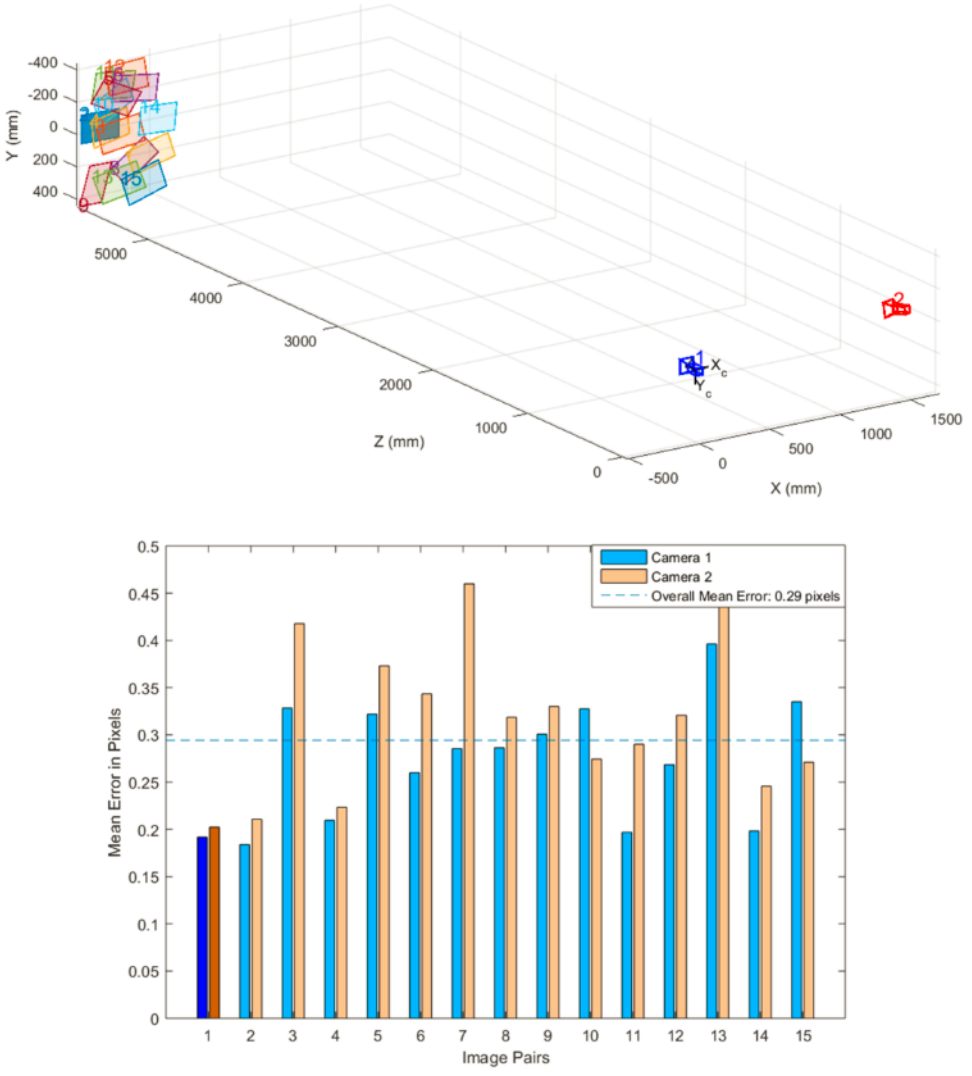

Figure 5.3: (Top) Extrinsic view matches the real world setup very well. The cameras were approximately 1.5 m apart, and the target was 5.5 m from the cameras. (Bottom) An average reprojection error of 0.27 pixels also indicates a successful calibration.

Figure 5.4 shows a left and right camera view of raw and processed test images. The Photron SA-Z cameras produced color images, which were converted to gray-scale in order to use MATLAB's *disparity* function and apply the image processing algorithm.

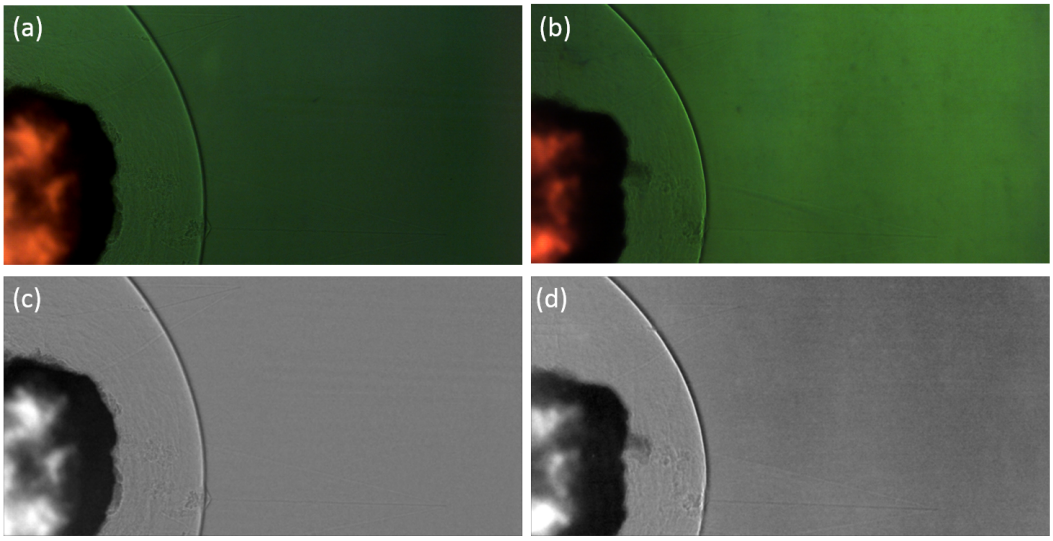

Figure 5.4: (a) Left and (b) right view of the raw test image and (c, d) respective processed images.

Unlike the helium jet, it is difficult to determine common points between each view due to the extended camera angle and opaque gas cloud. Figure 5.5 shows the rectified images and best guesses to common points between each view. Although the disparity range shown in Figure 5.5 is between 2244 and 2278, the range used to reconstruct the images was 2197 to 2325. This range was chosen to ensure that no part of the reconstruction was excluded as the exact disparity range could not be determined with accuracy.

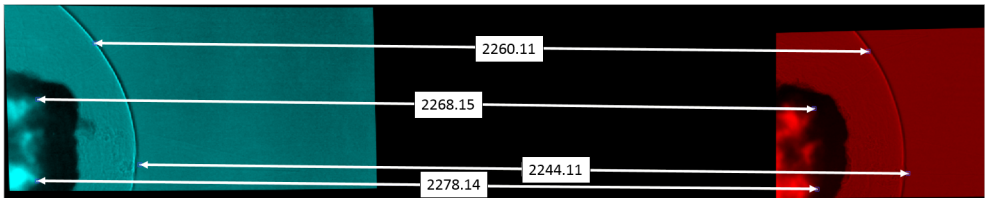

Figure 5.5: The rectified anaglyph of the explosive test shows a large disparity between the images, which is due to the large angle between the imaging systems.

The processed images from frames 35, 40 and 45 (0.875, 1 and 1.125 ms after detonation) used to create reprojections of the fireball and shock wave are shown in Figure 5.6. The reprojections of each frame are shown in Figure 5.7. Although the cameras are spaced 14 degrees apart, there is still strong agreement with the dimensions of the reprojection compared to the image.

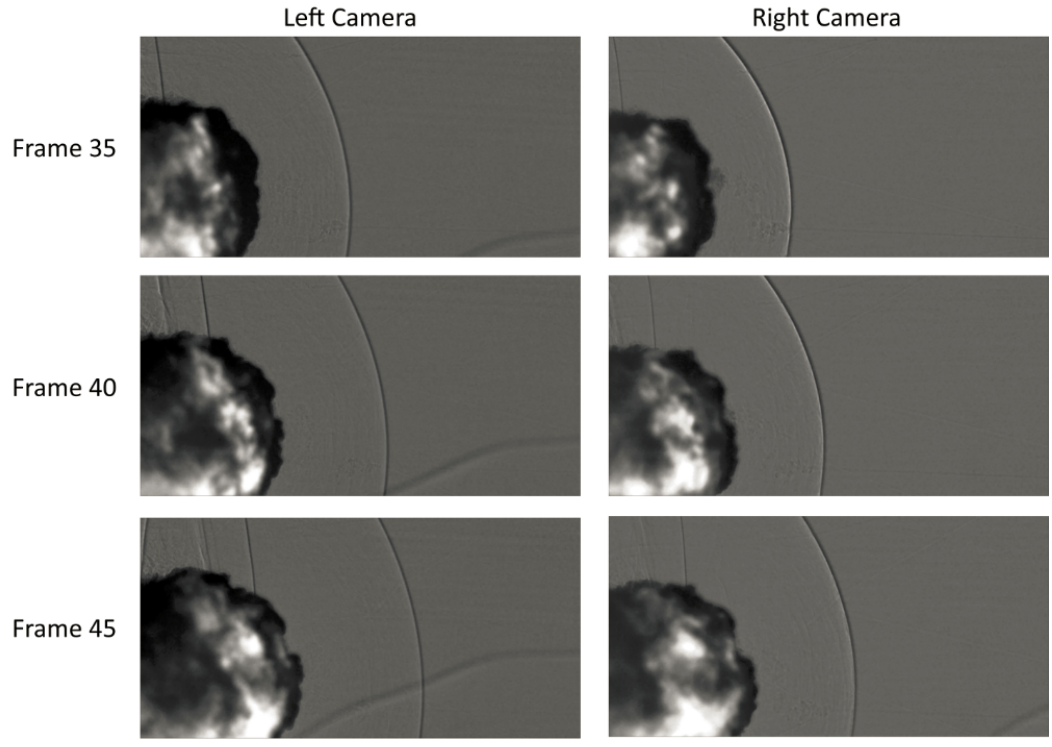

Figure 5.6: Processed images from frames 35, 40 and 45 from the left and right camera views used to create reprojections.

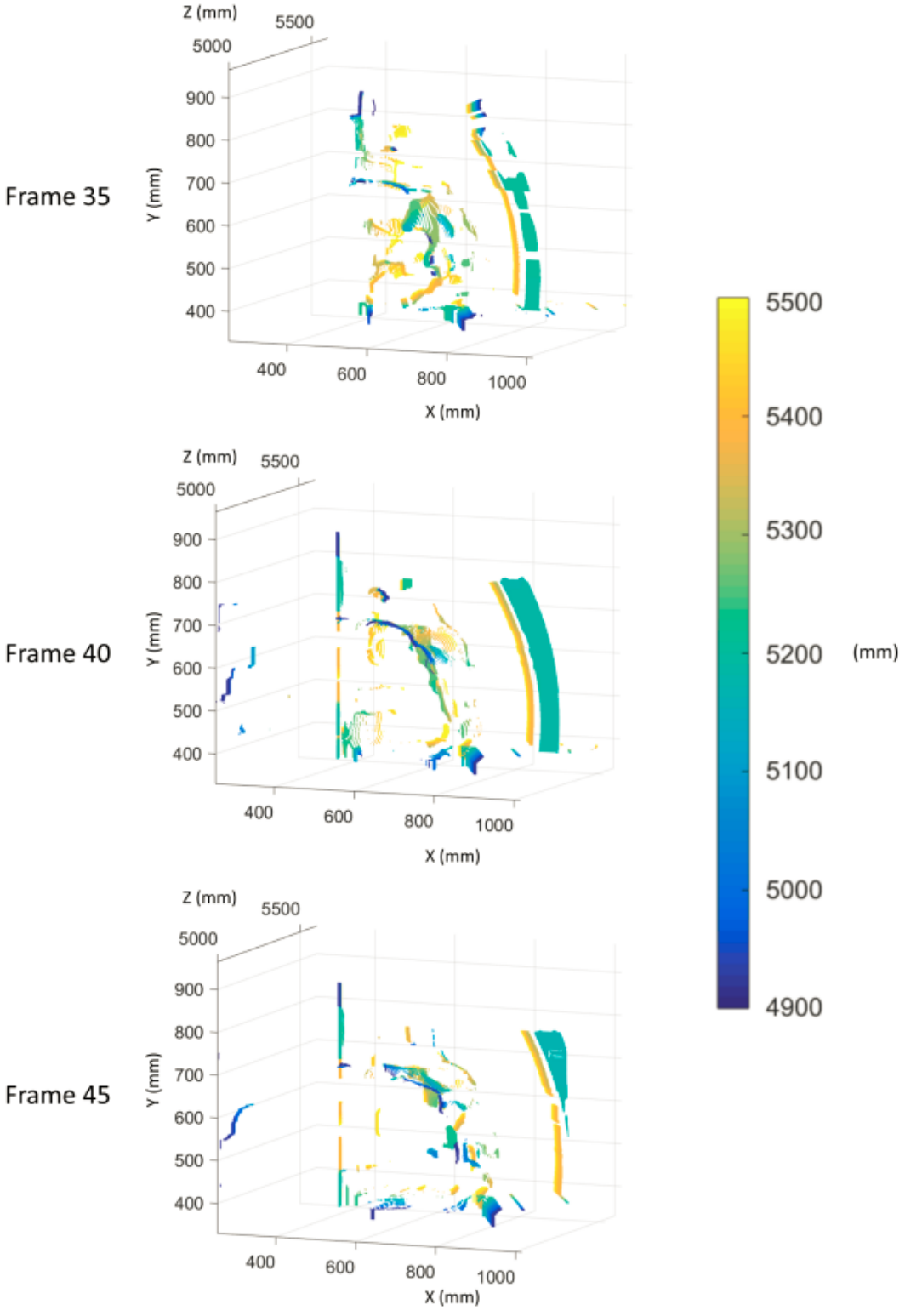

Figure 5.7: Reprojections of the fireball and shock wave for frames 35, 40 and 45 (0.785, 1 and 1.125ms after detonation)

The shock waves were isolated from each reporjection and replotted to reduce noise and obtain velocities. The new reprojection is shown in Figure 5.8. Three velocity measurements were taken between each reprojection at manually identified locations that could be matched, obtaining Mach numbers varying from 1.54 to 1.77 with an average of 1.67 and standard deviation of 0.07.

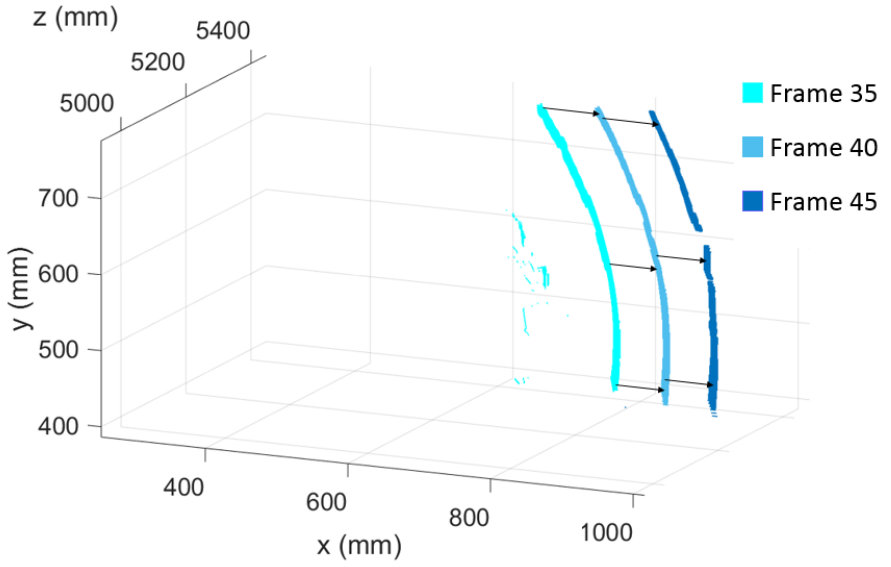

Figure 5.8: Reprojection of the shock propagation over 10 frames. Six displacements were measured obtaining average Mach numbers between 1.54 and 1.77 along the shock front.

The shock wave's displacement was measured from the left camera for frames 35, 40 and 45 for validation. The shock wave is only visualized where light rays are tangent to the shock wave, and in a projective shadowgraph system, the location of this intersection changes as the shock wave propagates due to the diverging light. In order to account for the changing intersection, a geometrical correction, discussed in [14, 22], was used to determine the true radius of the shock wave. The radii calculated were 0.972m, 1.034m and 1.094m for the respective frames, resulting in Mach numbers of 1.44 and 1.41.

The geometric correction was not performed for the three-dimensional analysis, and is the likely source of error. Because each camera is not viewing the same location of the shock wave, shown in Figure 5.9, this adds a complexity that has not yet been investigated, and was thus unaccounted for. Figure 5.9 is exaggerated to more clearly show the cameras viewing different intersections on the shock wave so the errors are smaller than shown. Developing a correction for a multi-camera system should be explored in future work.

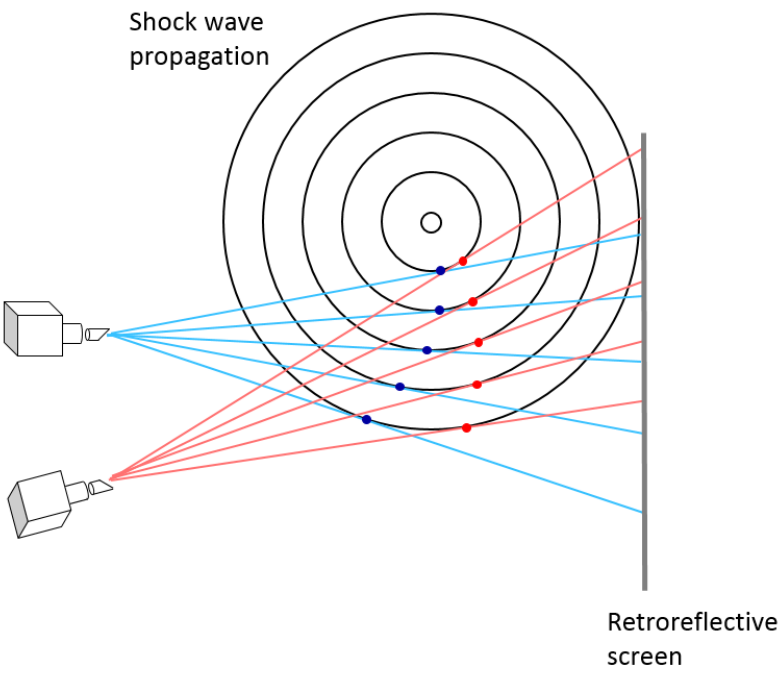

Figure 5.9: Stereo cameras in a projective shadowgraph system are not imaging the same location of the shock wave.

A similar analysis was performed on the fireball, shown in Figure 5.10. However plotting all three frames became convoluted so Figure 5.10 shows only frames 35 and 45. Five manually measured displacements were used to calculate velocities between 200 and 420 m/s for the product gas front. To show a more complete gaseous reconstruction, frames 181 and 196 (4.525 and 4.900 ms after detonation) were reprojected, and are shown in Figure 5.11. Nine displacements were measured yielding velocities between 40 m/s and 215 m/s.

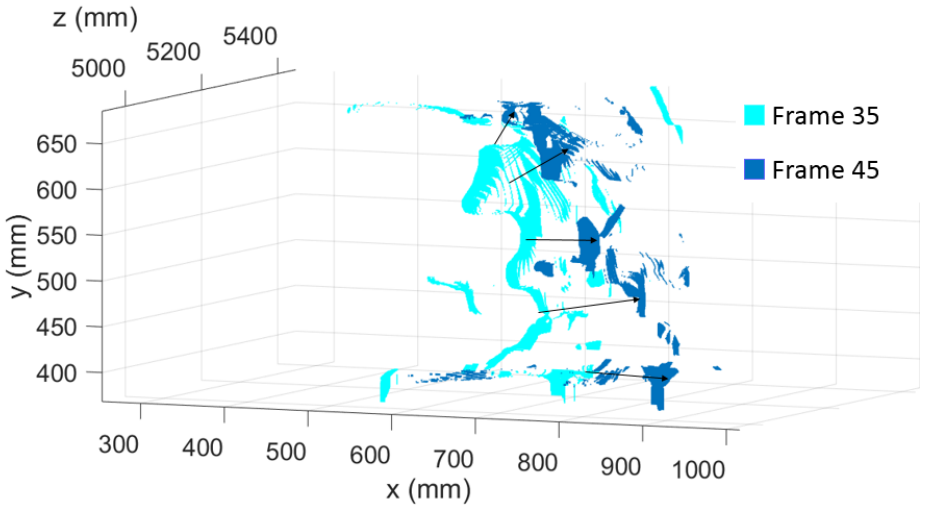

Figure 5.10: The fireball from frames 35 and 45 (0.875 and 1.125 ms after detonation) were isolated and plotted to visualize its propagation.

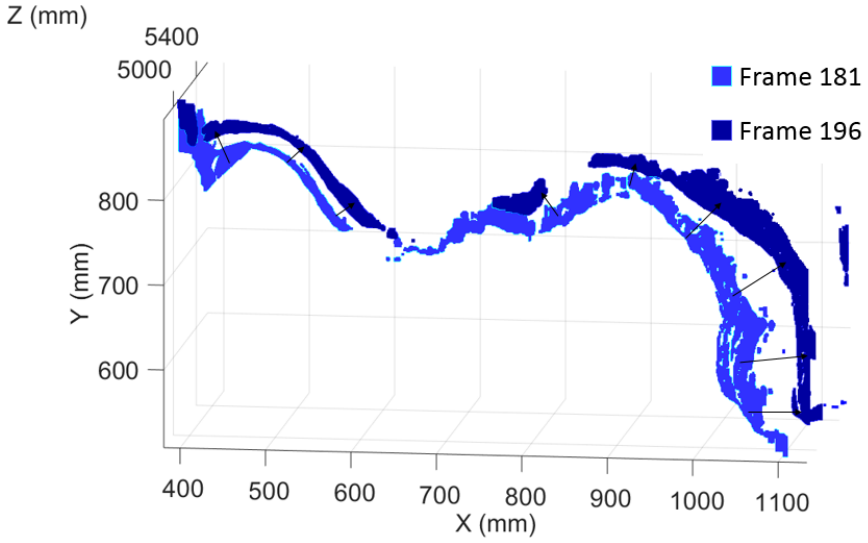

Figure 5.11: The gas cloud from frames 181 and 196 (4.525 and 4.900 ms after detonation) are plotted together to visualize the propagation.

Reprojecting and obtaining velocities for the explosive was performed manually and thus extremely labor-intensive, so only one of the field explosive tests was examined. The work in this chapter shows promise for this technique to be used for tracking shock, fireball and gas cloud propagation, but additional development of image processing routines must be made to allow automation of the process.

CHAPTER 6

CONCLUSIONS AND FUTURE RESEARCH RECOMMENDATIONS

6.1 Conclusions

The work performed here demonstrated the capabilities to reconstruct turbulent gases using stereo schlieren and shadowgraph imaging with post-processing carried out using built-in MATLAB functions. A helium jet was tested as a baseline experiment to understand the capabilities of creating three-dimensional reprojections in stereo schlieren and shadowgraphy. The reprojection algorithm was implemented on explosively-driven tests to identify three-dimensional tracking capabilities in a complex flow field.

The ideal disparity range for the automated reprojection method used is less than 256 pixels. The magnitude of disparities obtained during testing were between 470 and 2300. To identify how this impacted the quality of reconstruction, a simple objected was reprojected with disparity magnitudes of 480, 950, 1510, 2100 and 2700. To assist the matching algorithm, a box of matches was used because it has several unique surface features. The box was reprojected within 10 mm of its true dimensions up to a disparity of 2100. At a disparity of 2700, the box's height, width and depth were 50.2, 67.8 and 31.2 percent larger than the true dimensions, respectively.

A two-dimensional helium jet was analyzed using PIV and SIV to validate the results of the three-dimensional reconstruction analysis. Vertical schlieren cutoff, projective and focused shadowgraphy agreed well with the PIV results after implementing the Abel transform to obtain path averaged PIV data. The circular and horizontal cutoff deviated farther from the other cutoff scenarios. This agrees well with the literature as the accuracy of SIV is heavily dependent on the size of the "particles". The vertical cutoff and both shadowgraph techniques exhibited far more turbulent structures in the desired size range than the circular and horizontal cutoffs, leading to better SIV results.

The stereo schlieren and shadowgraph helium jet tests showed that at small stereo angles similar refractions in each schlieren system could be observed. It was found that there was no depth to the stereo schlieren test images because the disparity range between several common points in the rectified images were the same. Due to this, no additional information was gained by using stereo imaging compared to standard SIV analysis. Depth variation was identified in

the stereo projective shadowgraphy tests, but further investigation is required to perform a quantitative analysis of the fluid motion. The helium jet's surface appeared to be reprojected rather than the internal flow features.

The explosive test using stereo schlieren imaging demonstrated that even with small camera angles, turbulent features in early test frames from the left and right cameras do not appear the same due to variation in refractive index within the flow field and temporal distortions of the flow due to high velocities. However, turbulent structures in later frames are able to be triangulated from the two views.

The field explosive testing using stereo projective shadowgraph imaging was able to successfully reproject and track shock propagation, fireball and gas expansion. The errors produced in these analyses were within the tolerances created by the stereo calibration parameters. There were no reprojections made inside of the fireball and gas cloud due to the opaque gas cloud and large camera angle.

Negative meniscus lenses allow cameras to focus at farther distances in a schlieren system. The increase in focus distance is largely dependent on the focal length of the receiving schlieren lens. As the focal length of the schlieren lens increases, the effect of the negative meniscus lens increases at a non-linear rate. A non-linear trend was also observed when increasing the negative meniscus lens's focal length from -1000 mm to -100 mm. The maximum focus distance obtained in this testing was created using a 900mm schlieren lens and -100 mm negative meniscus lens resulting in a focus distance of 8.5 meters from the camera. This provided an additional 6.5 meters of focus distance when comparing the focus obtained without a negative meniscus lens.

6.2 Future Work Recommendations

Other three-dimensional reconstruction methods should be explored to determine the most appropriate technique to track turbulence. Tomographic reconstruction has previously been used in schlieren imaging to project a three-dimensional volume of the schlieren object and obtain data throughout the volume [7, 13, 26, 46]. It is recommended that tomographic reconstruction is explored here as a better method to reconstruct internal flow features.

Being able to account for different pixel intensities from the left and right camera view would assist in reconstruction. As noted by Lee and Kweon [34], varying exposures in a multi-camera system can lead to complications when creating a three-dimensional reconstruction. A more robust matching algorithm, such as [17], that can account for different light intensities would alleviate the difficulty of perfectly matching the light source's intensity and cutoff percentage in a schlieren system.

The projective shadowgraph reconstructions could be improved if the optical axes of the cameras were parallel. The cameras' optical axes were not parallel

in the field explosive test because only one light source was available. Having a singular light source spread the camera pair 1.5m apart, and in order to maintain the same field of view, the second camera was forced to be rotated. Adding a second light source would allow the cameras to have a similar field of view while maintaining parallel optical axes. The second light source would greatly reduce the disparity of the rectified images, improving the reprojection. Additionally an optically transparent explosive should be used in the projective shadowgraph test as turbulent mixing could potentially be tracked inside the gas cloud.

It was observed that the field of view was reduced when quantifying the effect of negative meniscus lenses in a schlieren system. Additionally stacking negative meniscus lenses further increased the distance the camera could focus. A study characterizing the effect of stacking negative meniscus lenses and its impact on the cameras field of view could contribute to research performed requiring long schlieren systems.

This work could be greatly improved with technological advances of high-speed digital cameras. Current high-speed cameras have very limited resolution compared to standard digital cameras. The development of high-speed cameras with large pixel resolutions would improve tracking and matching methods. Increasing the number of pixels that make up a single turbulent structure would increase its uniqueness, which is a driving factor for tracking and matching algorithms.

REFERENCES

[1] Adhikari, D. and Longmire, E. K. (2012). Visual hull method for tomographic piv measurement of flow around moving objects. *Experiments in Fluids*, 53(4):943–964.

[2] Adrian, R. (1993). *Selected Papers on Laser Doppler Velocimetry*. SPIE Milestone series, vol. MS 78. SPIE Optical Engineering Press.

[3] Anderson, J. S. (2017). Study of turbulent mixing in a post detonation environment using schlieren and imaging spectroscopy. Master's thesis, New Mexico Institute of Mining and Technology, Socorro, New Mexico.

[4] Barre, S., Braud, P., Chambres, O., and Bonnet, J. (1997). Influence of inlet pressure conditions on supersonic turbulent mixing layers. *Experimental Thermal and Fluid Science*, 14(1):68 – 74. Tenth Symposium on Turbulent Shear Flows.

[5] Beauvais, R. (1994). *Laser-Doppler Velocimetry (LDV)*, pages 179–193. Springer Berlin Heidelberg, Berlin, Heidelberg.

[6] Beresh, S., Kearney, S., Wagner, J., Guildenbecher, D., Henfling, J., Spillers, R., Pruett, B., Jiang, N., Slipchenko, M., Mance, J., and Roy, S. (2015). Pulse-burst piv in a high-speed wind tunnel. *Measurement Science and Technology*, 26(9):095305.

[7] Berger, K., Atcheson, B., Ihrke, I., Heidrich, W., and Magnor, M. (2009). Tomographic 4d reconstruction of gas flows in the presence of occluders. In *Proc. Vision, Modeling, and Visualization (VMV'09)*, Braunschweig, Germany.

[8] Bhakta, R. (2018). Development of a low-cost multiple diode continuous laser for piv applications. Master's thesis, New Mexico Institute of Mining and Technology, Socorro, New Mexico.

[9] Biss, M., Settles, G., Hargather, M., Dodson, L., and Miller, J. (2009). High-speed digital shadowgraphy of shock waves from explosions and gunshots. In Hannemann, K. and Seiler, F., editors, *Shock Waves*, pages 91–96, Berlin, Heidelberg. Springer Berlin Heidelberg.

[10] Biswas, S. and Qiao, L. (2017). A comprehensive statistical investigation of schlieren image velocimetry (siv) using high-velocity helium jet. *Experiments in Fluids*, 58(3):18.

[11] Bradski, G. and Kaehler, A. (2008). *Learning OpenCV*. O'Reilly Media, Inc.

[12] Briggs, M., Hill, L., Hull, L., Shinas, M., and Dolan, D. (2010). Applications and principles of photon-doppler velocimetry for explosive testing. pages 414–424.

[13] Décamp, S., Kozack, C., and Sutherland, B. R. (2008). Three-dimensional schlieren measurements using inverse tomography. *Experiments in Fluids*, 44(5):747–758.

[14] Dewey, J. M. (2016). *Measurement of the Physical Properties of Blast Waves*, pages 53–86. Springer International Publishing, Cham.

[15] Discetti, S. and Filippo, C. (2018). Volumetric velocimetry for fluid flows. *Measurement Science and Technology*, 29(4).

[16] Estruch, D., Lawson, N. J., and Garry, K. P. (2009). Application of optical measurement techniques to supersonic and hypersonic aerospace flows. *Journal of Aerospace Engineering*, 22(4):383–395.

[17] Fredriksson, K., Mkinen, V., and Navarro, G. (2007). Rotation and lighting invariant template matching. *Information and Computation*, 205(7):1096 – 1113.

[18] H. Hett, J. (1951). A high-speed stereoscopic schlieren system. *SMPTE Journal*, 56(2):214–218.

[19] Halls, B. R., Gord, J. R., Meyer, T. R., Thul, D. J., Slipchenko, M., and Roy, S. (2017). 20-khz-rate three-dimensional tomographic imaging of the concentration field in a turbulent jet. *Proceedings of the Combustion Institute*, 36(3):4611 – 4618.

[20] Hamzah, R. A., Rahim, R. A., and Noh, Z. M. (2010). Sum of absolute differences algorithm in stereo correspondence problem for stereo matching in computer vision application. In *2010 3rd International Conference on Computer Science and Information Technology*, volume 1, pages 652–657.

[21] Hargather, M., Lawson, M., Settles, G., and Weinstein, L. (2011). Seedless Velocimetry Measurements by Schlieren Image Velocimetry. *AIAA Journal*, 49:611–620.

[22] Hargather, M. J. and Settles, G. S. (2009). Retroreflective shadowgraph technique for large-scale flow visualization. *Appl. Opt.*, 48(22):4449–4457.

[23] Hargather, M. J. and Settles, G. S. (2012). A comparison of three quantitative schlieren techniques. *Optics and Lasers in Engineering*, 50(1):8 – 17. Advances in Flow Visualization.

[24] Heikkila, J. and Silven, O. (1997). A four-step camera calibration procedure with implicit image correction. In *Proceedings of IEEE Computer Society Conference on Computer Vision and Pattern Recognition*, pages 1106–1112.

[25] Hirschmuller, H. (2008). Stereo processing by semiglobal matching and mutual information. *IEEE Transactions on Pattern Analysis and Machine Intelligence*, 30(2):328–341.

[26] Ihrke, I., Berger, K., Atcheson, B., Magnor, M., and Heidrich, W. (2009). Tomographic reconstruction and efficient rendering of refractive gas flows. In Nitsche, W. and Dobriloff, C., editors, *Imaging Measurement Methods for Flow Analysis*, pages 145–154, Berlin, Heidelberg. Springer Berlin Heidelberg.

[27] Jackson, D. A. and Paul, D. M. (1971). Measurement of supersonic velocity and turbulence by laser anemometry. *Journal of Physics E: Scientific Instruments*, 4(3):173.

[28] Jenkins, C., Ripley, R., Wu, C., Horie, Y., Powers, K., and Wilson, W. (2013). Explosively driven particle fields imaged using a high speed framing camera and particle image velocimetry. *International Journal of Multiphase Flow*, 51:73 – 86.

[29] Jonassen, D. R., Settles, G. S., and Tronosky, M. D. (2006). Schlieren piv for turbulent flows. *Optics and Lasers in Engineering*, 44(3):190 – 207. Optical Methods in Heat Transfer and Fluid Flow.

[30] Kalabin, G. V. (1981). Experimental investigation of divergence of confined turbulent jets. *Soviet Mining*, 17(3):271–275.

[31] Kerhervé, F., Jordan, P., Gervais, Y., Valière, J.-C., and Braud, P. (2004). Two-point laser doppler velocimetry measurements in a mach 1.2 cold supersonic jet for statistical aeroacoustic source model. *Experiments in Fluids*, 37(3):419 – 437.

[32] Kolhe, P. S. and Agrawal, A. K. (2009). Abel inversion of deflectometric data: comparison of accuracy and noise propagation of existing techniques. *Appl. Opt.*, 48(20):3894–3902.

[33] Kuznetsov, V. and Bennetts, S. (2013). *Development of Photon Doppler Velocimeter for Explosives Research*. Weapons Systems Division, Edinburgh, South Australia.

[34] Lee, D. and Kweon, I. (2000). A novel stereo camera system by a biprism. *IEEE Transactions on Robotics and Automation*, 16(5):528–541.

[35] MATLAB (2017). *version 9.3.0.713579 (2017b)*. The MathWorks Inc., Natick, Massachusetts.

[36] Merzkirch, W. (1987). *Techniques of Flow Visualization*. AGARD.

[37] Moro, E. A. (2014). New developments in photon doppler velocimetry. *Journal of Physics: Conference Series*, 500(14):142023.

[38] Murphy., M. and Adrian, R. (2010). Piv space-time resolution of flow behind blast waves. *Experiments in Fluids*, 49(1):193–202.

[39] Murphy, M., Adrian, R., Stewart, D., Elliot, G., Thomas, K., and Kennedy, J. (2005). Visualization of blast waves created by exploding bridge wires. *Journal of Visualization*, 8(2):125–135.

[40] Murphy, M., Clarke, S., Munger, A., and Thomas, K. (2009). Application of a schlieren diagnostic to the behavior of exploding bridge wire and laser detonators. In *36th International Pyrotechnics Seminar*.

[41] Murphy, M. J. and Adrian, R. J. (2007). Particle response to shock waves in solids: dynamic witness plate/piv method for detonations. *Experiments in Fluids*, 43(2):163–171.

[42] Pu, Y. and Meng, H. (2005). Four-dimensional dynamic flow measurement by holographic particle image velocimetry. *Appl. Opt.*, 44(36):7697–7708.

[43] Raffel, M., Willert, C., Wereley, S., and J.Kompenhans (2007). *Particle Image Velocimetry: A Practical Guide*. Springer Berlin Heidelberg.

[44] Saxena, A., Chung, S. H., and Ng, A. Y. (2008). 3-d depth reconstruction from a single still image. *International Journal of Computer Vision*, 76(1):53–69.

[45] Scarano, F. (2008). *Overview of PIV in Supersonic Flows*, pages 445–463. Springer Berlin Heidelberg, Berlin, Heidelberg.

[46] Schwarz, A. (1996). Multi-tomographic flame analysis with a schlieren apparatus. *Measurement Science and Technology*, 7(3):406.

[47] Settles, G. (2001). *Schlieren and Shadowgraph Techniques: Visualizing Phenomena in Transparent Media*. Springer Berlin Heidelberg.

[48] Settles, G. (2005). Full-scale high-speed "Edgerton" retroreflective shadowgraphy of gunshots. In *APS Division of Fluid Dynamics Meeting Abstracts*.

[49] Skaggs, M., Hargather, M., and Cooper, M. (2017). Characterizing pyrotechnic igniter output with high-speed schlieren imaging. *Shock Waves*, 27(1):15–25.

[50] Smith, J. L. (2016). Design and construction of a fixture to examine the explosive effects of al/i2o5. Master's thesis, New Mexico Institute of Mining and Technology, Socorro, New Mexico.

[51] Thielicke, W. (2014). *The flapping flight of birds: Analysis and application*. PhD thesis, University of Groningen.

[52] Thielicke, W. and J. Stamhuis, E. (2014). Pivlab towards user-friendly, affordable and accurate digital particle image velocimetry in matlab. 2.

[53] Thielicke, W. and Stamhuis, E. J. (2018). PIVlab - Time-Resolved Digital Particle Image Velocimetry Tool for MATLAB.

[54] Tobin, J. and Hargather, M. (2016). Quantitative schlieren measurement of explosively-driven shock wave density, temperature, and pressure profiles. *Propellants, Explosives, Pyrotechnics*, 41(6):1050–1059.

[55] Tsai, R. (1987). A versatile camera calibration technique for high-accuracy 3d machine vision metrology using off-the-shelf tv cameras and lenses. *IEEE Journal on Robotics and Automation*, 3(4):323–344.

[56] Veret, C. (1952). La strioscopie stereoscopique. *La Recherche Aeronautique*, 29:3–7.

[57] Wagner, J., Beresh, S., DeMauro, E., Pruett, B., and Farias, P. (2017). Towards particle image velocimetry measurements during shock–particle curtain interactions. In Ben-Dor, G., Sadot, O., and Igra, O., editors, *30th International Symposium on Shock Waves 2*, pages 1257–1261, Cham. Springer International Publishing.

[58] Wang, Q. and Zhang, Y. (2011). High speed stereoscopic shadowgraph imaging and its digital 3d reconstruction. *Measurement Science and Technology*, 22.

[59] Y. Cheung, K. and Zhang, Y. (2006). Stereo imaging and analysis of combustion process in a gas turbine combustor. *Measurement Science and Technology*, 17(12):3221.

[60] Yeh, Y. and Z. Cummins, H. (1964). Localized fluid flow measurements with an he-ne laser spectrometer. 4:176 – 178.

[61] Zhang, Z. (2000). A flexible new technique for camera calibration. *IEEE Transactions on Pattern Analysis and Machine Intelligence*, 22(11):1330–1334.

[62] Zollner, H. and Sablatnig, R. (2004). Comparison of methods for geometric camera calibration using planar calibration targets. In *Proceedings of the 28th Workshop of the Austrian Association for Pattern Recognition*, pages 237–244, Hagenberg,Austria.

THREE-DIMENSIONAL RECONSTRUCTION OF TURBULENT GASES USING STEREO SCHLIEREN AND SHADOWGRAPH TECHNIQUES

by

Kyle Jeffrey Benalil